Università degli studi di Catania
in convenzione con
Università degli studi di Palermo

Dottorato di ricerca in

Scienza dei Materiali e Nanotecnologie

Photoactive hybrid graphene-based polymeric materials for water purification

Martina Ussia

Tutor: Prof.ssa Elena Bruno
Dott.ssa Sabrina Carola Carroccio
Dott. Vittorio Privitera
Coordinatore: Prof.ssa Maria Grazia Grimaldi

TESI PER IL CONSEGUIMENTO DEL TITOLO DI DOTTORE DI RICERCA

Cover:
Illustration about the combination of few layers of graphene porphyrin-based polymers, a novel hybrid photoactive material.

Photoactive hybrid graphene-based polymeric materials for water purification.

Martina Ussia

Ph.D. Thesis, University of Catania
Printed in Catania, January 2020

UNIVERSITÀ DEGLI STUDI DI CATANIA

IN CONVENZIONE

UNIVERSITÀ DEGLI STUDI DI PALERMO

DOTTORATO DI RICERCA IN

SCIENZA DEI MATERIALI E NANOTECNOLOGIE - XXXII CICLO

MARTINA USSIA

PHOTOACTIVE HYBRID GRAPHENE-BASED POLYMERIC MATERIALS FOR WATER PURIFICATION

TUTOR: PROF.SSA ELENA BRUNO
DOTT.SSA SABRINA CAROLA CARROCCIO
DOTT. VITTORIO PRIVITERA
COORDINATORE: PROF.SSA M. G. GRIMALDI

TESI PER IL CONSEGUIMENTO DEL TITOLO DI DOTTORE DI RICERCA

FOREWORD

The combined challenges of growing population, climate change and increasing lack of raw materials are leading to paramount innovation in the design of novel devices providing more and more environmentally sustainable solutions. After clay and nanotubes, graphene and its derivatives have become crucial in the preparation of hybrid polymer nanocomposites, being used as an active nanofiller and support of freestanding devices as well. Owing to the possibility of significant improvement as co-catalyst, graphene materials are widely used in combination with polymer-based photocatalysts becoming appealing in water purification applications.

The principal goal of this thesis is to present insights into hybrid graphene preparation and characterization describing also a variety of polymer synthetic strategies for the development of high-potential graphene-based composites.

I dedicate this thesis to my family and Mario for their valuable support, and to my scientific and life mentor Sabrina Carola Carroccio, for her patience and advices during my Ph.D. course.

INTRODUCTION

A great variety of articles, patents and reviews have been devoted to water purification, being considered a very urgent problem for environment, aquatic life and human health. Freshwater scarcity, exacerbated by climate change and growing population requires that pollutants must be definitively eliminated in water and wastewater effluents from both industrial and domestic sources to reuse this primary and vital source.

The water contamination is caused by a number of chemicals that includes conventional and emergent pollutants, harmful heavy metals, toxic dyes, pharmaceuticals, personal care products, microplastics, endocrine disruptor compounds and plasticizers. Therefore, these pollutants can cause bio-accumulative, persistent, carcinogenic, mutagenic, and detrimental effects on the survival of aquatic organisms, flora, fauna, and human health. Hence, providing clean and affordable water by removing contaminants is one of the biggest challenges to be faced by the modern scientific community.

In this context, materials science and nanotechnologies have brought promising alternatives to the conventional water treatment technologies. Through the control of the materials size, morphology and chemical structure, nanotechnology offers novel materials with exceptional adsorptive, catalytic, optical, electrical and/or antimicrobial properties that enhance treatment cost-efficiency. Graphene, since its discovery in 2004 by A.Geim and K. Novoselov, has attracted a lot of attention, thanks to its outstanding mechanical, thermal, optical, and electrical properties. More importantly, graphene with its high theoretical specific surface area of 2600 m^2/g provides a rich platform for surface chemistry. Furthermore, the large surface area combined with its outstanding electron-acceptor properties, make graphene materials ideal candidates for the preparation of composites in water treatment technologies. Indeed, the design of graphene hybrid nanomaterials for both adsorption and photocatalytic applications is one of the most attractive strategies in the field of water remediation.

Figure 1.1 shows the number of publications on graphene-based research by using as keywords the terms “graphene”, “water” and “pollution”. Notably, a significant growth rate from year 2010 with more than 3.000 publications is displayed along with a rapidly increase since 2014, reaching a number of about 29.000 publications in 2019.

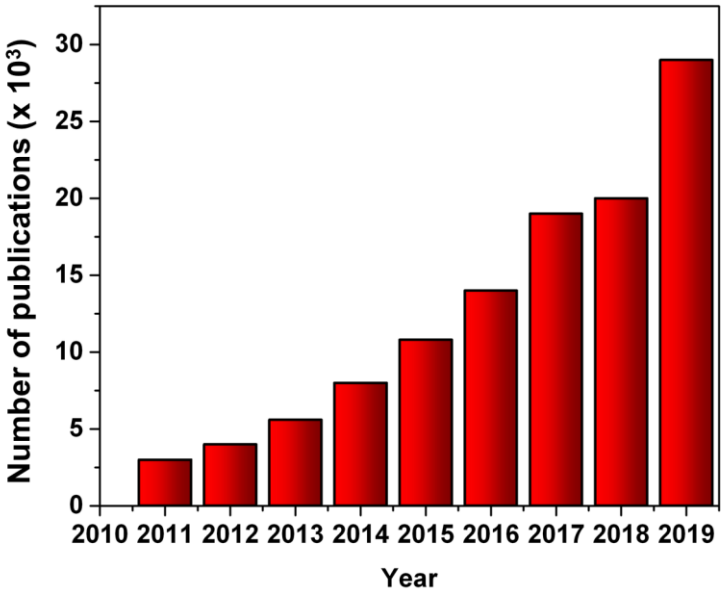

Figure 1.1 Number of papers in the field of the water purification (Scopus research about last 10 years, combining the key words: “graphene” and “water” and “pollution” since 2010).

This thesis contains three chapters that cover the state of the art of relevant topics on preparation, characterization and applications of hybrid polymers graphene-based materials. In particular:

- **Chapter 1** introduces the advantages in the use of heterogeneous photocatalysis for water purification and the role of graphene-based photocatalytic composites to remove conventional and emerging

pollutants. Furthermore, a brief overview on the benefits by combining graphene composites with polymers is also provided;

- **Chapter 2** presents the design and formulation of hybrid graphene-based composites as new photocatalytic systems for degradation of conventional and emerging pollutants in water. In particular, high-quality graphene materials coated by porphyrin-based polymers photocatalysts will be presented; their photocatalytic activity are studied, and eventually a photocatalytic degradation mechanism is proposed. Furthermore, Radical Addiction Fragmentation Transfer polymerization technique for the synthesis of novel porphyrin-based polymers will be described.
- **Chapter 3** is focused on the preparation of innovative nanocomposites based on a polymeric cryogels containing graphene oxide and ZnO nanostructures. Particularly, sponges enriched with ZnO by ALD acquire photocatalytic properties, allowing recyclability after their irradiation by UV light. In particular, will be demonstrated how cryopolymerization allowed by combining tailored individual components afford special features to the final sponges, making them an effective strategy for improving the removal and the degradation of contaminants in water.

CHAPTER 1

RESEARCH AND BACKGROUND

1.1 Water pollution

"*Thousands have lived without love,*
not one without water"
W. H. Auden

Even if all of us know that water is crucial for life, we waste it anyway. From macropolluttants to invisible chemicals, a great variety of contaminants end up in our world's water sources such as lakes, rivers, streams, groundwater and eventually the oceans. Water contamination has drastically contributed to a freshwater crisis, threatening the sources of water supply. The global water demand has critically increased in the last 100 years estimating also that it will continue to grow with a rate of about 1% per year as a function of the growing population, climate change, economic development and many other factors [1]. Therefore, to better address this aspect, it is necessary to in deep understand what is meant for water pollution. The pollution term come from the Latin word "*polluts*", which means contaminated. It can be further defined as the introduction of hazardous substances into the environment, harmful for any living organism, resources, structures, amenity and ecological systems. Given that, water pollution can be considered as the contamination of the water bodies (lakes, rivers, oceans, and groundwater) and it can be categorized into two groups: point sources and non-point sources.
The pollution point sources are those that come from a single location and can be directly checked, monitored and regulated. This class includes discharge pipe attached to a factory, oil spill from a tanker, both municipal and industrial wastewater effluent.
The non-point source contamination is referred to pollutants derived from diffuse sources, difficult to identify and regulate. These may comprise for example agricultural and rainwater runoff or waste blown into waterways from land.
In **Figure 1.2,** different types of the most relevant water pollutants are showed, including emerging inorganic and organic compounds, dyes, heavy metals, pesticides, biocides and pharmaceuticals.

Figure 1.2. Main water contaminants [Adapted from Ref. [2] with kind permission of Elsevier].

Most of these undesirable chemicals, biological contaminants, suspended solids and gases, cannot be eliminated naturally from water, and depending on the intended use of water, it is necessary remove them by using physical, biological or chemical processes, avoiding at the same time secondary contamination for the environment caused by the treatment itself.

1.2 Purification methodologies

During the beginning of the twentieth, a multitude of techniques currently used were developed and optimized to remove contaminants from water. These processes, classified as conventional methods, include adsorption, coagulation, flocculation, sedimentation and filtration, followed by disinfection [3]. However, such techniques suffer of several limitations. Adsorption or coagulation only concentrate the contaminants by transferring them from one phase to another one, without a complete elimination. Other conventional methods such as sedimentation, flocculation, filtration, involve high operating costs, releasing also more toxic by-products into the environment. In addition, chlorination methods, the most commonly and widely used disinfection processes, cause the generation of secondary pollutants that are

mutagenic and carcinogenic to human health [4,5]. In light of this, scientific community concentrates its attention to find alternative, environmental-friendly and cheapest solutions. Thus, advanced technologies were established over this time to satisfy more complex final user goals, such as the removal of carcinogenic and endocrine disrupting chemicals, toxic volatile organic compounds (VOCs), personal care products (PCPs), pesticides and cyanotoxins. They may include membrane filtration, adsorption onto non-conventional solids, advanced oxidation processes (AOPs) or electrochemical oxidation. The **Figure 1.3** summarize the available conventional and advanced water purification methodologies.

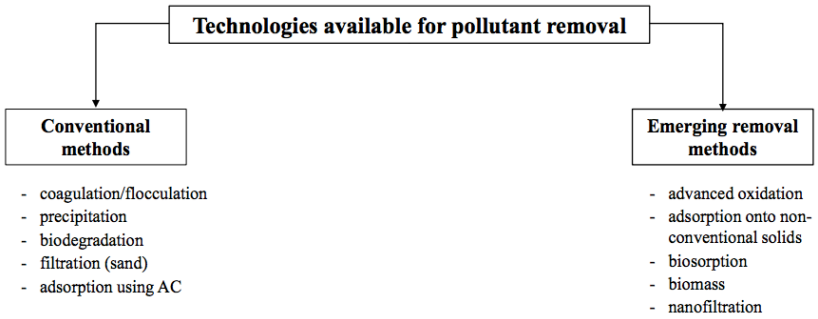

Figure 1.3. Available technologies for contaminants removal from water [Reproduced from Ref. [6] with kind permission of Springer].

Furthermore, during the twenty-first century new exciting opportunities to the water treatment systems come from with the use of the nanotechnologies. Nanomaterials have structural features significantly different from corresponding bulk materials possessing enhanced performances when used in similar applications. This is mainly due to the large surface area to volume ratio of nanomaterials that leads, in comparison with conventional materials, to higher ratio between atoms on the surface and those within. As a consequence, lower molar concentrations of nanomaterial, compared with the corresponding bulk materials, are required with obvious advantages in reduction of costs, fast dissolution and strong sorption. Furthermore, nanomaterials possess enhanced reactivity, sub-surface transport, and/or sequestration characteristics. Hence, by controlling material size,

morphology and chemical structure, nanotechnologies represent a key role in the development of novel materials with exceptional catalytic, adsorptive, optical, quantum, electrical and/or antimicrobial properties, able to boost both basic and advanced water treatment processes.

1.3 Advanced oxidation processes

Advanced oxidation processes (AOPs) are described for the first time by Glaze et al. in 1987 as water treatment methods which involve the production of highly reactive molecules, such as hydroxyl radicals, in "*sufficient quantity to effect water purification*" [7]. If compared to conventional separation methodologies, which only transfer the pollutants from one phase to another without destroying them, AOPs offer the advantage to remove contaminants definitively with high reaction rates, preventing at the same time the generation and disposal of secondary waste materials. Additionally, the non-selectivety offers the opportunity to use AOPs for a wide range of contaminants.
For these reason, AOPs can be considered superior processes that are very effective in the treatment of conventional and emerging organic toxic compounds without high energy consumption (see **Figure 1.4**).

Figure 1.4. Application fields of AOPs [Reproduced from Ref. [8] with kind permission of Elsevier]. [8]

The fundamentals steps involved in AOPs can be summarized as follows:
1. The production of strong oxidants like $OH^{\bullet}$, $HO_2^{\bullet}$, $O_2^{\bullet 2}$, $^1O_2$ etc. also called reactive oxygen species (ROS);

2. The produced ROS react with organic contaminants present in the water converting them into biodegradable compounds;

3. The oxidation and mineralization of the biodegradable intermediates in water, carbon dioxide, and inorganic salts.

Until now, several AOPs have been efficiently proposed for the degradation of contaminants. They can be distinguished into two main groups: photochemical and non-photochemical AOPs [8]. Some common photochemical and non- photochemical AOPs are reported in **Table 1.1**

Photochemical AOPs	**Non-photochemical AOPs**
Photolysis (UV + H_2O_2)	Ozone (O_3)
Photocatalysis (Light + Catalyst)	Fenton (Fe^{2+} + H_2O_2)
Photo-Fenton (Light + Fenton)	Electrolysis (Electrodes + Current)
	Sonolysis (Ultrasound)
	Microwaves + H_2O_2

Table 1.1 AOPs: photochemical and non-photochemical processes

Non-photochemical AOPs usually involve the use of strong oxidizing agents like hydrogen peroxide (H_2O_2), ozone (O_3) or catalysts such as iron ions, electrodes and metal oxides. Differently, the photochemical AOPs use irradiation (UV light, solar light, ultrasounds) to activate the catalyst. The latter are considered the most attractive methods being simple, clean, relatively inexpensive, and more efficient than chemical AOPs. Photochemical AOPs, such as photolysis (H_2O_2/UV), photo-Fenton process (H_2O_2/Fe^{2+}/UV), and heterogeneous photocatalysis (catalyst/hv) have been widely used to degrade or mineralize organic pollutants in water. In particular, the photo-Fenton process, compared to photolysis, is considered the best method to rapidly decompose a great variety of conventional and emerging pollutants with low energy consumption. However, the main limitation in the use of photo-Fenton

method is the production of a large quantity of ferric-hydroxide molecules at pH values higher than 4.0 [9,10]. Additionally, post-recovery of the catalyst is difficult, being also misplaced in the sludge. These drawbacks can be overcome by considering heterogeneous photocatalysis. The latter, uses a photocatalyst having the possibility to be removed after the purification process, allowing also the decontamination of water in a wide range of experimental conditions without high energy and cost consumptions.

1.4 Heterogeneous photocatalysis

Heterogeneous photocatalysis represents one of the most promising AOPs, as a cheapest and eco-friendly method to mineralize completely organic pollutants as well as metal ions [11]. Photocatalysis was introduced for the first time at the Institut de Catalyse and at the Université Claude Bernard in Lyon (France) in 1970, and from this date, it demonstrated potential uses not only in environmental field, but also for medical and structural applications (see **Figure 1.5**). [11,12]. Photocatalysis uses photon energy converting it into chemical energy, necessary to induce several reactions at the photocatalyst surface.

Figure 1.5. Potential applications of heterogeneous photocatalysis [Reproduced from Ref. [11] with kind permission of IOP Publishing]. [11].

Photocatalysis research area is devoted to explore new molecules and their potential in different field of applications. In the case of water purification field, the generated energy is converted to produce Reactive Oxygen Species (ROS) able to degrade the contaminants. The overall steps involved during the photocatalytic degradation of pollutants in water can be summarized into the follows [12]:

1. Migration of the pollutants from the liquid phase to the photocatalyst surface.
2. Adsorption of the pollutant onto the photocatalyst surface.
3. The generation of reactive oxygen species followed by the chemical degradation of the pollutants.
4. Desorption of the intermediate or final products from the photocatalyst surface and migration into the liquid media.

Many organic and inorganic photocatalysts have been extensively used in water purification and disinfection. Organic dyes like porphyrins or phthalocyanines are used as photosensitizers, while the most common used inorganic photocatalysts are TiO_2, ZnO, ZnS, CdS, Fe_2O_3, and WO_3 [13]. The main difference in the use of inorganic or organic photocatalysts principally depends on the light energy required to activate their photochemical process. Specifically, semiconductors require the UV-A range (λ<400 nm), whereas the photosensitizers need the visible-light range (400-800 nm).
In the next paragraphs the photosensitization processes of these two classes of photocatalysts will be in deep described.

1.4.1 The visible-light photocatalysis

The photosensitization process in water principally involves three components: photocatalyst, light, and oxygen. By irradiation at appropriate wavelengths, production of ROS occurred. As reported in the previous paragraphs, ROS are capable to oxidize organic pollutants into CO_2 and water and are naturally cytotoxic destroying unwanted microorganisms, acting also a disinfection process (see **Figure 1.6**).

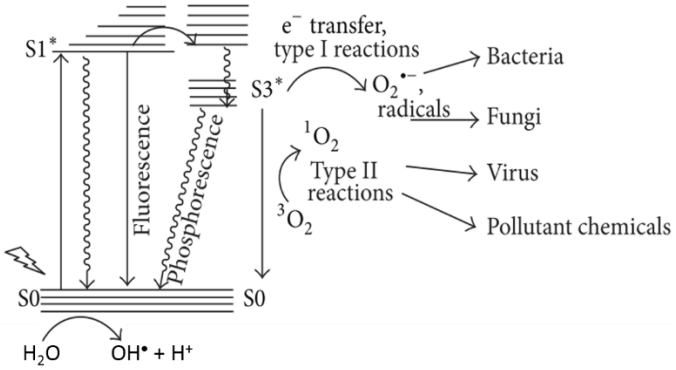

Figure 1.6. The Jablonski diagram [Adapted from Ref. [13] with kind permission of Hindawi]

Depending on the nature of the photocatalyst, the photodynamic action proceeds through type I or type II mechanism (schematized in **Figure 1.6**) or both. Type I mechanism involves electron transfer from excited sensitizer to substrate molecule or oxygen yielding free radicals and superoxide ion, whereas in type II mechanism energy transfer between photosensitizer and oxygen produces singlet oxygen. [13] Organic photocatalysts (photosensitizers) commonly used in the photodegradation of contaminants are summarized in **Figure 1.7** [14]. They possess evident chemical diversity, ranging from aromatic to heteroaromatic rings, porphyrins and phatocyanines. However, all of these classes of molecules absorb light in the visible range (400-800 nm) and **Figure 1.8** represents their most significant absorption bands.

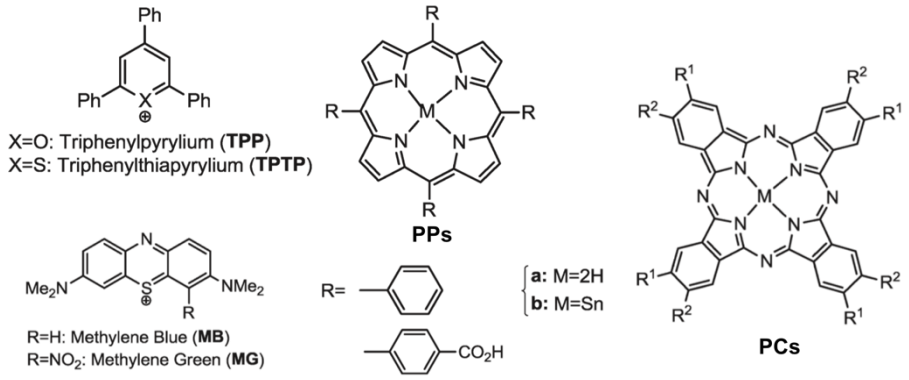

Figure 1.7. Structures of the most common organic semiconductors [Adapted from Ref. [14] with kind permission of the ACS].

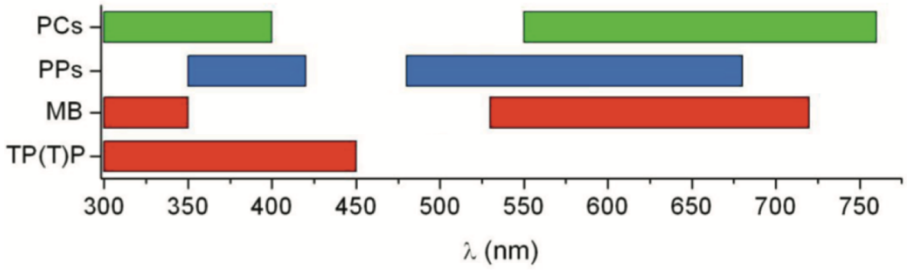

Figure 1.8. Absorption in the UV-Visible range of the organic photocatalysts [Adapted from Ref. [14] with kind permission of the ACS]. [14].

For such kind of molecules, the excitation process is achieved by the electron transfer from their ground state (S0) to the singlet excited state (S1∗).

$$S0 + h\nu \rightarrow S1^{*} \quad \textbf{(1)}$$

Thus, different pathways can occur:

($S1^{*}$) can undergo intersystem crossing (ISC) to give the triplet excited state ($S3^{*}$); then ($S1^{*}$) and ($S3^{*}$) can relax to the ground state resulting in fluorescence and phosphorescence processes, respectively [15,16]

$$\text{Intersystem crossing (ISC) } S1^{*} \rightarrow S3^{*} \quad \textbf{(2)}$$

$$\text{Relaxation } S1^{*} \rightarrow S0 + h\boldsymbol{\nu} \text{ (fluorescence)} \quad \textbf{(3)}$$

$$\text{Relaxation } S3^{*} \rightarrow S0 + h\boldsymbol{\nu} \text{ (Phosphorescence)} \quad \textbf{(4)}$$

Otherwise, since ($S3^{*}$) possesses a longer lifetime than ($S1^{*}$), it can be subject to electron transfer (type I mechanism) or energy transfer (type II mechanism) to another molecule [16]. As it can be possible to see from equations (5) and (6), in presence of oxygen, the photosensitizer can transfer its energy to the oxygen triplet ground state ($^{3}O_{2}$) giving singlet oxygen, which is considered the most reactive ROS (equation 5). Alternatively, by the type I mechanism, in presence of oxygen, superoxide radicals can be produced (equation 6).

Electron transfer (type I) $S3^{*} + O_2 \rightarrow S^{\cdot +} + O_2^{\cdot -}$ (5)

Energy transfer (type II) $S3^{*} + {}^3O_2 \rightarrow S0 + {}^1O_2$ (6)

Beyond the opportunity to use photosensitizers under visible-light irradiation, taking advantage in the use of the sun as the most available and environmentally-friendly energy source, they are able to produce singlet oxygen, which is considered the most cytotoxic ROS. However, many improvements in the visible-light photocatalysis have to be carried out to overcome some drawbacks. For instance, some visible-light molecules require to be synthesized, hence increasing their production cost. More importantly such kind of molecules are susceptible to photobleaching reducing drastically their stability during the photocatalytic degradation process.

1.4.2 Uv-based photocatalysis

Semiconductors such as TiO_2, Fe_2O_3, WO_3, ZnO, and CdSe are widely used for photocatalytic applications. If compared to the photosensitizers, also in the case of inorganic semiconductors the photoprocess is driven by the promotion of electrons from their fundamental (VB) to the excited state (CB) triggered by light absorption. In particular, the band gap (Eg) value provides to the portion of the solar spectrum that can be used to activate the photocatalyst, while the CB and VB potential positions specify the reductive and oxidative powers of the photogenerated electrons and holes of the semiconductor [16_tan]. **Figure 1.9** shows the Eg value as well as the CB and VB potentials of the most commonly used semiconductors.

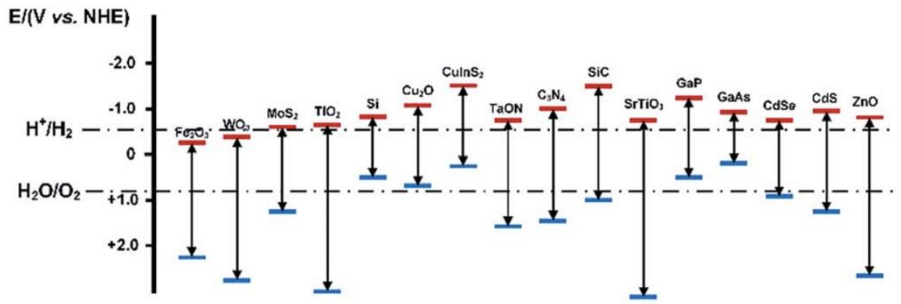

Figure 1.9. Band gap of the most used inorganic semiconductors [Reproduced from Ref. [18] with kind permission of the RSC].

Being such king of metal oxide and sulfide wide band gap semiconductors, they require the UV-A range (<400 nm) to activate the photochemical processes, which represents only 5% of the solar spectrum. However, most of the semiconductors are easily available, require low preparation cost and possess long-term stability. In light of this, several strategies to extend light absorption range are under investigation. The photocatalytic mechanism of ROS production is quite similar to those of the photosensitizers with the exception that inorganic semiconductors are not able to produce the singlet oxygen. Thus, when a semiconductor is irradiated with light of wavelength equal or greater than its band gap, energy is absorbed, resulting in the promotion of electrons from the VB to the CB, and the formation of electron-hole pairs. These charge carriers may recombine, with the energy being reemitted as light or heat, or they may migrate to the catalyst surface where they can take part in redox reactions in the particle-solution interface (see **Figure 1.10**).

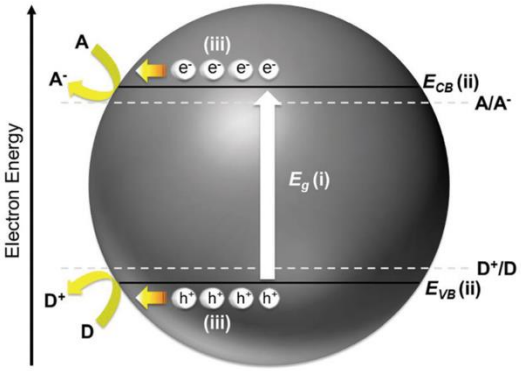

Figure 1.10. [17] Semiconductor fundamental features to allow the photochemical processes [Reproduced from Ref. [17] with kind permission of the RSC].

Following the abovementioned type I mechanism, $HO^{\cdot}$, $O_2^{\cdot-}$ and $HOO\cdot$ radicals are produced (7-10). The as produced oxidizing agents can undergo other reactions to form hydroperoxyl radical and subsequently H_2O_2 as well as oxidize pollutants into CO_2 and H_2O (11–14).

$$\text{Semiconductor} + h\nu \rightarrow h_{VB}^{+} + e_{CB}^{-} \quad (7)$$

$$h_{VB}^{+} + H_2O \rightarrow HO^{\cdot} + H^{+} \quad (8)$$

$$e_{CB}^{-} + O_2 \rightarrow O_2^{\cdot-} \quad (9)$$

$$O_2^{\cdot-} + H^{+} \rightarrow HOO^{\cdot} \quad (10)$$

$$HOO^{\cdot} + HOO^{\cdot} \rightarrow H_2O_2 + O_2 \quad (11)$$

$$HO^{\cdot} + \text{pollutant} \rightarrow CO_2 + H_2O \quad (12)$$

$$O_2^{\cdot-} + \text{pollutant} \rightarrow CO_2 + H_2O \quad (13)$$

$$HOO^{\cdot} + \text{pollutant} \rightarrow CO_2 + H_2O \quad (14)$$

1.4.3 Influencing factors of photodegradation of pollutants

Some basic features could critically influence each step of photocatalysis. The nature and structure of the photocatalyst as well as its surface area, determine the overall performances of the photocatalytic process. Furthermore, the oxidation of contaminants in water is highly dependent on a variety of operational parameters, such as the concentration of the substrate, photocatalyst content, pH and temperature of the solution, time and intensity of light irradiation and dissolved oxygen. The heterogeneous photocatalysis consists in a multistep process including seven key stages depicted in **Figure 1.11**: (1) light harvesting; (2) charge excitation; (3) charge separation and transfer; (4) surface reduction reactions; (5) surface oxidation reactions; (6) bulk charge recombination; and (7) surface charge recombination. Being the loss of efficiency for each step crucial in determining the final performance of photocatalysis, a variety of engineering modification of semiconductor surfaces and interfaces have been proposed and they are still under investigation [19].

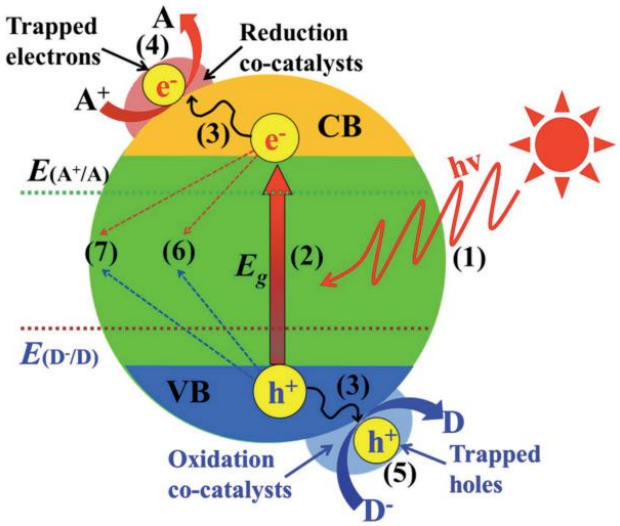

Figure 1.11. The typical stages of heterogeneous photocatalysis [Reproduced from Ref. [19] with kind permission of the RSC].

For instance, preparation of photocatalysts with macro/mesoporous or peculiar inner structures allows enhanced scattering of light inside the as generated pore channels or cavities due to multiple reflections. This results in improved captured of light along with more photogenerated electron-hole pairs [20-22]. Beside light-harvesting, also charge separation/transport kinetics represents a key role to improve the photocatalysis quantum efficiency, reducing at the same time recombination of photo-generated electron/hole pairs. Indeed, CB electrons can recombine with VB holes very quickly releasing energy in the form of unproductive heat or photons. In this context, the fabrication of various kinds of heterojunctions, such as the Schottky junction, Type II heterojunctions, and all solid-state Z-scheme junctions, pore texture tailoring, quantum-size effects, and co-catalysts loading are considered the most effective and promising strategies to gain better charge separation/transport kinetics [19,23]. These methods not only are able to enhance light harvesting and molecular diffusion/transport processes, but also increase the specific surface area of the photocatalyst by accelerating the surface reaction kinetics. In particular, the use of a co-catalyst able to trap the photogenerated electrons, can allow the suppression of recombination phenomena promoting charge carrier and migration to the catalyst surface where redox reactions can occur. Depending on the nature of semiconductor (inorganic or organic), different types of co-catalysts have been extensively studied, including noble metals (Pt, Au, Ag), [24-28] graphene-based materials, [23, 29-31], transition metals and their composites. Among these graphene-based materials have attracted much attention for both organic and inorganic semiconductors due to their unique features in terms of charge transfer and separation capability [32,33].

1.5 Graphene-based photocatalysis

Since its discovery in 2004 by A.K. Geim and K.S. Novoselov, graphene, a single layer of carbon atoms tightly packed into a two-dimensional (2D) honeycomb lattice, attracted notable interest among scientific and technological communities [32]. Thanks to its superior electrical conductivity and mobility, theoretically high specific surface area, excellent optical transmittance (see **Figure 1.12**), the graphene-

driven “gold rush” has become widespread in various areas. In light of this, it is not surprising to find graphene applied also in the field of photocatalysis [29-31].

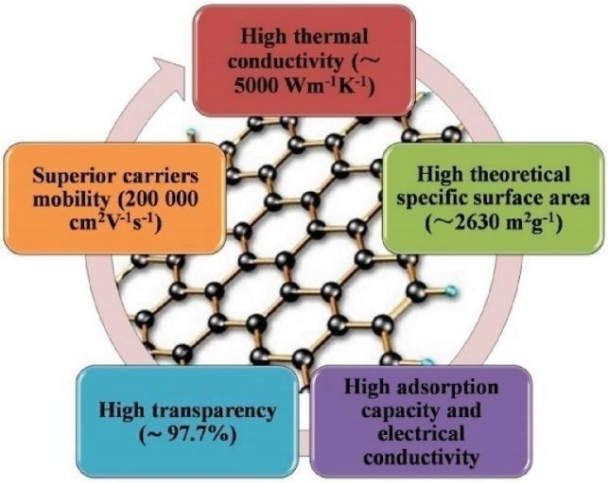

Figure 1.12. Fundamental features of graphene [Reproduced from Ref. [23] with kind permission of the RSC].

Figure 1.13 reports the number of publications by inserting the terms “photocatal” and “graphene” separately as keywords, observing a significant growth rate from year 2000 maintaining a marvelous rate. On the other hand, by combining these two areas (see the inset of **Figure 1.13**), an exponential growth of publications since 2009 is observed [33], suggesting the great attraction in the application of graphene in photocatalytic systems.

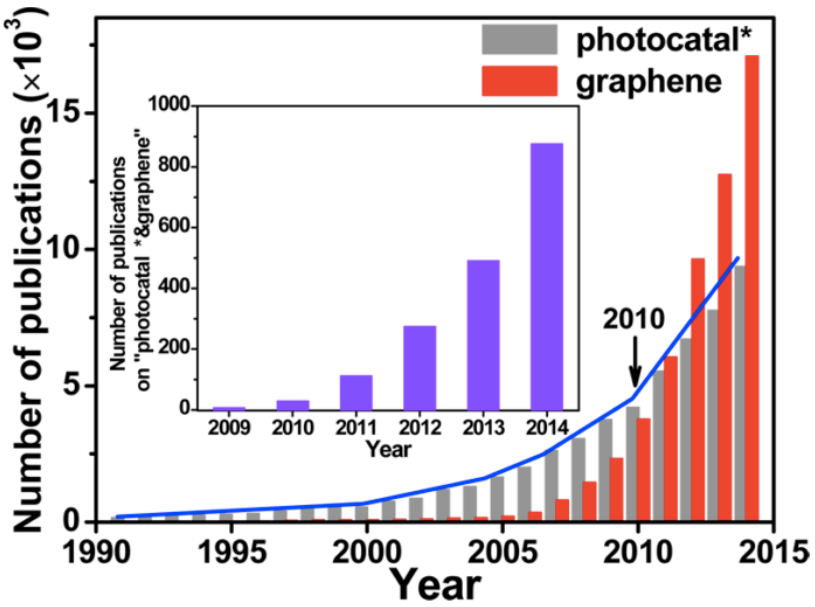

Figure 1.13. Number of papers in the field of graphene-based photocatalysis [Scopus research by using as key words “photocatal” and “graphene” separately and combined as well (see the inset)]. Reproduced from Ref. [33] with kind permission of the ACS.

Indeed, graphene-based materials aimed to improve the photocatalytic performances of organic and inorganic semiconductors, mainly due to a decrease in the band-gap of the composite, an enhancement of the adsorptive features, and most importantly an improvement in the charge separation and transport phenomena [34].

1.6 Concept and properties of graphene materials.

An overview of the structure and main properties of graphene-based materials are reported in **Figure 1.14**. Pristine or “high-quality” graphene is composed of a single layer of carbon atoms arranged in a sp^2-bonded aromatic assembly and it can be distinguished from graphene oxide (GO) and reduced-graphene oxide (RGO).

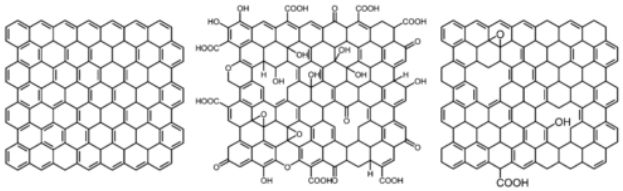

Properties	Graphene	Graphene Oxide	Reduced Graphene Oxide
Synthesis	-Chemical vapor deposition -Thermal decomposition of SiC -Graphite exfoliation	-Oxidation and exfoliation of graphite	-Reduction of graphene oxide
C:O ratio	No oxygen	2-4	8-246
Young's modulus (TPa)	1	0.2	0.25
Electron mobility ($cm^2 V^{-1} s^{-1}$)	10 000–50 000	insulator	0.05–200
Production cost	High	Low	Low

Figure 1.14. The main properties of graphene-based materials [Reproduced from Ref. [35] with kind permission of the RSC].

Pristine graphene can be naturally found as the building block of graphite, where graphene sheets are stacked by π-π interactions with an interlayer distance of 3.34 Å. The preparation of high-quality graphene was firstly demonstrated by Geim and Novoselov using the micromechanical exfoliation method, leading to the Nobel Prize in Physics in 2010. However, this technique is considered labor-intensive and not easily scalable. Thus, different approaches were developed such as ultrasonication of graphite in organic solvents, thermal decomposition of SiC or epitaxial growth of graphene on transition metals (Ni, Pd, Ru, Ir, Cu) via chemical vapor deposition (CVD) of hydrocarbons or alcohols. Among these, CVD has been pointed out as the most inexpensive, and scalable strategy to produce high quality graphene [35-37]. Application of graphene in photocatalysis is mainly due to its excellent electronic properties derived from the high-quality 2D crystal lattice. Specifically, the valence orbitals of a single carbon atom sp^2 hybridized, are composed of three planar δ orbitals (120° with each other) and one remaining 2p orbital ($2p_z$) oriented along the perpendicular axis to the graphene plane [19]. Thus, single unit cell in

composed by two equal carbon sublattices A and B [**Figure 1.15 (a)**]. The so-unique band structure obtained was demonstrated for the first time by the density functional theory (DFT) calculation by Walace in 1947 [**Figure 1.15 (b)**] [37].

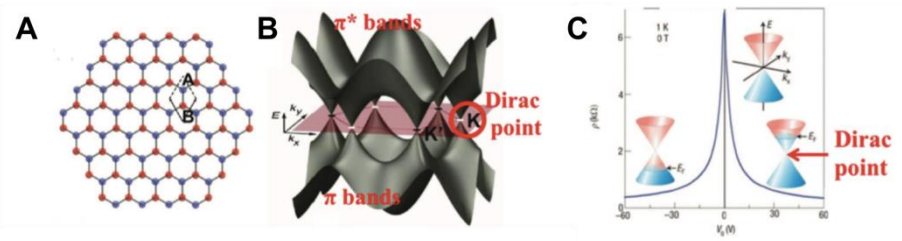

Figure 1.15. a) The hexagonal honeycomb lattice of graphene with two atoms A and B per unit cell; b) The tridimensional band structure of graphene; c) The conduction and valence bands in single-layer graphene with a representation of the Dirac point [Adapted from Ref. [19] with kind permission of the Wiley-VCH]

The π electrons among two carbons belonging to the respective $2p_z$ orbitals are related to delocalized π (bonding) and π* (anti-bonding) bands, forming an highest occupied valence band (VB) and a lowest unoccupied conduction band (CB) [**Figure 1.15 (b)**] [37]. In particular, the VB and CB converge at six points (Dirac or neutrality points). From the electronic point of view, the contact of two bands at Dirac points indicates that graphene monolayer is a semi-metal or zero-gap semiconductor [**Figure 1.15 (c)**] [37] with a work function ≈4.42 eV [19]. GO is an oxidized form of graphene, composed of a high density of oxygen functional groups (carboxyl, hydroxyl, carbonyl, and epoxy) in the carbon lattice. The cost of monolayer graphene still remains high for practical application in water remediation as well as electronic, optical, and biological uses. To obtain cheapest graphene, sacrificing some peculiar features of monolayer (see **table 1.2**), graphene derivatives materials are developed and widely used in several fields including water remediation. GO production was proposed for the first time by Hummers and Offeman in 1958 by using $KMnO_4$ as oxidizing

agent in concentrated sulfuric acid [38]. Then, different modified Hummer methods was proposed to improve the reaction yields and, at the same time, more environmental-friendly solutions. However, $KMnO_4$-based reaction remains the most used method for GO production. The introduction of oxygen in the graphene critically affect its physicochemical properties reducing its electronic and mechanical properties [39,40]. Instead, the high density of oxygen functional groups makes GO more hydrophilic, and this feature, along with the high surface area, allows GO available for a wide range of chemical functionalization. Therefore, GO in considered an important building block for the development of novel graphene-based composites. The reduction of GO, by using chemical reducing agents, thermal annealing, photoreduction, or microwave-assisted reduction [41,42], is used to produce RGO. More importantly, RGO possess an altered chemical structure if compared to graphene and GO, having carbon vacancies, residual oxygen, and clustered pentagons and heptagons carbon structure [43,44], allowing also a partial restoration of mechanical and electronic properties (see **Figure 1.14**).

1.7 The role of graphene materials in photocatalysis

The main role of graphene derivatives in photocatalytic composites involves their use as acceptor and shuttle of the photogenerated electrons [45-47]. Clearly, high-quality graphene explicates superior capability as acceptor and stabilizer of charge carriers if compared to GO and RGO. On the other hand, these low cost materials further result to be peculiar in adding adsorption properties to the final devices for the removal of contaminants in water. Besides these properties, graphene materials are also able to tune the light absorption range and intensity. In the following sub-sections, a summary of these roles in graphene-based composite photocatalysts will be reported.

1.7.1 Graphene as photoelectron shuttle and acceptor

Graphene as unique 2D electron conductive platform is able to work as co-catalyst in photo-induced electron transfer processes (see **Figure 1.16**) [32]. In particular, after photoexcitation of a semiconductor (organic or inorganic), the photogenerated electrons in their excited state are injected to the graphene surface boosting separation and transfer of charge carriers, reducing the electron-hole recombination rate and participating in photo-redox processes.

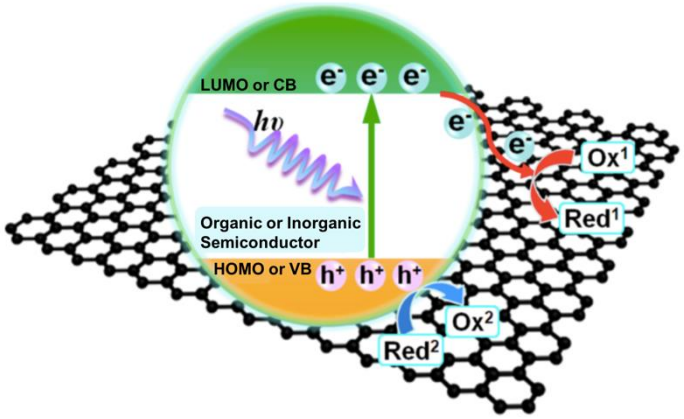

Figure 1.16. Chart of the charge carrier transfer for semiconductor photocatalysts to graphene [Reproduced from Ref. [33] with kind permission of the ACS].

In light of this, in recent years many graphene-based materials and semiconductors composites has been developed, exploiting also the photoinduced electron transfer mechanism through UV-Vis spectroscopy [48], as well as steady state and time resolved fluorescence [49,50]. For example, Zhang et al. reported a tetrasulfonated zinc phtalocyanin bounded to graphene sheets by non-covalent interactions, demonstrating the ability of graphene to accept and transport electrons [46]. Recently, Lightcap et al. described the ability of RGO to store and shuttle electrons. In particular, photogenerated electrons by irradiation of TiO_2 can be transported

through RGO to reduce silver ions (Ag^+) into Ag nanoparticles and selectively anchoring semiconductor TiO_2 and Ag nanoparticles at separate sites of RGO support [48].

1.7.2 Adsorption ability of graphene materials.

Thanks to its peculiar 2D structure and high theoretical surface area, graphene and its derivatives, in addition to their use as photoelectron media, are able to enhance the adsorption capacity versus several target reactants (e.g. dyes, emerging pollutants, heavy metals) [33]. As reported in **Figure 1.17** the enhancement of adsorption ability of graphene-based composites can be attributed to different types of interactions such as physical adsorption, electrostatic attraction, or chemical interaction (surface complexation) [51]. The introduction of oxygen or nitrogen functional groups on the graphene surface contributes to increase the interaction of the composites with a wide variety of molecules and metal ions allowing an improvement in the photoredox activity [33].

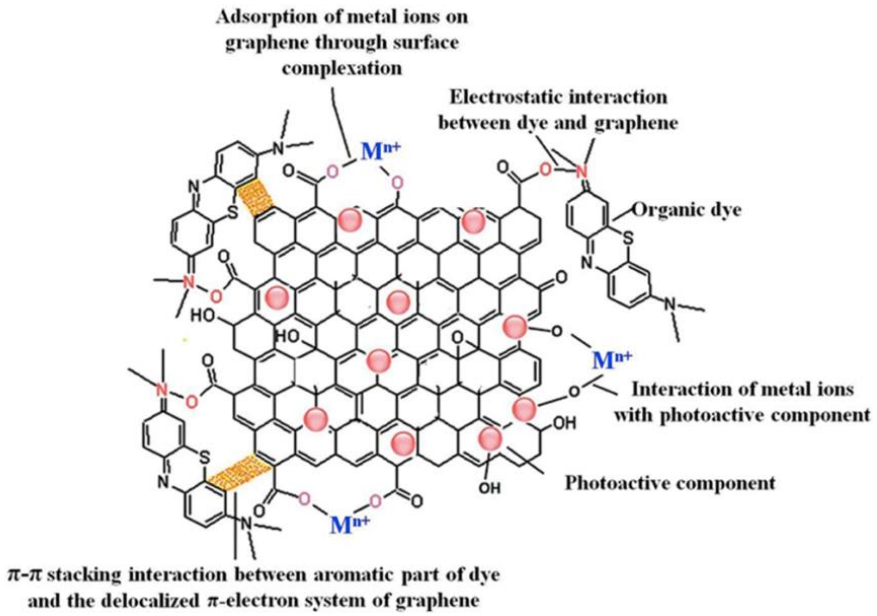

Figure 1.17. Representation of different types of interactions involved during the pollutants adsorption on graphene-based photocatalysts [Reproduced from Ref. [33] with kind permission of the ACS].

As an example, the mechanism by which graphene–based composites can enhance the photocatalytic performance in the degradation of organic dyes can be described by three sequential steps (see **Figure 1.18**). The first step involves the adsorption of the dye molecules on the graphene surface by π-π stacking interactions between the graphene and dye sp_2 domains. Upon interaction with graphene sheets, the oxidative species surrounding the catalyst can readily access the adsorbed dye, making the photodegradation process more effective. The strong contact facilitates the reactions after the photocatalyst irradiation, allowing a more effective photodegradation process. The second step is the generation of electron-hole pairs after the photocatalyst irradiation with appropriate wavelength. At the end, the third step concerns the charge carrier separation and transport [33]. As well stated from the aforementioned section, the excited electrons are transferred from the photocatalyst to the sp_2-hybridized graphene

platform. The photogenerated holes and excited electrons are subjected to further reactions in the aqueous media forming ROS, able to degrade contaminants in water providing eventually to their mineralization in CO_2 and H_2O.

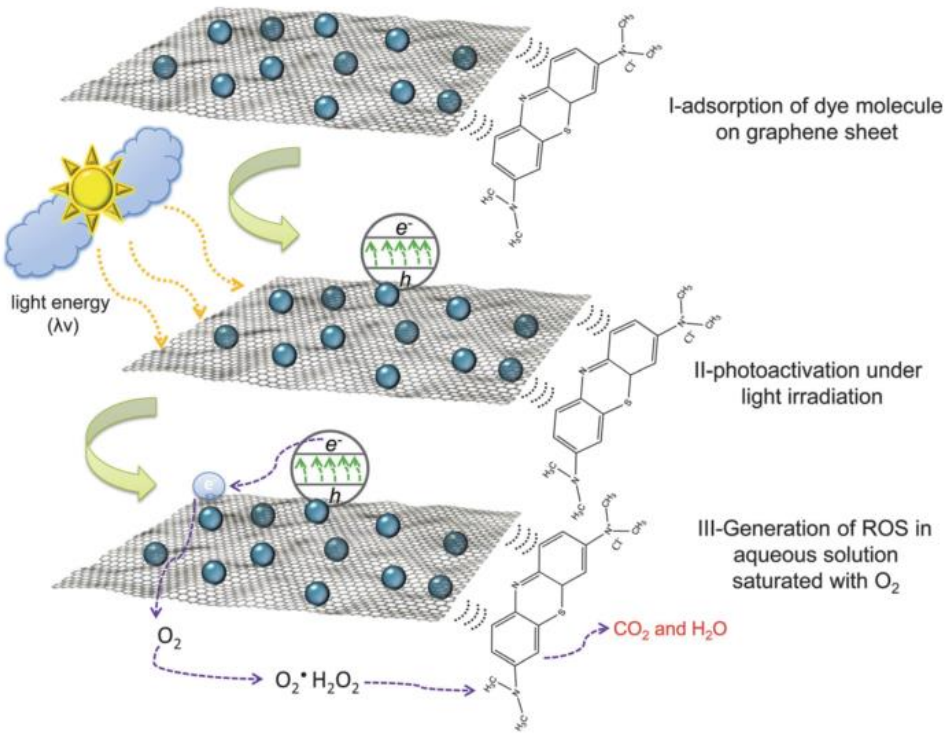

Figure 1.18. Mineralization mechanism of Methylene blue mediated by a graphene-based photocatalyst [Reproduced from Ref. [33] with kind permission of the ACS].

1.7.2 Light-tuning by graphene composites materials.

Besides its role in charge transfer carrier and improved adsorption ability, graphene was also used to extend the light-harvesting of photocatalysts in the solar range, especially when inorganic semiconductors are used as photocatalytic materials. To do this, a strong interaction between graphene derivatives and semiconductors have to be achieved. By chemically binding RGO to P25 through a one-step hydrothermal method, Zhang et al. have extended the light harvesting range of degussa semiconductor (P25) into the visible-light range [52]. Similar results were observed also in a ZnO-RGO composites. For instance, Tien et al. developed a RGO-ZnO sphere composites founded an extension of the absorption edge to the visible light range, most likely due to the formation of Zn−O−C chemical bonds [53].

1.8 Polymer graphene-based photocatalysts.

The use of graphene-based photocatalysts is still facing a series of technical challenges. Among these, the major limitation that prevents commercialization consists in the post recovery of the catalyst particle after water treatment. For istance, TiO_2 nanoparticles have always been applied in a slurry way to obtain high volumetric generation rate of ROS. Since nanomaterials can exhibit serious toxicity for aquatic and human life, at the end of the process catalysts separation is needed, involving also the use of difficult and expensive methods.
On the contrary, the covalent or non-covalent catalyst immobilization in graphene-based materials (in the form of standalone 2D or 3D structures) or in a polymer matrix enables their recyclability and easy removal after the treatment [35]. In this context, polymer graphene-based nanocomposites play a key role in addressing the problems associated to water purification. Due to the inherent remarkable surface properties of the incorporated nanoparticles and also the possibility to obtain thin films, membranes or filters with high stability and processability, polymer graphene-based materials display outstanding potentiality in the disinfection and microbial control of water [54].

A variety of polymer nanocomposites have been investigated and their properties tailored by the combination of different polymers and nanoparticles. Thermoplastic (polymethylmethacrylate, polyvinyl chloride, polystyrene, polyethylene, polypropylene) as well as thermoset (polyurethane, epoxy resin) polymers have been employed mainly in combination with metal oxides (TiO_2, ZnO,CeO_2) nanoparticles used as a filler [55,56].
However, several drawbacks in the preparation of polymer nanocomposites have to be taken into account. For example, polymer substrates that support photocatalyst itself being organic undergo to degradation phenomena under light irradiation. Therefore, a suitable selection of the polymer matrix and nanocomposites formulation has to be made as well. It was demonstrated that formulations involving catalyst well embedded into the polymer matrix are subjected to faster degradation compared with the coated polymer [57].
Regarding the formulation of polymer-based photocatalytic systems, high temperature processes after synthesis to prepare the hybrid, are required to activate the photocatalyst nanoparticles. However, the majority of engineering polymers available to this purpose, degrade at T>300 °C. This limits such application only on those polymers that have very outstanding thermal stability. Conversely, approaches that implied formulation of polymer nanocomposites by using low temperatures such as solvent casting and atomic layer deposition (ALD) techniques can be exploited. In addition, formulation by using organic photocatalysts can be also evaluated.

Conclusions.

In summary, this chapter introduce advantages and limitations use of heterogeneous photocatalysis, considered as one of the most promising alternatives to minimize energy requirements, costs, chemical consumption and potential environmental impact associated with water purification. In this context, graphene-based materials could play a key role in developing photocatalytic composites by coupling with organic and inorganic semiconductors to degrade conventional and emerging pollutants.

References.

[1] United Nations World Water Assessment Programme)/UN-Water. 2018. The United Nations World Water; Development Report 2018: Nature-Based Solutions for Water. Paris, UNESCO;

[2] Jawaid, M., & Khan, M. M. (Eds.). (2018). Polymer-based nanocomposites for energy and environmental applications. Woodhead Publishing;

[3] Alvarez, P. J., Chan, C. K., Elimelech, M., Halas, N. J., & Villagrán, D. (2018). Emerging opportunities for nanotechnology to enhance water security. Nature nanotechnology, 13(8), 634;

[4] Chong, M. N., Jin, B., Chow, C. W., & Saint, C. (2010). Recent developments in photocatalytic water treatment technology: a review. Water research, 44(10), 2997-3027;

[5] Coleman, H. M., Marquis, C. P., Scott, J. A., Chin, S. S., & Amal, R. (2005). Bactericidal effects of titanium dioxide-based photocatalysts. Chemical Engineering Journal, 113(1), 55-63.

[6] Crini, G., & Lichtfouse, E. (2019). Advantages and disadvantages of techniques used for wastewater treatment. Environmental Chemistry Letters, 17(1), 145-155;

[7] Elmolla, E. S., & Chaudhuri, M. (2011). The use of artificial neural network (ANN) for modelling, simulation and prediction of advanced oxidation process performance in recalcitrant wastewater treatment. In Artificial Neural Networks-Application. IntechOpen;

[8] Ameta, S., & Ameta, R. (Eds.). (2018). Advanced oxidation processes for wastewater treatment: emerging green chemical technology. Academic Press;

[9] Pouran, S. R., Aziz, A. A., & Daud, W. M. A. W. (2015). Review on the main advances in photo-Fenton oxidation system for recalcitrant wastewaters. Journal of Industrial and Engineering Chemistry, 21, 53-69;

[10] Hermosilla, D., Cortijo, M., & Huang, C. P. (2009). Optimizing the treatment of landfill leachate by conventional Fenton and photo-Fenton processes. Science of the Total Environment, 407(11), 3473-3481.

[11] Ahmed, S. N., & Haider, W. (2018). Heterogeneous photocatalysis and its potential applications in water and

wastewater treatment: a review. Nanotechnology, 29(34), 342001;
[12] Serpone, N., Emeline, A. V., Horikoshi, S., Kuznetsov, V. N., & Ryabchuk, V. K. (2012). On the genesis of heterogeneous photocatalysis: a brief historical perspective in the period 1910 to the mid-1980s. Photochemical & Photobiological Sciences, 11(7), 1121-1150;
[13] Thandu, M., Comuzzi, C., & Goi, D. (2015). Phototreatment of water by organic photosensitizers and comparison with inorganic semiconductors. International Journal of Photoenergy;
[14] Marin, M. L., Santos-Juanes, L., Arques, A., Amat, A. M., & Miranda, M. A. (2011). Organic photocatalysts for the oxidation of pollutants and model compounds. Chemical reviews, 112(3), 1710-1750;
[15] DeRosa, M. C., & Crutchley, R. J. (2002). Photosensitized singlet oxygen and its applications. Coordination Chemistry Reviews, 233, 351-371;
[16] Macdonald, I. J., & Dougherty, T. J. (2001). Basic principles of photodynamic therapy. Journal of Porphyrins and Phthalocyanines, 5(02), 105-129;
[17] Tan, H. L., Abdi, F. F., & Ng, Y. H. (2019). Heterogeneous photocatalysts: an overview of classic and modern approaches for optical, electronic, and charge dynamics evaluation. Chemical Society Reviews, 48(5), 1255-1271;
[18] Pan, H., Zhu, S., Lou, X., Mao, L., Lin, J., Tian, F., & Zhang, D. (2015). Graphene-based photocatalysts for oxygen evolution from water. RSC Advances, 5(9), 6543-6552;
[19] Sun, J., Zhang, J., Zhang, M., Antonietti, M., Fu, X., & Wang, X. (2012). Bioinspired hollow semiconductor nanospheres as photosynthetic nanoparticles. Nature Communications, 3, 1139;
[20] Zhang, T., Zhang, X., Ng, J., Yang, H., Liu, J., & Sun, D. D. (2011). Fabrication of magnetic cryptomelane-type manganese oxide nanowires for water treatment. Chemical Communications, 47(6), 1890-1892;
[21] Li, H., Bian, Z., Zhu, J., Zhang, D., Li, G., Huo, Y., ... & Lu, Y. (2007). Mesoporous titania spheres with tunable chamber stucture and enhanced photocatalytic activity. Journal of the American Chemical Society, 129(27), 8406-8407;

[22] Li, X., Yu, J., & Jaroniec, M. (2016). Hierarchical photocatalysts. Chemical Society Reviews, 45(9), 2603-2636;
[23] Li, X., Yu, J., Wageh, S., Al-Ghamdi, A. A., & Xie, J. (2016). Graphene in photocatalysis: a review. Small, 12(48), 6640-6696;
[24] Liang, S., Xia, Y., Zhu, S., Zheng, S., He, Y., Bi, J., ... & Wu, L. (2015). Au and Pt co-loaded g-C3N4 nanosheets for enhanced photocatalytic hydrogen production under visible light irradiation. Applied Surface Science, 358, 304-312;
[25] Cao, M., Wang, P., Ao, Y., Wang, C., Hou, J., & Qian, J. (2015). Investigation on graphene and Pt co-modified CdS nanowires with enhanced photocatalytic hydrogen evolution activity under visible light irradiation. Dalton Transactions, 44(37), 16372-16382;
[26] Wang, C., Yue, R., Wang, H., Zou, C., Du, J., Jiang, F., ... & Wang, C. (2014). Dendritic Ag@ Pt core–shell catalyst modified with reduced graphene oxide and titanium dioxide: Fabrication, characterization, and its photo-electrocatalytic performance. International journal of hydrogen energy, 39(11), 5764-5771;
[27] Jiang, J., Yu, J., & Cao, S. (2016). Au/PtO nanoparticle-modified g-C3N4 for plasmon-enhanced photocatalytic hydrogen evolution under visible light. Journal of colloid and interface science, 461, 56-63;
[28] Zhang, J., Wang, Y., Zhang, J., Lin, Z., Huang, F., & Yu, J. (2013). Enhanced photocatalytic hydrogen production activities of Au-loaded ZnS flowers. ACS applied materials & interfaces, 5(3), 1031-1037;
[29] Xiang, Q., Yu, J., & Jaroniec, M. (2012). Synergetic effect of MoS2 and graphene as cocatalysts for enhanced photocatalytic H2 production activity of TiO2 nanoparticles. Journal of the American Chemical Society, 134(15), 6575-6578;
[30] Zhang, J., Yu, J., Jaroniec, M., & Gong, J. R. (2012). Noble metal-free reduced graphene oxide-Zn x Cd1–x S nanocomposite with enhanced solar photocatalytic H2-production performance. Nano letters, 12(9), 4584-4589;
[31] Wang, P., Wang, J., Ming, T., Wang, X., Yu, H., Yu, J., ... & Lei, M. (2013). Dye-sensitization-induced visible-light reduction of graphene oxide for the enhanced TiO2 photocatalytic performance. ACS applied materials & interfaces, 5(8), 2924-2929;

[32] Geim, A. K., & Novoselov, K. S. (2010). The rise of graphene. In Nanoscience and Technology: A Collection of Reviews from Nature Journals (pp. 11-19);
[33] Zhang, N., Yang, M. Q., Liu, S., Sun, Y., & Xu, Y. J. (2015). Waltzing with the versatile platform of graphene to synthesize composite photocatalysts. Chemical reviews, 115(18), 10307-10377;
[34] Pastrana-Martínez, L. M., Morales-Torres, S., Figueiredo, J. L., Faria, J. L., & Silva, A. M. (2018). Graphene photocatalysts. In Multifunctional Photocatalytic Materials for Energy (pp. 79-101). Woodhead Publishing;
[35] Perreault, F., De Faria, A. F., & Elimelech, M. (2015). Environmental applications of graphene-based nanomaterials. Chemical Society Reviews, 44(16), 5861-5896;
[36] Li, X., Cai, W., An, J., Kim, S., Nah, J., Yang, D., ... & Banerjee, S. K. (2009). Large-area synthesis of high-quality and uniform graphene films on copper foils. science, 324(5932), 1312-1314;
[37] Bae, S., Kim, H., Lee, Y., Xu, X., Park, J. S., Zheng, Y., ... & Kim, Y. J. (2010). Roll-to-roll production of 30-inch graphene films for transparent electrodes. Nature nanotechnology, 5(8), 574;
[38] Hummers Jr, W. S., & Offeman, R. E. (1958). Preparation of graphitic oxide. Journal of the american chemical society, 80(6), 1339-1339;
[39] Sreeprasad, T. S., & Berry, V. (2013). How do the electrical properties of graphene change with its functionalization?. Small, 9(3), 341-350;
[40] Suk, J. W., Piner, R. D., An, J., & Ruoff, R. S. (2010). Mechanical properties of monolayer graphene oxide. ACS nano, 4(11), 6557-6564;
[41] Chua, C. K., & Pumera, M. (2014). Chemical reduction of graphene oxide: a synthetic chemistry viewpoint. Chemical Society Reviews, 43(1), 291-312;
[42] Pei, S., & Cheng, H. M. (2012). The reduction of graphene oxide. Carbon, 50(9), 3210-3228;
[43] Gómez-Navarro, C., Meyer, J. C., Sundaram, R. S., Chuvilin, A., Kurasch, S., Burghard, M., ... & Kaiser, U. (2010). Atomic structure of reduced graphene oxide. Nano letters, 10(4), 1144-1148;

[44] Bagri, A., Mattevi, C., Acik, M., Chabal, Y. J., Chhowalla, M., & Shenoy, V. B. (2010). Structural evolution during the reduction of chemically derived graphene oxide. Nature chemistry, 2(7), 581;
[45] Yang, M. Q., Zhang, N., Pagliaro, M., & Xu, Y. J. (2014). Artificial photosynthesis over graphene–semiconductor composites. Are we getting better?. Chemical Society Reviews, 43(24), 8240-8254;
[46] Zhang, N., Zhang, Y., & Xu, Y. J. (2012). Recent progress on graphene-based photocatalysts: current status and future perspectives. Nanoscale, 4(19), 5792-5813;
[47] Yang, M. Q., & Xu, Y. J. (2013). Selective photoredox using graphene-based composite photocatalysts. Physical Chemistry Chemical Physics, 15(44), 19102-19118;
[48] Lightcap, I. V., Kosel, T. H., & Kamat, P. V. (2010). Anchoring semiconductor and metal nanoparticles on a two-dimensional catalyst mat. Storing and shuttling electrons with reduced graphene oxide. Nano letters, 10(2), 577-583;
[49] Zhang, X. F., & Xi, Q. (2011). A graphene sheet as an efficient electron acceptor and conductor for photoinduced charge separation. Carbon, 49(12), 3842-3850;
[50] Wojcik, A., & Kamat, P. V. (2010). Reduced graphene oxide and porphyrin. An interactive affair in 2-D. ACS nano, 4(11), 6697-6706;
[51] Upadhyay, R. K., Soin, N., & Roy, S. S. (2014). Role of graphene/metal oxide composites as photocatalysts, adsorbents and disinfectants in water treatment: a review. Rsc Advances, 4(8), 3823-3851;
[52] Zhang, H., Lv, X., Li, Y., Wang, Y., & Li, J. (2009). P25-graphene composite as a high performance photocatalyst. ACS nano, 4(1), 380-386;
[53] Tien, H. N., Khoa, N. T., Hahn, S. H., Chung, J. S., Shin, E. W., & Hur, S. H. (2013). One-pot synthesis of a reduced graphene oxide–zinc oxide sphere composite and its use as a visible light photocatalyst. Chemical engineering journal, 229, 126-133;
[54] Falcaro, P., Ricco, R., Yazdi, A., Imaz, I., Furukawa, S., Maspoch, D., ... & Doonan, C. J. (2016). Application of metal and metal oxide nanoparticles@ MOFs. Coordination Chemistry Reviews, 307, 237-254;

[55] Di Mauro, A., Cantarella, M., Nicotra, G., Pellegrino, G., Gulino, A., Brundo, M. V., ... & Impellizzeri, G. (2017). Novel synthesis of ZnO/PMMA nanocomposites for photocatalytic applications. Scientific reports, 7, 40895;

[56] Cantarella, M., Sanz, R., Buccheri, M. A., Ruffino, F., Rappazzo, G., Scalese, S., ... & Privitera, V. (2016). Immobilization of nanomaterials in PMMA composites for photocatalytic removal of dyes, phenols and bacteria from water. Journal of Photochemistry and Photobiology A: Chemistry, 321, 1-11;

[57] Bussière, P. O., Peyroux, J., Chadeyron, G., & Therias, S. (2013). Influence of functional nanoparticles on the photostability of polymer materials: Recent progress and further applications. Polymer degradation and stability, 98(12), 2411-2418.

CHAPTER 2

POLYMER PORPHYRIN GRAPHENE-BASED PHOTOCATALYST

As well stated in the previous chapter, photocatalysis represents one of the most promising environmental-friendly solution to purify water. In particular, the combination of graphene (G) with photoactive molecules aims to strongly increase the photocatalytic activity of the hybrid systems by boosting the separation and transfer of photogenerated charges.

In this view, organic photosensitizers, having an excellent visible-light absorption, coupled with the charge transfer properties of G-based materials represent the current hot topic in water treatment. Among these, porphyrins have shown great potential in visible-light photocatalytic applications because of their large extinction molar coefficient aside from the well-defined organic structures with tunable size and morphology [1,2]. Furthermore, their low cost, eco-friendliness and versatility of the molecular syntheses constitute attractive features, both from environmentally and economically point of view. As reported in literature, the molecular architecture of porphyrins, as well as the dimensions and morphologies of their self-assembly aggregates, considerably influence the photocatalytic efficiency (PCE) of such systems [3,4,5], resulting in a fast recombination of their photo-induced electron-hole pairs. To overcome these crucial concern, one of the possible approaches used is the anchoring of porphyrins onto G-based materials via covalent and non-covalent interactions (e.g., π-π stacking, van der Waals and/or electrostatic interactions) [6-15]. This strategy, as well demonstrated by A. Wojcik and P. Kamat [6], facilitates the electron transfer process from porphyrin to G, facilitating a spin forbidden intersystem crossing (ISC) process. This leads to the production of the singlet oxygen ($^1O_2$) considered the most cytotoxic reactive oxygen species (ROS) [2,16]. Nonetheless, although materials obtained are able to introduce the aforementioned benefits, some complications have to be taken into account during the photoreactions, such as the "shielding effect" [17], as well as the radical scavenger activity of G-based materials [18].

In this chapter, an innovative approach to control the porphyrin- and G-related drawbacks will be presented. In particular, the development of a freestanding hybrid nanocomposite by using cyclic porphyrin polymers deposited onto standalone G structures will be described and discussed. The evaluation of several physico-chemical parameters that critically contribute to the PCE are taken into account.

2.1 Freestanding graphene/porphyrin composites

Significant efforts in electron-transfer process have been made by anchoring porphyrins onto G-based materials via covalent and non-covalent interactions (e.g., π-π stacking or van der Waals and/or electrostatic interactions) strategies, which permit to bind molecules to the selected substrate [6,7-15]. However, some complications arise from the use of G-based materials as co-catalysts in photocatalytic nanocomposites formulations. In fact, although these materials generate the benefits discussed in the previous chapter, some tricky features have to be considered during the photodegradation processes, such as the "shielding effect" as well as their radical scavenger activity. The first phenomenon is induced by the content addition of G-based materials as co-catalyst. Due to their opacity, a weakening of the light irradiation depth through the G-based composites restricts the efficiency of G in promoting the photoactivity [19]. This intrinsic negative effect imposes a weight addition ratio of G derivatives into the composite lower than 5%. However, greater amounts of carbon materials would be necessary to inhibit the recombination of electron-hole pairs photogenerated by the photocatalyst [19]. In covalently graphene oxide (GO) and reduced graphene oxide (RGO) functionalized composites, an increasing number of photoactive sites are clearly related to an improving of photocatalytic efficiencies. To boost the number of such sites, it is indispensable to increase the weight addition ratio or, alternately, the oxidation points onto the G surface. The latter introduces significant structural defects that strongly affects the electron mobility and thus the charge-transfer and separation processes. Furthermore, a huge adsorption capacity against organic contaminants in water is displayed from oxidized G-based materials. This peculiar property, that in the case of GO versus MB dye was quantified at 714 mg/g [20], makes difficult to discern between adsorption and photodegradation processes during photocatalytic tests. Another crucial point is related to the antioxidant activity of carbon materials versus organic molecules. Multiple experiments have shown that G-based materials are an effective scavenger of $OH^{\bullet}$ radicals in water. The latter entrapped onto G structure are no longer available to degrade pollutant, avoiding the desired purification process. More importantly, the final composite materials must be easy removed after the treatment.

An innovative approach able to overcome all the aforementioned drawbacks, consists in the preparation of a freestanding hybrid nanocomposite by combining supported high-quality G and photoactive porphyrin derivatives. The novelty of this approach involves the exploitation of extensive non-covalent interactions between the high surface area of G co-catalyst and a coating of porphyrin polymers. However, the effect of physico-chemical parameters used to prepare the material can influence the photocatalytic ability. In the next sections the role of the solvent used for the polymer deposition, the morphology of the G support, and the porphyrin polymers molecular weight as well as their architecture will be reported and discussed.

2.1.1 Porphyrin polymers as photoactive phase

The heterogeneous catalysis from porphyrins and metal-porphyrins under visible-light irradiation is well reported in the literature [2]. Porphyrin systems can act as photocatalytic media in form of free molecules, supported molecules, nanostructured assemblies and thin films [2,3,7,8]. Whatever is the strategy adopted, the formation of porphyrin agglomerates triggers the rapid quenching of excited state preventing photocatalysis. A good strategy to overcome the porphyrin-related problems in the preparation of G-based composites can involve the use of porphyrin polymers. In particular, their use promotes an intimate and extensive contact at the G interface, compared with merely porphyrin molecules. Indeed, the polymer coating is able to protect graphene materials to the direct exposure of light, dyes and $OH^{\bullet}$ radicals, which drastically reduce the PCE. On the other hand, the use of cyclic porphyrin polymers thanks to their peculiar chemical structure, can offer new perspectives in exploiting porphyrin derivatives as photoactive compounds.
To mitigate the aggregation phenomena among porphyrin units, the use of specific sterically hindered polyporphyrins may increase the number of photoactive sites, limiting also the formation of agglomerates, and as a result, boosting the desired charge-transfer process onto the G surface. To this purpose, a co-polymerization process between porphyrin monomer (5,10-di[p-(9-methoxytriethylenenoxy)phenyl]-15,20-di[p-hydroxyphenyl) and 1,20-di(bisphenoxy-A) eicosane to concatenate higher number of photoactive sites in more stable cyclic chain structures was used to

develop cyclic porphyrin polymer [21-24]. Additionally, two hampering pendant groups in 5 and 10 positions for each molecule [see **Figure 2.1**] were introduced with the aim to reduce the coordination and aggregation with other porphyrin molecules. In **Figure 2.1** the synthetic pathways of polymerization for porphyrin copolymer (CPC) were depicted. The synthetic details of polymerization reactions of CPC is reported in the experimental section. The obtained material was purified and characterized by Matrix Assisted Laser Desorption Ionization Mass Spectrometry (MALDI-TOF MS) (see **Figure 2.2**). The **Table 2.1** reports the molar mass (MM) values of CPC calculated by using gel permeation chromatography (GPC) analysis. A total content of 37% of porphyrin into the CPC was estimated by using UV-Vis method (**Table 2.1**).

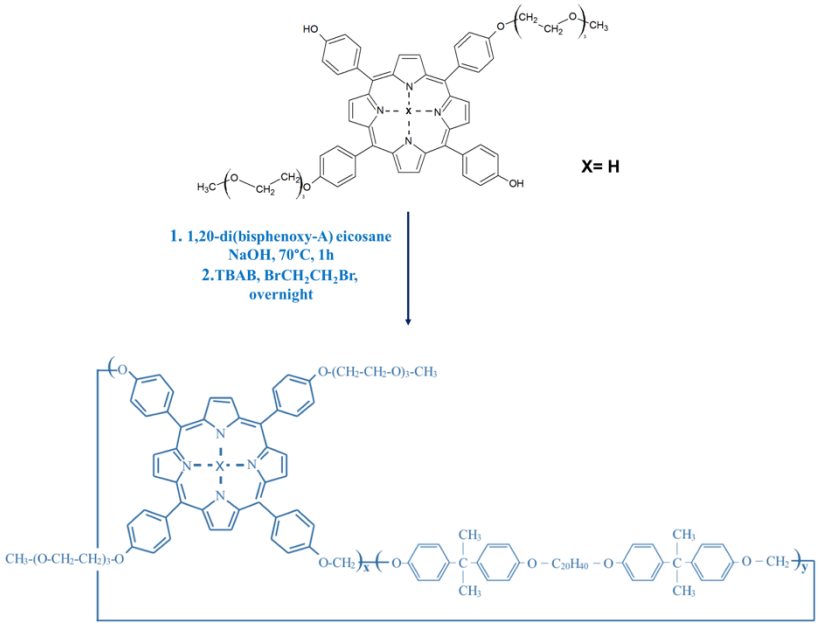

Figure 2.1 Scheme of reaction for the preparation of CPC .

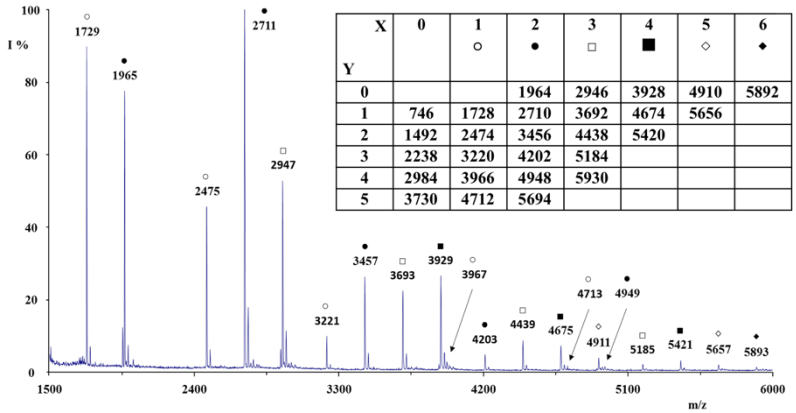

X / Y	0	1 ○	2 ●	3 □	4 ■	5 ◇	6 ◆
0			1964	2946	3928	4910	5892
1	746	1728	2710	3692	4674	5656	
2	1492	2474	3456	4438	5420		
3	2238	3220	4202	5184			
4	2984	3966	4948	5930			
5	3730	4712	5694				

Figure 2.2. Positive MALDI-TOF mass spectrum, acquired in reflection mode, CPC and structural assignments.

Table 2.1

Composition, yield and Molar Masses of synthesized CPC

Polymer	Nominal % Porphyrin molar content	Actual % Porphyrin molar content	Polymer yield (w/w)[a]	Mw[b]	Mn[b]
Porph-copolymer	50	37,5	75%	10586	9241

a) Percent of polymeric material with respect to the total number of starting monomers

b) Molar masses values calculated by using PMMA as GPC standards.

2.2 The role of the solvent in graphene/cyclic porphyrin copolymer preparation

The complexity of interactions between polymer chains as well as polymer–solvent, play a key role on the materials morphologies and distribution before and after cast deposition. Therefore, the solvent selected to perform the deposition onto G assumes a relevant importance in the photocatalytic performance, depending on the morphology as well as macromolecule substrate interactions [25]. As reported also in the recent literature [6], a strong interactive affinity between porphyrin and G material exists both in solution as well as in films, thus it cannot exclude as a determinant factor the solvent effect during the graphene/polymer interface formation. In light of this, the influence of the solvent used to prepare the hybrid materials are here reported. To this purpose, the CPC was dissolved in three different solvents: chloroform ($CHCl_3$), tetrahydrofuran (THF) and dimethylformamide (DMF), and used to impregnate via bath deposition 2D-G. Depending on the nature of the solvent, a different behavior of CPC was observed and, as a consequence, a different coating on the G surface was produced. UV-Vis spectra as well as the microscopic and nanoscopic features of CPC after the deposition will be described and correlated with the photocatalytic activity of the three samples by using Methylen Blue (MB) degradation test.

2.2.1 UV-Vis spectrometric analysis of cyclic porphyrin copolymer in three solvents

Free-base porphyrins UV-Vis spectra show an intense near-UV Soret band and visible Q bands [26]. The UV-Vis spectra of porph-copolymer with a concentration of about 1×10^{-6} M are shown in **Figure 2.2**. Data revealed that the Soret band of copolymer is slightly shifted from 420 nm in $CHCl_3$ to 421 nm in THF and 423 nm in DMF according with the behavior of corresponding monomer in the same solvent. As expected, the changes in wavelength are ascribed to the different physicochemical properties of the solvents. A list of the solvent parameters that affect the absorption values is displayed in **Table 2.2**. The solvatochromic shift of copolymer can be influenced by the acceptor number (AN), hydrogen-bonding donor and acceptor capacity

(α and β parameters respectively), and π* that describes the polarity and polarizability of the solvent [27]. Chloroform shows a weak β value, while THF and DMF are strong acceptors of hydrogen bonding.

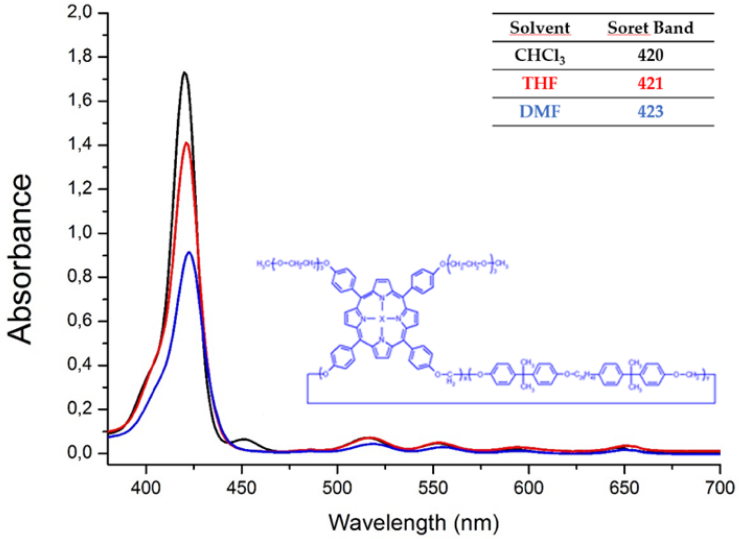

Figure 2.3. The UV-Vis spectra of CPC recorded with $CHCl_3$ (black line), THF (red line) and DMF (blue line).

However, DMF shows a greater π* and DN as well. Depending on the chemical structure of the dissolved species, the contribution of these parameters can lead to significant changes in macromolecule-solvent interactions and, as a consequence, in the polymer coating. In fact, polymers having a great number of oxygen atoms (electrons donors) possess a better affinity versus THF and DMF with a soret band shifted to longer wavelengths than $CHCl_3$.

Table 2.2 The properties of $CHCl_3$, THF and DMF

Solvent	ε_g	DN	AN	π*	β	α	VP
$CHCl_3$	4.7	4.0	23.1	0.58	0.10	0.20	212
THF	7.58	20	8.0	0.58	0.55	0.00	19.3
DMF	36.7	26.6	16.0	0.88	0.69	0.00	0.38

As well described for the porphyrin moieties, depending on the solvent used, the bathochromic effects could be also associated with a different energy gap from the ground to the excited state. DMF being a dipole non-proton solvent, shows a greater static dielectric permittivity (εg) than the $CHCl_3$ (see **Table 2.2**). Accordingly, when DMF is used as a solvent, reduction in the energy gap of the porphyrin moieties [26] occurs, decreasing the energy gap for the transition process from the ground to the excited state. We can reasonable suppose that in the same manner the electron transfer process on the G surface is favorited.

2.2.2 Formulation and morphological characterization of the hybrid systems

The hybrid nanocomposites were prepared by immersing 2D-G samples in three different polymer solutions, testing the degradation of MB under visible-light irradiation (see **Scheme 2.1**). Morphological and physicochemical characterizations are reported as follows.

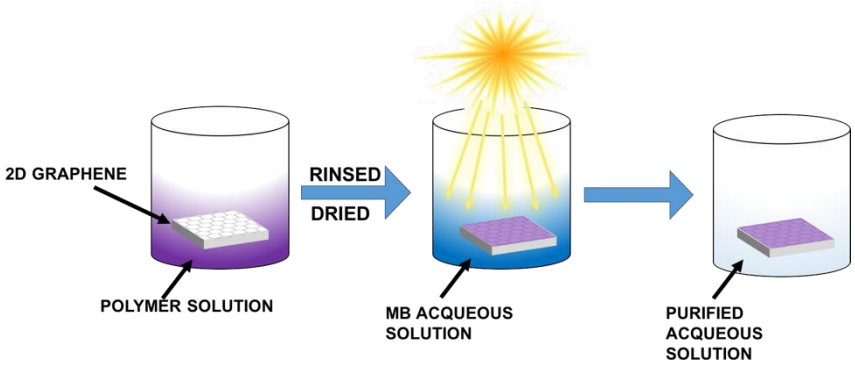

Scheme 2.1. Schematic description of the exsperiment. 2D graphene samples were dipped in three different polymer solutions, rinsed and dried. The as prepared materials were tested by degrading MB under visible-light irradiation.

The copolymer morphology after deposition by casting method onto pristine 2D graphene in the three different solvents was studied, by using scanning electron microscopy (SEM) in (**Figures 2.4** and **2.5**, Atomic Force Microscopy (AFM) in **Figures 2.6**, **2.7** and **2.8** and UV−visible diffuse reflectance spectra (DRS) reported in **Figure 2.9**. As a whole, comparing with the pristine graphene reported in **Figures 2.4 (a)**, from the micrograph in **Figures 2.4 (b)**, it can be seen how the microstructures of the macromolecular film produced by $CHCl_3$ solvent casting, are different from those obtained by using THF [**Figures 2.4 (c)**] and DMF [**Figures 2.4 (d)**].
To evaluate the thickness, the uniform distribution and the adhesion of the copolymer onto the graphene substrate in the three cases, cross-section analyses were performed. **Figures 2.5 (a)-(f)** showed significant differences can be noted between the three samples. Modifications are surely ascribed to the chemical and physical properties of the solvents (see **Table 2.2**). In particular, the reported parameters in **Table 2.2** influence the molecule-solvent as well as the molecule-substrate interactions playing a key role on the covering process. The thickness of polymer coating range roughly from 50 to 210 μm.
$CHCl_3$ leads to a fast evaporation rate of the solvent. Thus, polymer hemispheres formed, rapidly crack to produce circular holes [see **Figure 2.4 (b)**] on the substrate. Therefore, from the inspections of the

cross-section reported in **Figures 2.5 (a)** and **(b)**, a weak polymer-substrate interaction at the interface was achieved. In this case, it can be supposed that hydrogen bonding between the copolymer and the solvent (with great α capacity) promoted. Furthermore, the high volatility of $CHCl_3$ reduced the possibility to establish π-π interactions among aromatic porphyrin moieties of the copolymer and the graphene layer, producing self-aggregation phenomena.
THF, on the other hand, that is an acceptor of hydrogen-bonding (β=0,55) with a small value of polarizability, can lead to better polyporphyrin-graphene interactions [see **Figures 2.5 (c)** and **(d)**]. According to the lower vapor pressure value of THF, polymer hemispheres formed during evaporation are not subjected to the rapid cracking phenomena [see **Figure 2.5(d)**] and consequently, circular holes are not produced.
The polymer coating by using DMF solution presents a different morphology if compared with the previous two samples. In **Figure 2.4 (d)** and in **Figures 2.5 (e)** and **(f)** the coating appears smooth with a good polymer-graphene adhesion, without the formation of hemispheres, resembling the morphology of pristine graphene in **Figure 2.4 (a)**. These evidences are coherent with the DMF chemical properties. The latter having the highest ε_g, AN, DN, β, prevents the aggregates formation, especially if compared to $CHCl_3$. Furthermore, thanks to the lowest vapor pressure value, the copolymer can assemble in its more stable configuration onto graphene. Consequently, the macromolecule-substrate non-covalent bonds result was favorited and a more adhesive film can be observed [**Figure 2.5 (f)**].

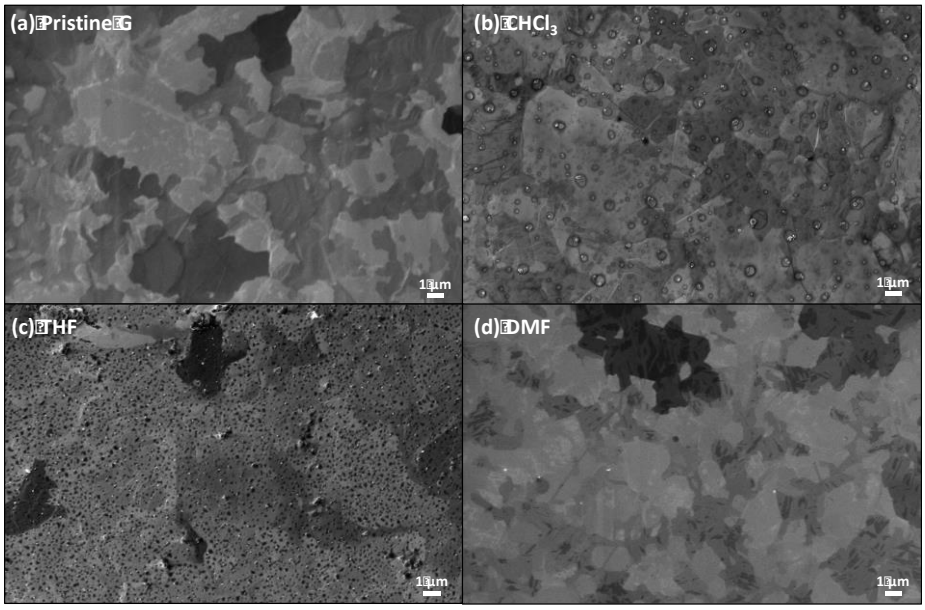

Figure 2.4. SEM images of (a) pristine 2D-G and the CPC coating by using (b) $CHCl_3$, (c) THF and (d) DMF.

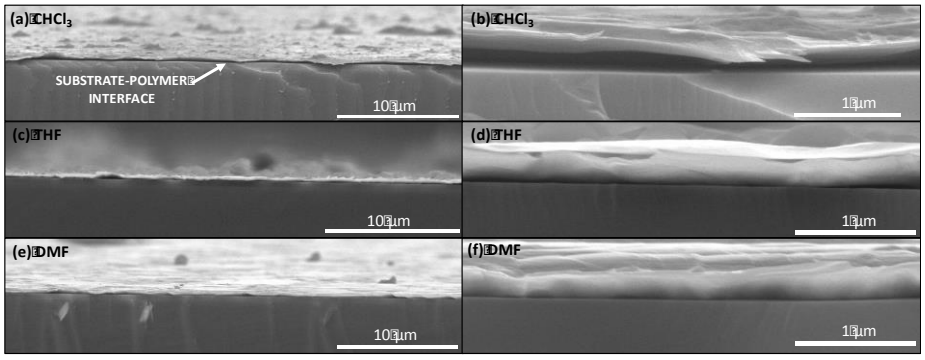

Figure 2.5. SEM in cross-section images of the CPC on 2D-G samples at lower magnification by using (a) $CHCl_3$, (b) THF and (c) DMF and at higher magnification by using (d) $CHCl_3$, (e) THF and (f) DMF.

To further explore the morphologies and appreciate the roughness parameters of the copolymer coating onto the 2D graphene surface, AFM analysis was also performed. **Figure 2.6 (a)** and **Figure 2.7** report

the two dimensional and three dimensional views of the pristine graphene, respectively. Ni polycrystalline structure is clearly recognizable: Ni micrometric grains and corresponding grain boundaries are visible. At this scale, due to the grain boundaries and structuration of their morphology, the height scale spans from 0 to 140 nm and the surface roughness is very high. The surface roughness was quantified by the Root Mean Square (RMS) width σ = <z(x,y)2>1/2 being z(x,y) = h(x,y)-<h(x,y)> with h(x,y) the height function and <z(x,y)> the spatial average over a planar reference surface. For this sample, it resulted on this scan scale, 18.3 nm. **Figures 2.6 (b)-(d)** shown two-dimensional AFM images of the sample surfaces. In particular, to gain information on the films uniformity on a large scale, **Figures 2.6 (b)-(d)** report 20 μm×20 μm AFM scans.

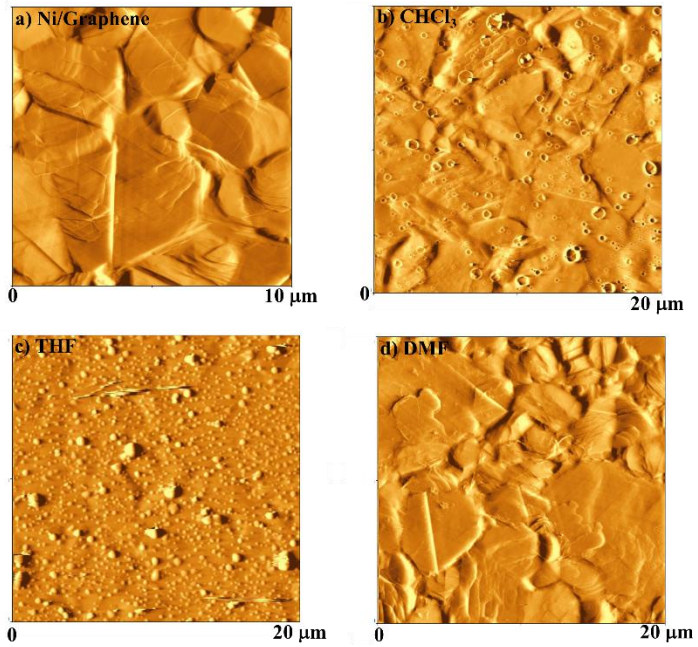

Figure 2.6. (a) 10 μm×10 μm scan of 2D-G and 20 μm×20 μm scans with copolymer deposited by using (b) $CHCl_3$, (c) THF and (d) DMF.

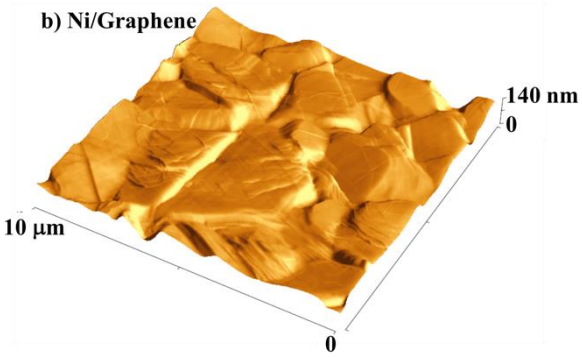

Figure 2.7. 10 μm×10 μm three-dimensional AFM images of 2D-G (on top) surface.

The AFM images confirm the previous results observed by SEM. In particular, **Figure 2.6 (b)** shows that the deposition of the polymer by using $CHCl_3$, leads to a holed film, which conformally covers the G surface, accordingly with previously, discussed results. The underlying Ni surface (i.e. Ni grains and grain boundaries) is still visible, indicating that the thickness (i.e. amount) of the polymer film is not so high to fill the valley regions between the Ni grains. It, instead, follows conformally the Ni surface morphology. The 2 μm×2 μm AFM scans in **Figure 2.6 (a)** allow a closer inspection of the polymeric film morphology: apart from the circular holes, it is continuous over the substrate surface. The diameter of these holes ranges from a minimum of some tens of nanometers to a maximum of some hundreds of nanometers. On the other hand, the depth of the holes ranges from a minimum of about 2-3 nm to a maximum of about 30 nm. The AFM line profile of a hole is reported allowing the measurement of a hole depth of about 30 nm. Furthermore, the edge of the holes presents a rim, which is elevated with respect to the neighboring flat film (see, also, the hole-line section). Using the 2 μm×2μm AFM scan, a surface roughness of 5.9 nm was evaluated and representative of the roughness of the holed polymeric films on a region confined within a Ni grain (on this scale it is not altered from the Ni grain boundaries).
Figure 2.6 (c) shows that the deposition of the polymer film obtained by using THF solvent. The latter produces a thicker film able to underly Ni substrates that is no more recognizable. In this case, it is clear that the polymer fills the valley regions between Ni grains with a uniform coating for the entire substrate hiding any characteristic features of the

original surface. Accordingly, with the SEM analyses, hemispherical polymeric structures are formed. Their presence is more evident in the 2 μm×2 μm AFM scans reported in **Figure 2.8 (c)**. The diameter of these hemispheres ranges from a minimum of some tens of nanometers to a maximum of some hundreds of nanometers. On the other hand, height of these hemispheres ranges from a minimum of about 50 nm to a maximum of about 300 nm. AFM line profile of a selected hemisphere is reported in **Figure 2.8 (d)** allowing the measurement of a structure height of about 60 nm. Using the 2 μm×2 μm AFM scans for THF sample a surface roughness of 24.7 nm was evaluated. This value can be compared to the 5.9 nm roughness value (by the same scan length) for the polymeric film deposited by $CHCl_3$. The higher surface roughness arises from the very high standard deviation on the distribution of the heights of the hemispherical structures (higher than the standard deviation on the distribution of the depths of the holes in the previous sample).

DMF polymer solution [see **Figure 2.8 (d)**] leads to a thinner film if compared with the previous samples. In fact, considering the reference sample, from these pictures, the morphology of the underlying Ni substrate is clearly recognizable without any appreciable difference. However, the 2 μm×2 μm AFM scans [**Figure 2.8 (e)**] report a surface structuration related to the polymeric film presence. In this case, the polymeric film is smooth over the substrate surface. It forms localized wire-like and globular-like structures. AFM line profile of a globular structure is reported in Figure 5 (e) allowing the measurement of a structure height of about 69 nm. However, from the 2 μm×2 μm AFM scan, the surface roughness is evaluated in 4.7 nm, lower than the roughness (on the same scan length) of the previous THF and $CHCl_3$ samples.

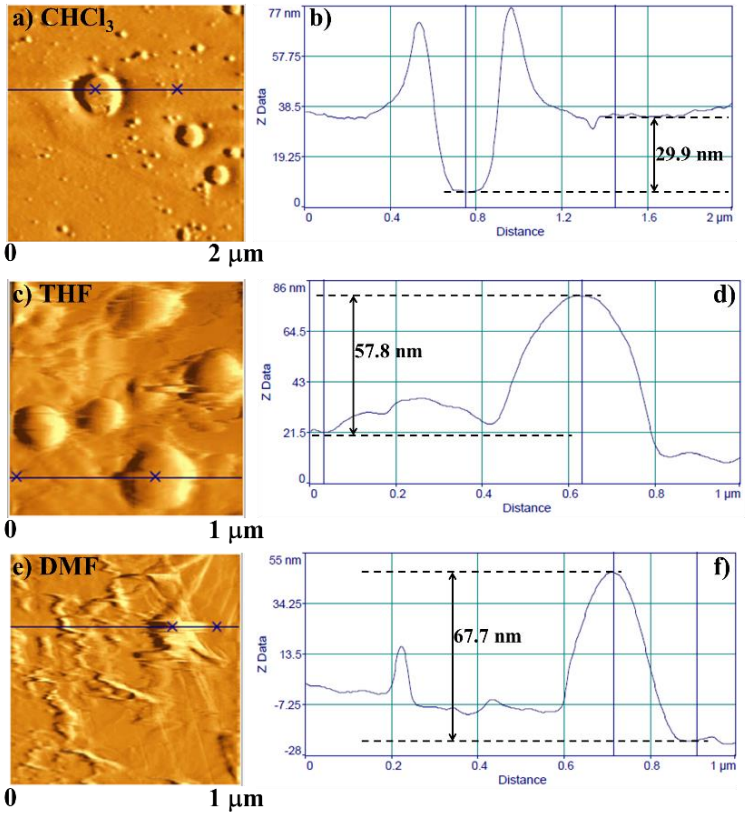

Figure 2.8. Topographic AFM images at 2 μm×2 μm scans with their specific AFM line profiles of CPC deposited onto 2D-G by using (a) $CHCl_3$, (c) THF and (e) DMF as a solvent.

These data further support as the physicochemical properties of the three solvents significant affect the polyporphyrins self-assembly before and after the evaporation, influencing also the G-porphyrin interactions during the deposition process. $CHCl_3$ and THF show the same roughness and similar morphologies, differing from each other for the holes and the hemispherical structures respectively.
In conclusion, from a comparison of the three solvents used to cast the copolymer, both SEM and AFM data showed as DMF forms nanodomains that can be related with G-porphyrin non-covalent interactions.

Diffuse reflectance spectroscopy (DRS) spectra were also performed in the range of 200 -1100 nm to in deep investigate the effect of the polymer deposition onto the graphene surface depending on the specific solvent used. As it is possible to appreciate from **Figure 2.9 (a)** and **Figure 2.9 (b)** a blue shift of the porphyrin diagnostic bands were observed for $CHCl_3$ and THF samples respectively. This behavior could be related to the formation of non-photoactive H-type aggregations that drastically reduce their photo-ability, in agreement with our photocatalytic results [27].

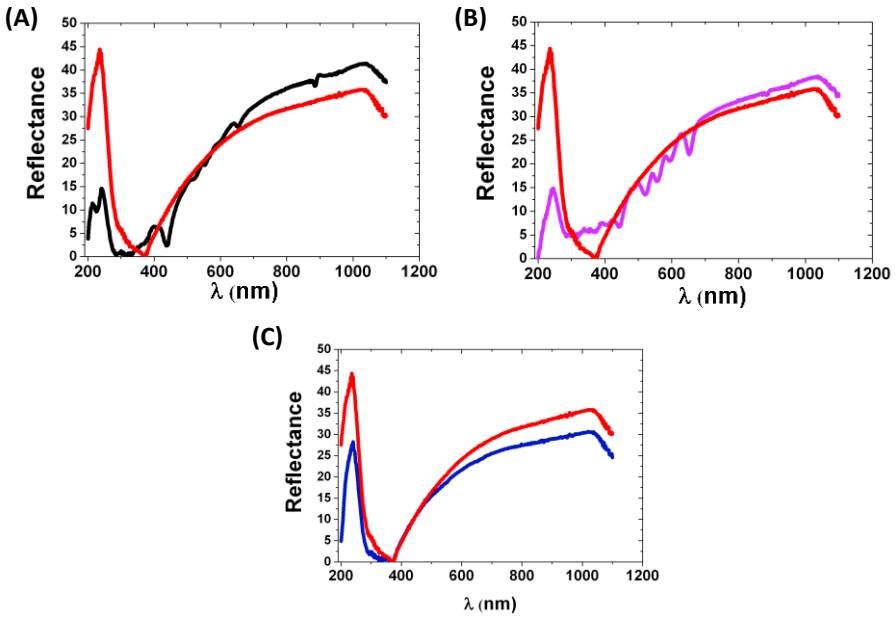

Figure 2.9. UV-Vis reflectance spectra of (a) CPC $CHCl_3$ (black line), (b) CPC THF (purple line) and (c) CPC DMF (blue line). UV-Vis reflectance of the 2D-G substrate is reported in each spectra (red line).

Whereas, in the DRS of DMF copolymer [**Figure 2.9**], absorption in the diagnostic UV-Vis region of the spectrum is not evident, even if compared with the 2D substrate a different diffuse reflectance is clearly evidenced. The disappearance of typical porphyrins signals is most likely due to a thinner film formed by DMF sample also revealed by the morphological analyses.

2.2.3 Photocatalytic Activity

To correlate the effect of the solvents and the photocatalytic performances, the 2D graphene samples coated by using THF, $CHCl_3$ and DMF were subjected to photocatalytic experiments by using the MB degradation test under visible light irradiation. The variation of MB concentration was spectrophotometrically evaluated observing the absorption bands at 664 nm. **Figure 2.10 (a)** reports the C/C_0 values (where C and C_0 are the actual and starting MB concentrations, respectively) of MB as a function of the time. It is important to highlight that the amount of polyporphyrin that coats the 2D substrates (1.5×1.5 cm) is lesser than 0.13 mg. To obtain an accurate correlation between morphological and photocatalytic data, the related characterizations were performed by using the same sample. Given that, in these experiments our aim was to find the best data among the used solvents, being not relevant to the absolute values. In addition, if compared with other photocatalytic systems [28,29] in this stage we performed all the experiments by using freestanding devices, without stirring and/or bubbling air into the solution [28,30].
As expected from SEM and AFM analyses, the best result in terms of photocatalytic activity is showed by the DMF sample, which reaches a degradation efficiency of 17% (see **Figure 2.10**).

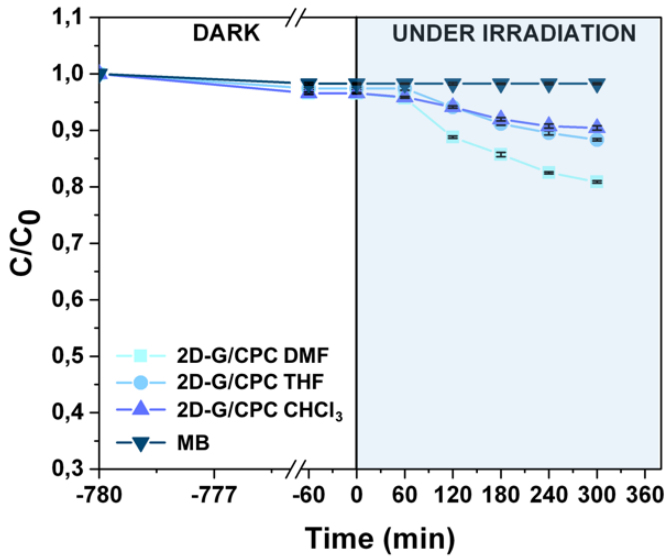

Figure 2.10. UV-vis spectral degradation of 1,5x10^{-5} M MB aqueous solution of 2D-G/CPC in $CHCl_3$ (blue triangle up), THF (blue circle) and DMF (blue square)

2.2.4 Influence of operational conditions

Devices obtained from DMF polymer casting were subjected to photocatalytic experiment by stirring and/or bubbling air. As showed in **Figures 2.11 (a)** and **(b)**, the changes in the experimental set up greatly contribute to boost the photocatalytic degradation of MB dye. In particular, taking into account the mechanism of ROS formation (see section 1.4.1), the achievement of 55% after addition of air-bubbling along with stirring, suggests the formation of singlet oxygen and/or superoxide anion radicals as ROS species during photocatalysis.

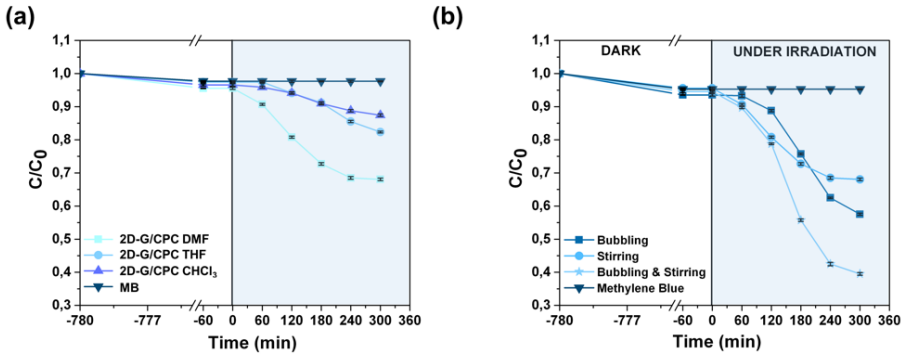

Figure 2.11. UV-vis spectral degradation of $1{,}5x10^{-5}$ M MB aqueous solution of (a) 2D-G/CPC in $CHCl_3$ (blue triangle up), THF (blue circle) and DMF (blue square) under stirring and (b) 2D-G/CPC DMF under stirring (blue circle), under bubbling (blue square) and under stirring&bubbling (blue star).

2.3 Tridimensional graphene in polymer composites preparation.

Although the obtained results opened new perspectives in the exploitation of G-based materials for water purification applications, further improvements can be achieved by changing the 2D-G support with a tridimensional (3D-G) one. In particular, this support allows the growth of a 3D-G macroscopic structure with a continuous and well interconnected graphene sheets network [graphene foam (GF)], resulting in GF and GF-based composites with improved electrical, mechanical and adhesive properties [22]. Furthermore, GF offers the advantage to possess a very high exposed surface area (~850 m^2/g) allowing to obtain higher area for polymer coating, thus increasing the number of photoactive sites. In light of this, GF photoactive composites preparation, characterization and applications will be discussed, comparing also the results with previous ones.

2.3.1 Synthesis of graphene foam and characterization.

The GF was obtained by chemical vapor deposition (CVD) growth (see **Appendix 1**). Nichel foam template (pieces of 1 cm^2) were heated up to 1000 °C for 20 minutes under Ar, H_2 and CH_4 flows (600, 1000 and 20 sccm, respectively) and then cooled down at 15 °C min to grow the

graphene layers on the Ni foam surface. The obtained GF sample was analyzed and characterized by SEM at progressive magnifications [**Figure 2.12 (a)-(c)**] and Raman spectroscopy [**Figure 2.12 (d)**]. It was evident that the graphene film adheres to the surface of the nickel foam, reproducing its morphology, but it showed a non-homogeneous distribution, as evidenced by the different grey contrasts over the sample. The lower contrast was due to a different quality of the graphene film formed, confirmed by Raman spectra [**Figure 2.12 (d)**] that evidenced the typical G and 2D peaks of either in the brighter and darker regions. The irregular distribution of graphene (going from monolayer to multilayers) is well known on nickel substrates, due to the graphene growth process occurring by carbon segregation and precipitation that makes it difficult to control its thickness and uniformity [31]. Indeed, this growth mechanism is not self-limiting like on copper.

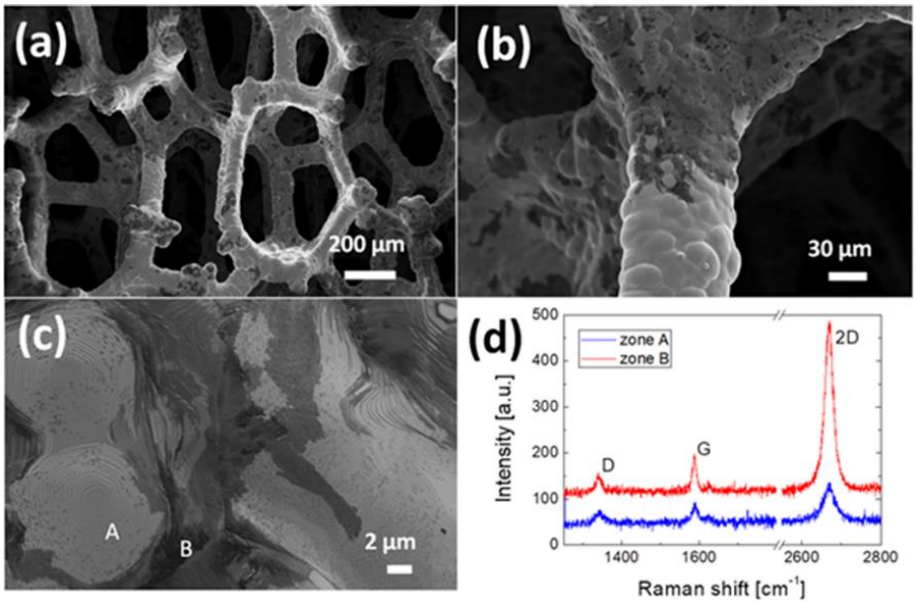

Figure 2.12. (a – c): SEM images obtained in the Inlens mode of the nickel-graphene foam at different magnifications; (d): Raman spectra obtained on different areas of the foam with different grey contrast (e.g. zone A and B of panel (c)).

Although GF produced from Nickel-foam template shows a non-homogeneous high-quality graphene, the peculiarity of its high surface area, tunable porosity, outstanding electron-transfer properties allows the formulation of hybrid graphene-based polymer composites with excellent performances in photocatalytic applications as well demonstrated in the next sections.

2.4 Porphyrin homo-polymers studies

To take advantage in terms of photocatalytic efficiencies as well as to find and discriminate some differences in photochemical behaviors, porphyrin polymers similar to those of copolymer were prepared. In particular, the same starting monomer and a Zn porphyrin monomer derivative were selected. The latter was chosen for its considerable interest in photocatalytic applications [5,10]. Thus, porphyrin polymer containing 100% of porphyrin units, also called cyclic porphyrin homopolymer (CPH), was prepared, and the synthetic procedure reported in **Figure 2.13**.

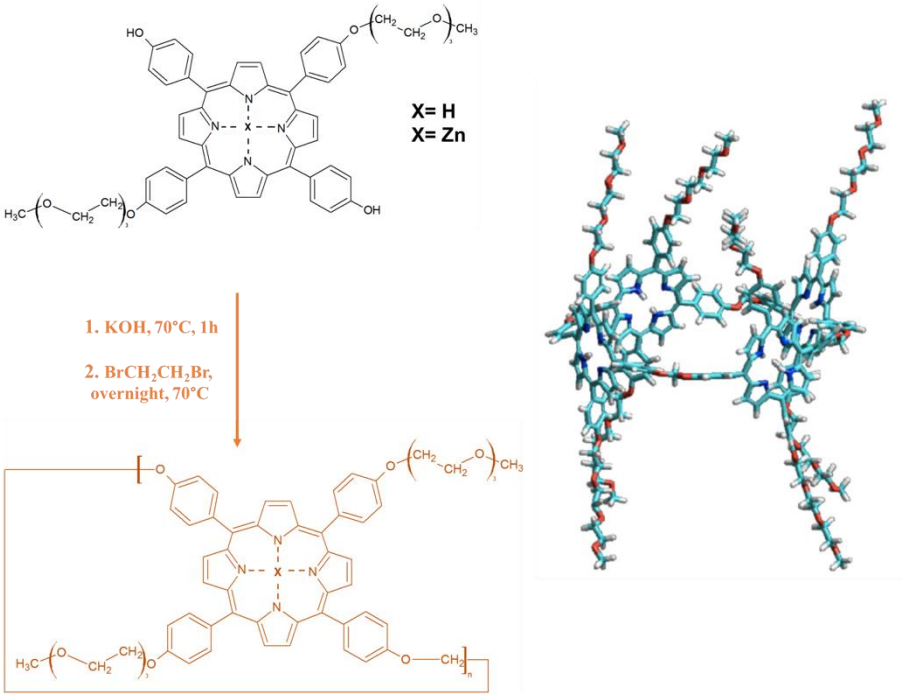

Figure 2.13. Preparation of CPH and Zn-CPH. Molecular model of cyclic tetramer of Poly trans-Prs (as example of CPH conformational structure, reproduced from Ref [23] with kind permission of Elsevier)

The obtained polymers were purified and characterized by MALDI-TOF MS and GPC. MALDI-TOF analysis, performed after samples purification, indicated that Zn derivate (Zn-CPH) contained oligomers up to 3 repeat units, whereas polymerization of Zinc-free CPH, displayed a higher number of porphyrin units along the cyclic chains (see **Figure 2.14**).

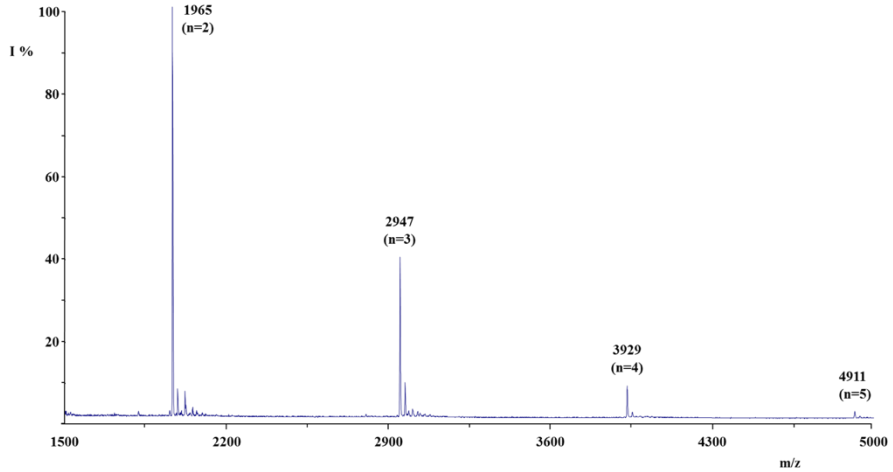

Figure 2.14. Positive MALDI-TOF mass spectrum, acquired in reflection mode of CPH.

The GPC data, calculated by using PMMA as a standard, reported the Mass average molar mass (Mw) value for CPH of 4932, lower than of CPC (10586).

2.4.1 Formulation and characterization of freestanding graphene foam/porphyrin polymer nanocomposites

Nickel foam covered by G was embedded with the polymeric photosensitizers were formulated. GF pieces of about 5 mm × 20 mm were characterized by SEM, and weighted. The GF composites were formulated by dissolving known amounts (~10 mg) of each polymer sample (CPH and CPC) in 1 mL of DMF. After, the GF pieces were immersed into the obtained solutions overnight, removed from the vials and dried under vacuum at 50°C [**Figures 2.15 (a)-(c)**]. The obtained materials were weighted again to estimate the amount of cyclic porphyrin polymers non-covalently attached to the GF surfaces. In both cases (CPH and CPC), the weights registered after deposition indicated amounts lesser than 0,4 mg. To gain information on the strenght of the non-covalent bound at the interface, samples were washed several times by using fresh DMF and $CHCl_3$. After, XPS analyses were performed.

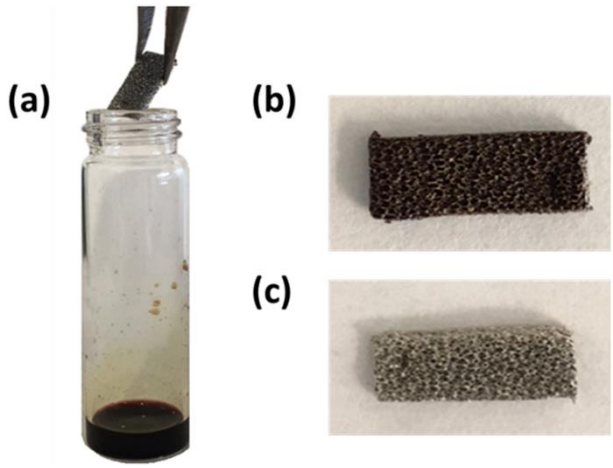

Figure 2.15. Formulation of GF/polymer nanocomposites: (a) the immersion of GF in porphyrin-polymer solutions, (b) dried GF/CPH and (c) dried GF/CPC samples.

Data on the surface composition of both porphyrin-based freestanding devices were collected. The wide range XPS spectra (survey) related to the GF/CPH and GF/CPC composites are shown in the left panel of **Figure 2.16**. As showed, both the survey spectra evidenced the

presence of carbon and oxygen species, as expected. The nitrogen contribution, instead, is not visible because of the low amount in both the nanocomposites (see **Table 2.3**).

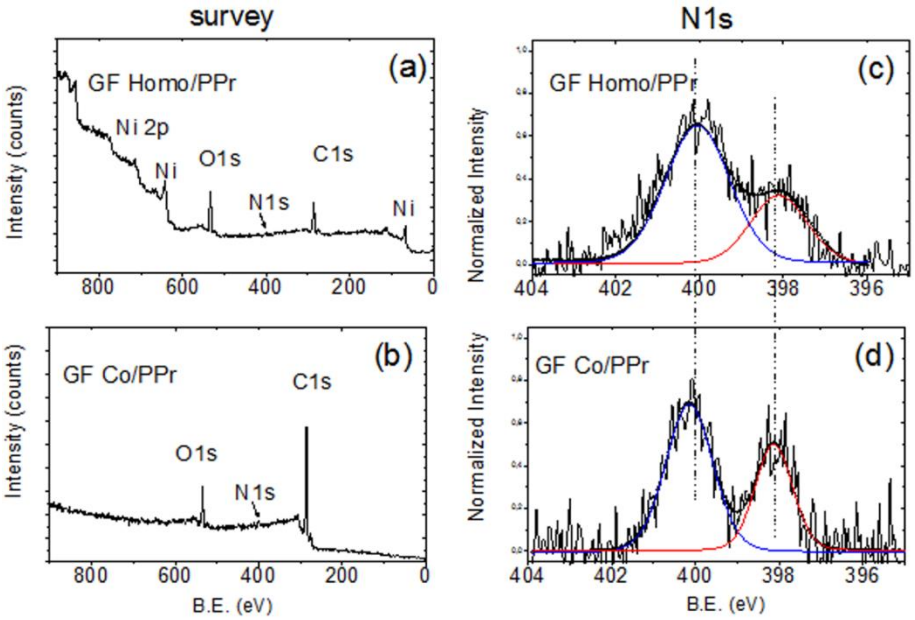

Figure 2.16. Left panel: wide range XPS spectra (survey) of (a) GF/CPH and (b) GF/CPC; Right panel: high resolution N1s XPS spectra of (c) GF/CPH and (d) GF/CPC.

Table 2.3
XPS relative atomic percentages as obtained by the spectra of GF/CPH and GF/CPC

	C 1s (%)	O 1s (%)	N 1s (%)	Ni 2p
GF/CPH	57.8	30.5	2.7	9.0
GF/CPC	86.3	11.2	2.0	<0.5

The spectral signals from the nickel substrate are visible only in in GF/CPH sample, thus indicating that in the case of the CPC, a

smoother coating was produced on the Ni-graphene surface than in the homopolymer. The elemental percentages reported in **Table 2.3** showed that the amount of carbon is significantly higher in the case of GF/CPC than in GF/CPH. This finding was in agreement with the molecular structures of the two compounds sketched in **Figure 2.1**, having the copolymer long organic spacers between the porphyrin units. In order to inspect the electronic structure of porphyrin-based compounds, the high-resolution regions related to the N1s and C1s signals (see **Figures 2.16 and 2.17**) were investigated [32,33].

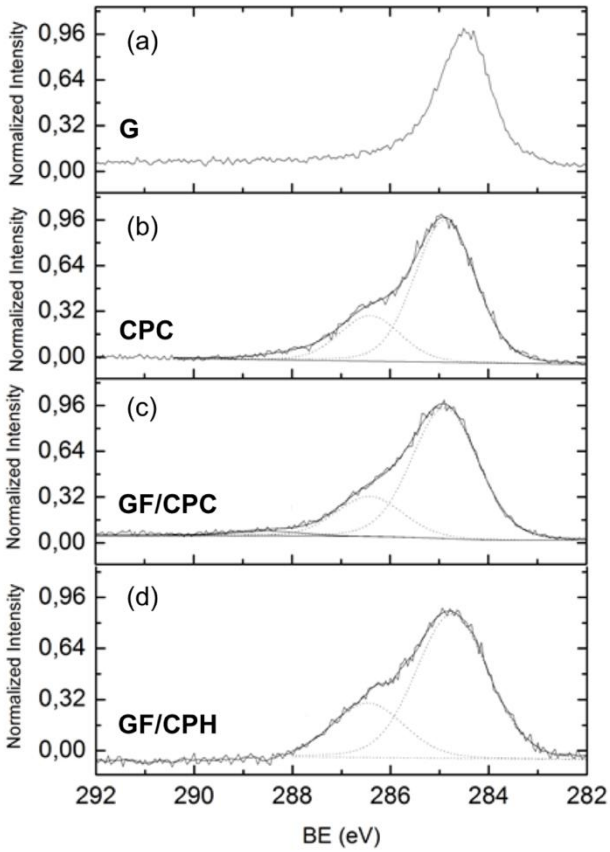

Figure 2.17. C1s XPS spectra of **(a)** G **(b)** CPC powder **(c)** GF/CPC and **(d)** GF/CPH

As widely reported in the literature, the N1s XPS represents a sensitive probe of the charge distribution in the porphyrin macrocycle, being strongly affected by their periphery and intermolecular interactions as well [34-37]. In agreement with the literature data related to the free-base porphyrin, the N1s signal consists of a doublet with the two components centered at 400.2 eV and at 398.2 eV, in both GF/CPC and GF/CPH spectra. Such binding energy (BE) values are diagnostically attributed to the presence of the pyrrolic (-NH-) and to the iminic (-N=) species, characteristic of the porphyrin ring [38,39]. Nonetheless, as seen by comparing **Figures 2.16 (c)** and **(d)**, the bandwidths of the pyrrolic and iminic components are notably different in both cases, being the Full Width at Half Maximum (FWHM) ~1.34 eV in the case of GF/CPC and ~1.82 eV in that of GF/CPH. Such dissimilarity is attributed to a diverse chemical surrounding experienced by the nitrogen atoms of the macrocycle in the two porphyrin-based compounds. In particular, the enlargement of the bands observed in the case of GF/CPH can be caused by the intermolecular stacking occurring between the porphyrin unit along the chains. On the other hand, in the case of GF/CPC, such intermolecular interaction was limited by the long organic sequences of aromatic/aliphatic spacers that separate the porphyrin units in the CPC. The C1s XPS region, was detected for G, CPC powder, GF/CPC and GF/CPH [see **Figure 2.17 (a-d)**]. In the case of the G substrate, the C1s signal consists of a narrow band (FWHM of 1.2 eV) centered at 284.7 eV. The C1s XPS spectrum obtained from the powder of the CPC [**Figure 2.17 (b)**] revealed the presence of two components positioned at 285.0 eV and at 286.5 eV, both with FWHM of 1.5 eV. Such bands are due, respectively, to the C-C, C=C, C-H and to the C-O, C=N, C-N species of the porphyrin structure [38]. The spectra related to the two GF composites [**Figures 2.17 (c) and (d)**] were very similar to that of the powder. Nevertheless, a slight enlargement of the FWHM was observed after the surface functionalization (1.7 eV vs 1.5 eV), as an effect of the interaction of the molecule with the surface [32, 33]. These observations are confirmed by the XPS analyses carried out on the powders of CPH and CPC, taken as references (see **Figures 2.18**).

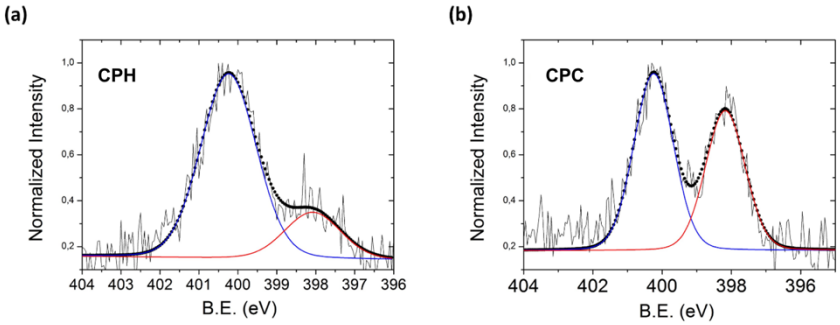

Figure 2.18. N1s XPS spectra carried out on the powders of (a) CPH and (b) CPC

The analyses, in fact, further demonstrated the spectral differences between the two porphyrin-based structures, showing the broadening of the N1s XPS bands for homopolymer, compared with the copolymer. Based on these results, the organic chains used as linker to join the porphyrinic units can modulate the intermolecular π-π stacking of the aromatic rings and, consequently, the final electronic structures of the macromolecular system.
SEM analysis of GF/CPH and GF/CPC were also carried out to observe the morphology of polymeric coating onto the GF surface. In **Figure 2.19,** the different abilities in covering the nickel-graphene foam for the CPH [**Figures 2.19 (a)-(c)**] and the CPC films [**Figures 2.19 (d)-(f)**] were reported and compared.

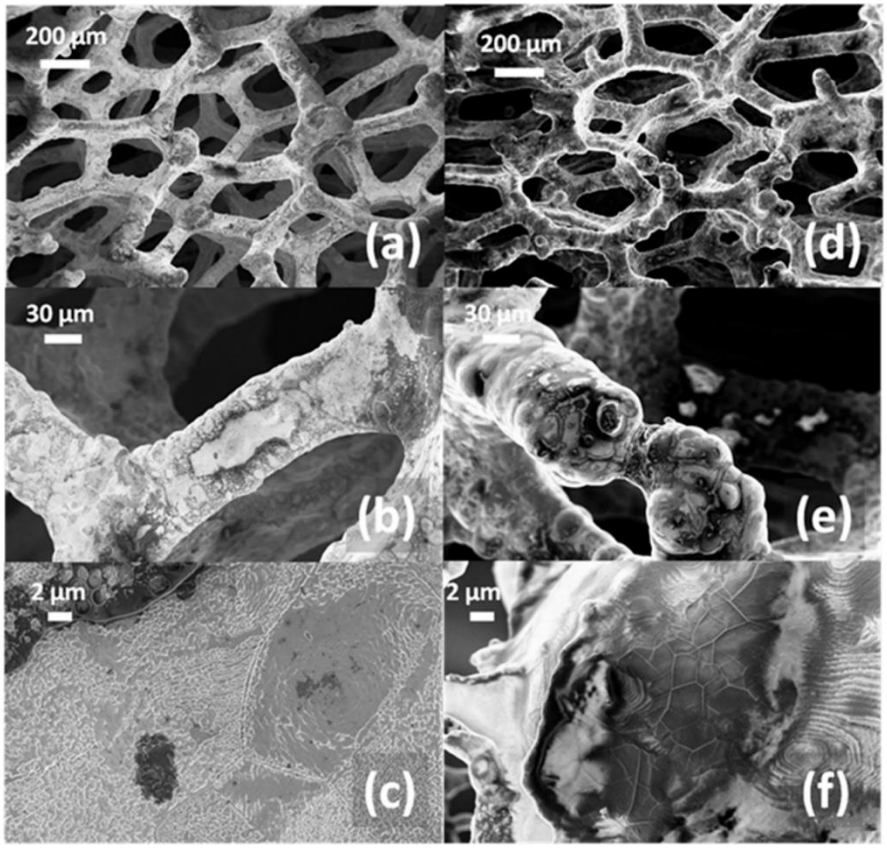

Figure 2.19. SEM images obtained in the Inlens mode at different magnifications of: the as-grown nickel-graphene structure covered with the hopolymer (a)-(c) and with the copolymer films (d)-(f).

In both cases, the polymers coated the total surface of the foam [**Figures 2.19 (a)-(b)** and **(d)-(e)**]. However, their morphology showed clear differences, appearing quite smooth in the copolymer case [**Figure 2.19 (f)**], while it results much rough in the CPH [**Figure 2.19 (c)**]. The morphologies of the two devices can be attributed to the different microstructure as well as Mw (see **Table 1**) of the two types of macromolecules involved. Higher Mw values, together with the presence of 1,20-di(biphenoxide-A) eicosane moieties along the chains, could provide a better coating due to the higher copolymer viscosity. In this regard, in **Figure 2.19 (e)** it is possible to appreciate

that two separate parts of GF remained linked by polymeric copolymer film formed after solvent evaporation. The experimental data reported above indicated the presence of an intimate contact at the G-polymer interface. This evidence suggested the existence of non-covalent interactions among porphyrin polymers and GF, able to accomplish the charge transfer process between the photoactive polymer and graphene substrate. At the same time, a uniform coating of polymer material was obtained, helping to protect the graphene surface from the direct exposure of light and $OH^{\bullet}$ radicals.
To finely explore the morphologies and appreciate the roughness parameters of porphyrins and cyclic-porphyrin polymers onto the graphene surface, we performed AFM analysis onto 2D reference nickel/graphene substrates. These samples were prepared following the same procedure used for 3D GF composites. Lower magnification topographic AFM images (**Figure 2.20**) evidenced a well distributed and extended coating for CPH and CPC films, if compared to porphyrin monomers.

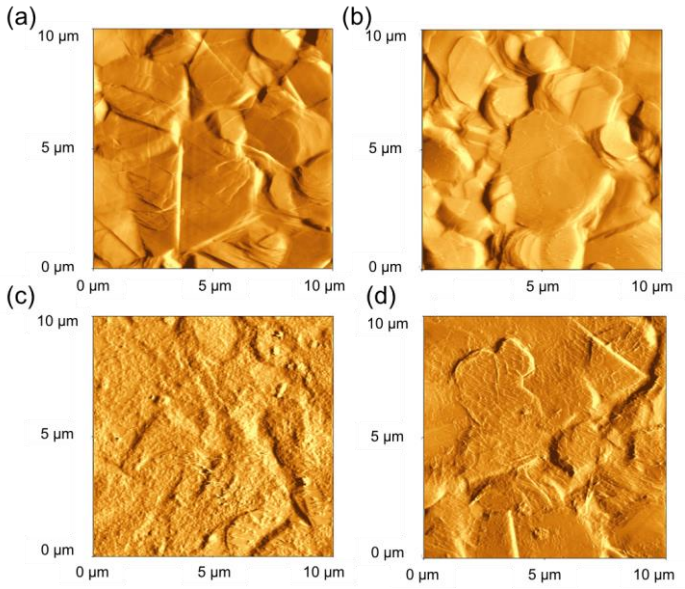

Figure 2.20. Topographic AFM image at lower magnification of (a) GF, (b) GF/monomer, (c) GF/CPH and (d) GF/CPC.

Nevertheless, higher magnification AFM analyses of the three samples demonstrated relevant morphological differences. In **Figure 2.21** the AFM images at higher magnification collected for (**a**) pristine G surface, (**b**) G/porphyrin monomer, (**c**) G/CPH and (**d**) G/CPC were reported. As it is possible to notice from **Figure 2.21 (b)**, porphyrin monomers formed on the exposed surface round shape nano-aggregates as well as nano-tubular structures. The statistics on morphological parameters for this sample revealed a peak-to-peak (i.e. the highest probed height difference by the AFM tip) of 2 nm and a value of RMS of 2.3 nm (all rough surfaces exhibit perpendicular height fluctuations which are characterized by a Root Mean Square, RMS, quantifying the surface roughness). As the width of porphyrin units are estimated to be about 2 nm, we might suppose that they are tilted up perpendicularly to the surface forming non-photoactive H-nanoaggregates types. The round shaped nano-domains whose molecules, without specific form, possess a peak-to-peak of 19 nm. The G/CPH and G/CPC AFM images [**Figures 2.21 (c)** and **(d)**, respectively] showed a better coverage of the underlying graphene and non-columnar structures were presented. Nonetheless, more nano-globular structures appear, with a peak to peak of 20-30 nm and a RMS of 9.2 nm for the CPH, whereas 69 nm with a RMS of 4.7 nm were registered for the CPC. This difference can be attributed to the bigger sizes of macromolecules in the CPC materials than in CPH [see GPC data in **Table 2.1**]. Moreover, the nanoaggregates on the surface of CPH appear very close each other [**Figure 2.21 (c)**], whereas the CPC topography [**Figure 2.21 (d)**] clearly showed a much lower surface density of these nanoglobular shape onto the surface and, hence, a much higher flat surface available for photocatalytic processes. This fact can be attributed to the different cyclic hindered conformational geometries of the CPH and CPC compared to the monomers. In particular, CPC are characterized by longer spacers between porphyrin units that further avoid the π-stacking between them and, as a consequence, strongly reduce the formation of non-active aggregates, as evident in **Figure 2.21 (d)**.

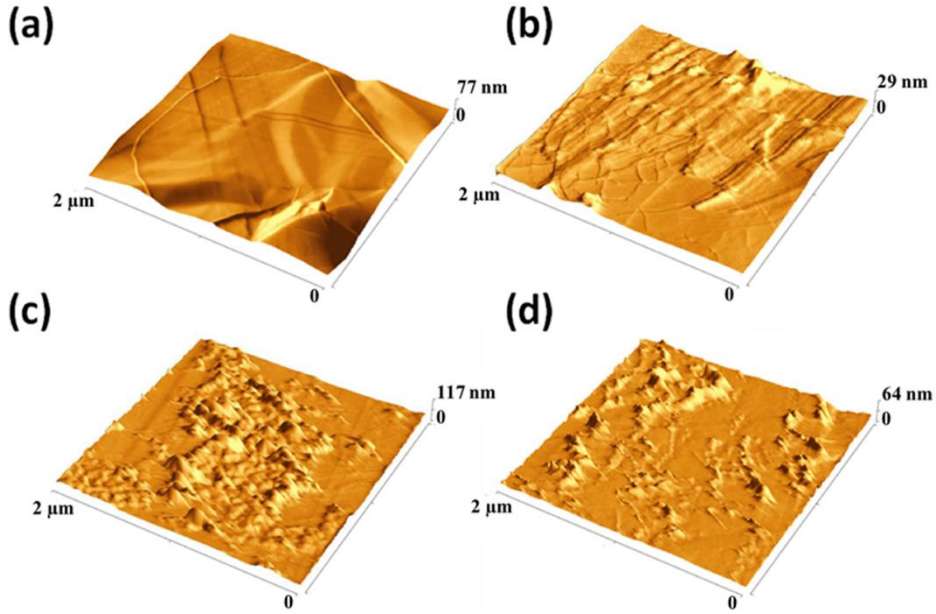

Figure 2.21. Topographic AFM images of (a) G, (b) G/Monomer, (c) G/CPH and (d) G/CPC.

2.4.2 Photocatalytic activity.

The photocatalytic activity under visible-light irradiation of the hybrid materials was evaluated and compared by degrading MB dye water solution. As described in the experimental section, graphene polymer nanocomposites samples were immersed in 2 ml of MB solution 0.015 mM and left overnight in dark to reach the adsorption-desorption equilibrium. In **Figures 2.22 (a)-(b)**, the normalized A/A_0 values (where A and A_0 are the actual and starting MB absorptions, respectively) of MB as a function of the photo-exposure time during both the dark and visible-light experiments are reported.

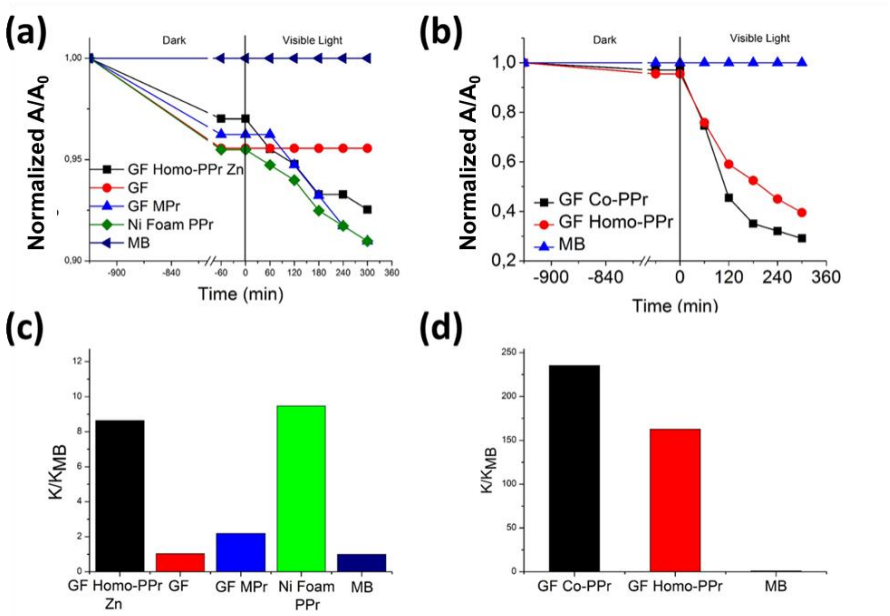

Figure 2.22. Photocatalytic activity of the (a) GF/Zn CPH (black line), GF (purple line), GF/Monomer (blue electric line), Ni Foam/CPH (green line), and (b) GF/CPC (black line) and GF/CPH (red line) compared in both cases to the discoloration of pure MB under visible light irradiation. In Figures (c) and (d) are reported the photocatalytic degradation efficiencies by using MB.

To dispel any doubts on the efficiency of the GF device in promoting photocatalysis, CPH was tested also on pristine Nickel foam surface (without graphene). As shown in **Figure 2.22 (a)**, CPH embedded on Nickel foam (Ni Foam/CPH, green trace) displayed 7% of decrement in A/A_0 values, indicating a very low photocatalytic activity. Similarly, GF with porphyrin monomers, as well as GF/Zn CPH did not give significant catalytic efficiency [**Fig. 2.22 (a)**], whereas a huge increment in degrading MB molecules was evident for the GF surface covered by the two different photoactive polymers [GF/CPH and GF/CPC devices in **Fig. 2.22 (b)**]. It was demonstrated that the porphyrin monomers onto Ni foam did not show a significant activity, likely due to a too fast recombination of the electron-hole pairs formed by irradiation. When

porphyrins were coupled with GF, the contact interface between them (i.e. the potential established across it) prevented charge recombination. The electron transfer process and, as a consequence, photocatalytic activity of graphene/porphyrin composites, could be affected by morphological differences, as evidenced from SEM and AFM analyses of CPH, CPC and porphyrin monomer (**Figs. 2.19** and **2.21**). It is worth to note, indeed, that a typical dewetting phenomenon occurred after bath deposition forming porphyrin aggregates. The length of the spacers between porphyrin units could drive this phenomenon, and as a consequence, changes in coating were observed. Moreover, the different coating of CPH compared to the CPC (**Figure 2.20**) could derive also by their different molecular masses values. As far as the monomer case is concerned, we cannot exclude that its deficiency in photocatalytic activity on graphene surface could arise from an inadequate coverage of the underneath graphene substrate. Concerning the low photocatalytic activity of Zn-CPH, it might be ascribed to the discrete amount of unreacted monomer into the casted solution as well as its low degree of polymerization. According to the Langmuir-Hinshelwood model, we also evaluated the photocatalytic reaction rate, k, given by the following equation: $\ln(C/C_0) = -kt$, where C and C_0 are the actual and starting MB concentrations, and t is the time of exposure [40]. The values of the reaction rate k reported in the ordinate axis are normalized to the k value found in the absence of any catalyst materials (K/K_{MB}). The data calculated for our samples were reported in the **Figures 2.22 (c)-(d)**, remarkably defining the followed order in term of PCE: GF/CPC > GF/CPH >> Ni Foam/CPH> GF/Zn-CPH > GF/Monomer > GF. The higher performance of CPC than CPH could be attributed to the presence of secluded porphyrins along the cyclic chains that better avoided agglomerations. Outstanding, the amount of porphyrin polymers in CPC was about 60% less than CPH. In any case, it was to highlight that only 0,4 mg of polymers supported on 6 mg of GF were able to explicate outstanding photocatalytic efficiencies compared with the recently findings [3,16,41,42]. In addition, the realization of freestanding devices was formulated. As a consequence, further separation steps from water solution, needed in case of dispersed catalyst such as TiO_2, were avoided [16,41,42]. Obviously, different parameters related to the CPC photoability have to be addressed, such as the length and structure of spacer between porphyrin units as well as the MM values and distribution.

Regarding the practical water remediation issue, recyclability is an important property required by photocatalytic devices. Therefore, some recyclability tests were performed. In particular the stabilities of GF/CPH and GF/CPC devices was evaluated performing MB degradation test for three times. After the first cycle, carried out as described in the experimental section, the photocatalysts were removed from water, washed thrice with water, dried for 12 hours and used for the second and the third cycles. The **Figure 2.23 (a)**, concerning GF/CPH, indicates about 60% degradation of MB in the first cycle while it decreases to about 40% and 20% in second and third cycle, respectively. Whereas, from the **Figure 2.23 (b)**, the percentage of MB degradation for GF/CPC decreases from 71% to the 22% from the first to the third cycle. Considering that each run lasts 300 minutes, our systems are able to perform an outstanding photoactive action up to 700 min.
SEM analysis of GF/CPH and GF/CPC [**Figures 2.23 (c)** and **(d)**], carried out after the third run, shows a sensible damage of polymer coating on graphene surface. This phenomenon could be attributed to the ROS which have acted a significant erosion. This indicating that the reduction of photocatalytic action was mainly due to degradation of macromolecules on graphene surface.

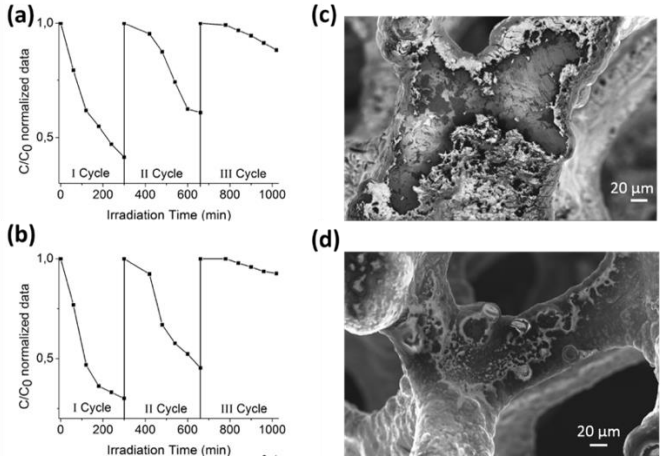

Figure 2.23. Recyclability of (a) GF/CPH and (b) GF/CPC for three subsequent cycles. SEM images obtained in the Inlens mode at 1.00 KX magnification of (c) GF/CPH and (d) GF/CPC after the third cycle.

To test if graphene surface was still able to exploit its co-catalytic properties, we embedded again the GF with the CPC polymers solution, washed with DMF and dried for 12 hours obtaining a restored material for a new recyclability experiment. The same procedure was repeated two times. **Figure 2.24** reports the % of MB degradation for each experiment, evidencing that device performance was kept almost constant in the second experiment with a partial decrease in the third one.

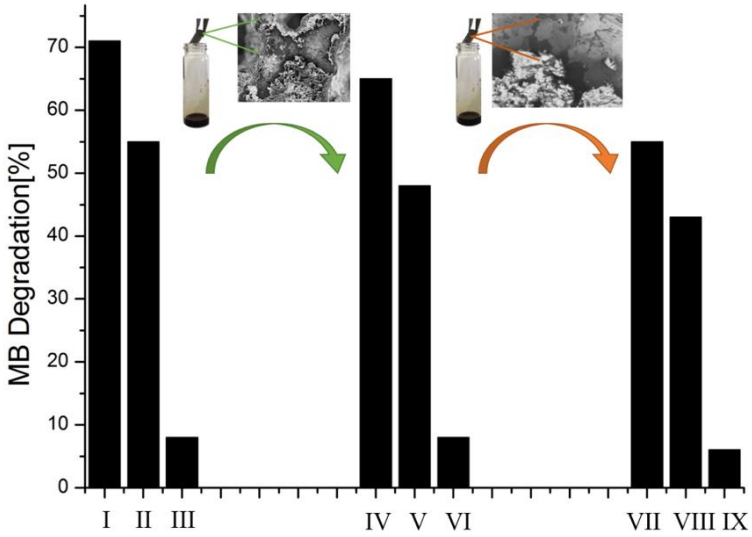

Figure 2.24. Recyclability after re-deposition of CPC on depredated GF/CPC.

2.5 Nickel removal from graphene foam polymer composites

Previously it was well demonstrated as the non-covalent assembly of porphyrin based polymers with a G platform supported by Nickel (Ni), represents an efficient method to avoid the electron-hole recombination mechanism as well as other critical issues deriving from the use of G derivatives, and thus obtaining very effective materials for water purification. However, the Ni content in such kind of materials represents an important limiting factor. Undeniably, Ni removal is strictly required for applications in the water field, being an a contaminant (≥ 0.010ppm) harmful for aquatic and human life. In light of this, in this section a time-saving method to remove Ni from G avoiding the collapse of the 3D structure during the nickel-etching will be presented [43]. In particular, the 3D collapse constitutes an important critical issue for the production of G foam from Ni template by Chemical Vapor Deposition (CVD) [31]. After growing onto the Ni substrate, the production of G foam required a multi-step process which includes polymer infiltration, etching by acidic solution, solvent washing to dissolve the polymer coating and finally, drying or lyophilization. These latter two steps are crucial to obtain a foam-like network graphene, avoiding its structural collapse. As well stated, the etching procedure to eliminate nickel catalyst substrate requires the graphene protection by spin-coating polymers such as commercial poly-methylmetacrilate (PMMA) or polydimethyl siloxane (PDMS) [44]. Subsequently, the sample is etched using HCl 3M, then, it is dried and passed in hot-solvent to remove the polymer, obtaining the final product to employ. However, this step results to be critical inducing the 3D structure collapse caused by the liquid capillary force involved during solvent evaporation, that provides a thinner G than the pristine Ni-Foam [45]. Thus, polymer removal drastically limits the use of Ni-free/G as freestanding materials. In recent papers, concerning the formulation of conducting G foam devices, the collapse of the 3D structure was avoided by non-removing the protective polymer coating that remains as a part of the final material [38,44]. Taking into account this strategy, the novelty here reported consists in preparing the Ni-free sample in a one-step process preserving via photocatalyst coating, the G support [see **Figure 2.25 (a)-(d)**]. In particular, CPC which resulted as the most promising photoactive polymer, was used with the double function of the photoactive part of the device and protective coverage, as well. Thus, the hybrid system was etched. This treatment avoided

the collapse of the network obtaining the final photoactive material without any additional steps. The as-prepared Nickel free sample, was subjected to morphological and physico-chemical characterizations reported as follows.

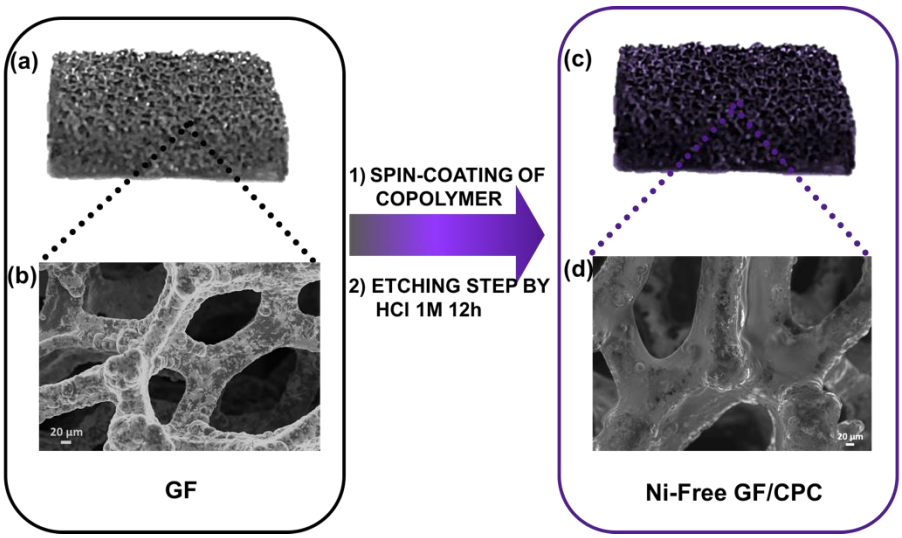

Figure 2.25. (a), (b) an as-grown 3DG coated with a thin layer of Porph rings by a spin-coating deposition method and **(c), (d)** a Ni free GF/CPC sample after etching by hot HCl 1M solution maintaining the typical 3D graphene structure.

2.5.1 Ni-free composite characterization.

To demonstrate that the etching procedure did not affect the 3D structure of GF, SEM images of pristine Ni-foam [see **Figure 2.26 (a)**], as-deposited graphene [**Figure 2.2.6 (b)]** and GF/CPC [**Figure 2.26 (c)**] samples were compared with the Ni-free sample [**Figure 2.26 (d)]**. **Figure 2(d)** showed that the morphology of the Ni-Free GF/CPC sample appears unchanged after the etching procedure demonstrating the efficacy of the polymer-layer onto the graphene surface to protect the G network from collapse of the structure.

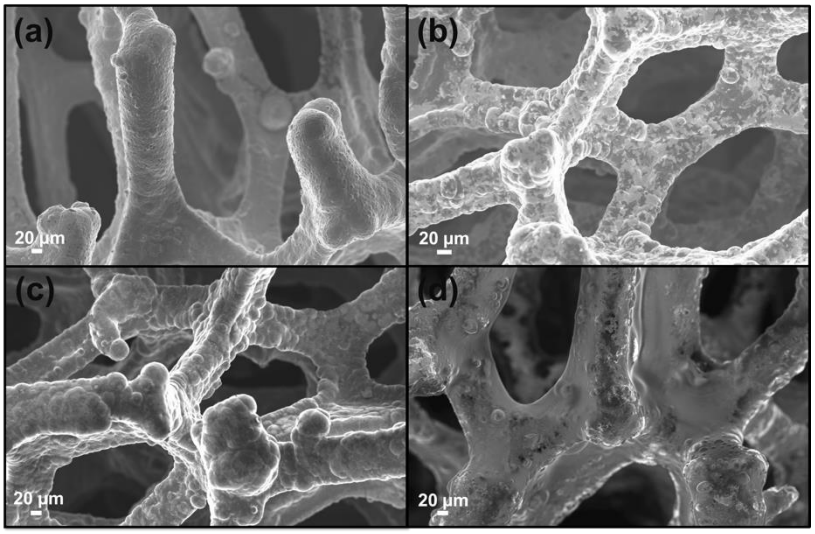

Figure 2.26 SEM images obtained in the Inlens mode of **(a)** Ni-foam **(b)** GF **(c)** GF/CPC **(d)** Ni-free GF/CPC

To ascertain that the etching procedure did not affect the nature of the polymer coating and its related interactions with the G substrate, XPS analysis was performed. Furthermore, XPS provided also information about the effective removal of Nickel. **Figure 2.27 (a)** reported the XPS N1s region of the Ni-free GF/CPC sample. The signal consists of two components centered at 400.2 eV and at 398.2 eV, indicating the presence of the pyrrolic (−NH−) and to the iminic (−N=) species of the CPC respectively [39,44]. Furthermore, the C1s region [**Figure 2.27 (b)**] revealed two components positioned at 285.0 eV (FWHM of 1.5 eV) and at 286.5 eV (FWHM of 1.7 eV), due respectively to the C-C, C=C, C-H of the G and to the C-O, C=N, C-N species of the GF/CDC structure.

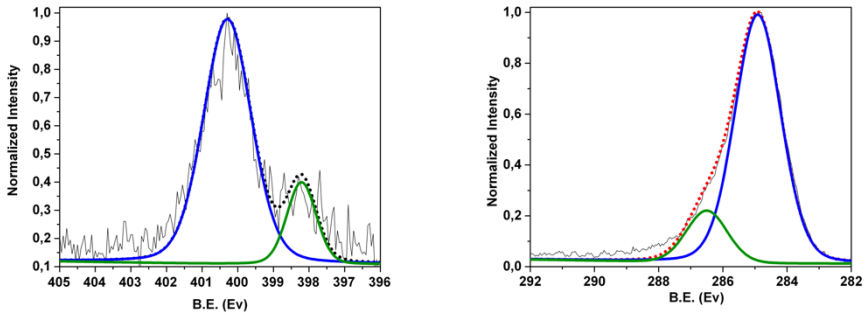

Figure 2.27. XPS spectra of Ni-free/GF-CPC sample in the **(a)** high resolution N1s region and **(b)** high resolution C1s region.

To confirm the Nickel removal after etching, we also performed a quantitative analysis by using Inductively Coupled Plasma-Mass Spectrometry (ICP-MS). In **Table 2.3** the Nickel contents are reported before and after sample etching. As it is possible to observe, the residual Ni amount after the etching procedure, was lower than 100 μg/cm^2.

GF	GF/CDC	Ni-free GF/CPC
165,736 mg/cm^2	166,066 mg/cm^2	94 μg/cm^2

Table 2.3. Nickel content in G samples before and after etching.

2.5.2 Photoluminescence quenching experiments.

The charge electron-transfer processes in hybrid systems were evaluated by analyzing the influence of the G presence on the optical emission of the polyporphyrins [6]. Since photoluminesce (PL) emission strongly depends on the radiative recombination rate of excited electron-hole pairs, additional electron pathways occured it decreases.

As reported in the literature, the coupling of photoactive systems with graphene-based materials produced a quenching in the PL intensity induced by additional electron-transfer process due to the G interaction at material interfaces [15]. **Figure 2.28** compares the PL emission collected under excitation at 325 nm on GF/CDC and on Ni-free

GF/CPC with a reference CPC on pristine Ni-foam (Ni-Foam/CPC). In all cases the PL emission exhibited a broad band composed by two peaks centered at 660 and 720 nm, related to their $Q_X(0–0)$ and $Q_X(0–1)$ transitions respectively.

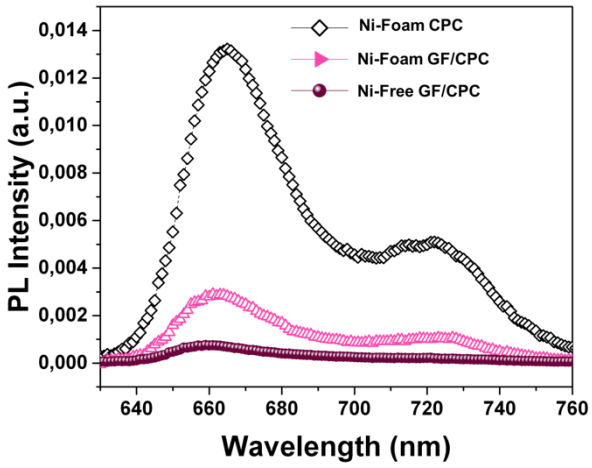

Figure 2.28. PL spectra of Ni-Foam CPC (black rumble), Ni-Foam CPC (fuchsia triangle), Ni-free GF/CPC (purple circle) collected upon excitation at 325 nm.

However, it was evident an effective quenching in the case of Ni-foam GF/CPC and a quasi-total disappearance of characteristic emission band for the Ni-Free GF/CPC with a slightly blue-shift of the signals. This key result validates that π-π interactions between porphyrin aromatic moieties and graphene took place, allowing a remarkable electron transfer at the polymer interface [6]. Different phenomena could justify the further PL quenching after nickel removal, such as the change in graphene electronic structure as well as an enhanced graphene π-delocalization after electron injection [46-48].

2.5.3 MB degradation test of Ni-Free GF/CPC composite

The photocatalytic activity versus MB (**Figure 2.29**) is tested by comparing the results with those reported in the previous sections. The dark adsorption data of all the samples are reported in **Figure 2.29 (a)**

evidencing a major adsorption in the case of the Ni-free material. This value was most likely due to hollow channels of G, formed after Ni removal and exposed to the MB solution. When the adsorption/desorption equilibrium was reached, samples were exposed to the visible light.

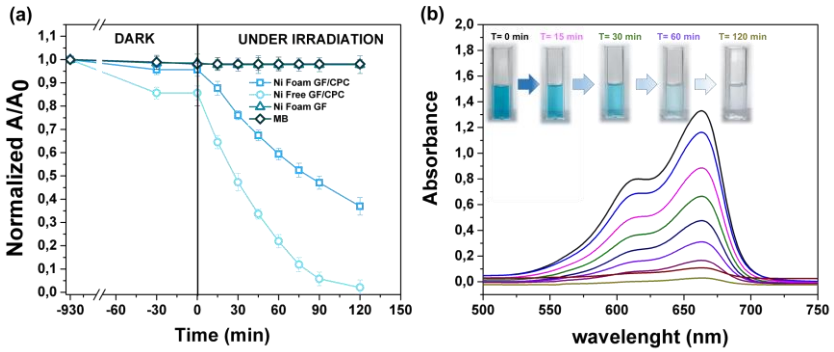

Figure 2.29. (a) Photocatalytic activity of GF, GF/CPC, Ni-Free GF/CPC toward the degradation of MB after 120 minutes of light irradiation; **(b)** Time dependent absorption changes of MB upon visible irradiation in presence of Ni-free GF/CPC.

Data collected after 120 minutes of light irradiation revealed that Ni-free GF/CPC degraded 93.4% of MB [see also **Figure 2.29 (b)**], whereas the Ni-foam GF/CPC showed 60% of photo-degradative capacity. As expected, also the Ni Foam GF, used as external reference did not exhibit MB degradation. These results indicated that the Ni-removal played a key-role in the photodegradation, eliminating almost all MB after only 120 minutes of VL irradiation. According with PL measurements, the boost of the photocatalytic efficiency was reasonable owed to a more effective electron-transfer process at the graphene interface. Also in this case, compared with the performance of similar devices [8,10], this hybrid sample offered the great advantage to use a standalone system [10], cointaining only 0,4 mg/cm^2 of photocatalyst, [8,49] showing valuable photoability under visible-light irradiation.

2.5.4 Photocatalytic degradation of emerging pollutants.

The photocatalytic activity of Ni-free GF/CPC hybrid material was monitored by UV-Vis, total organic carbon (TOC) and Mass Spectrometry (MS) techniques selecting as target pollutants the pesticide 2,4-dichlorophenoxyacetic acid (2,4-D), MB dye, and the water soluble polyethylene-glycol (PEG). The 2,4-D herbicide is widely used in agricultural sector although it is well renewed its toxicity accomplished by a poorly water biodegradability [18]. Concerning the PEGs, controversial opinions was reported on its safe environmentally use. This hydrophilic polymer, which is often included in several copolymeric formulations for a wide range of applications, is considered biodegradable up to 10 monomeric units. However PEG with higher molar masses are commonly used for cosmetics, detergents and biomedical purposes, becoming an insidious threat for the environments [50-53]. In **Figure 2.30 (a-b)** are reported the ESI-MS spectra of **(a)** 2,4-D pristine solution and **(b)** after 6 hours of visible-light irradiation in presence of the photocatalyst. As shown from the spectra, the ESI-MS peaks associated to the 2,4-D molecules (*m*/*z* at 218.95/ 220.95), disappeared after the photocatalytic procedure. Conversely, the lesser abundant signals at *m*/*z* 160.95/162.94 assigned to the main degradation product 2,4-dichlorophenol [18], significantly increased after the photocatalyst addition. The initial presence of 2,4-dichlorophenol molecules in the pristine sample derived from synthesis impurity. Although the formation of by-products indicated the occurrence of herbicide degradation, 2,4-D mineralization was not successfully achieved under these experimental conditions. Indeed, as revealed from UV-Vis and TOC analyses, absorbance profiles as well as TOC values remained unchanged during the photo-exposure, most likely due to the formation of recalcitrant 2,4-dichlorophenol and other chlorinated species in solution. As expected, this intermediates are very difficult to mineralize by Vis-light photocatalytic process [54,55] requiring more severe experimental conditions.

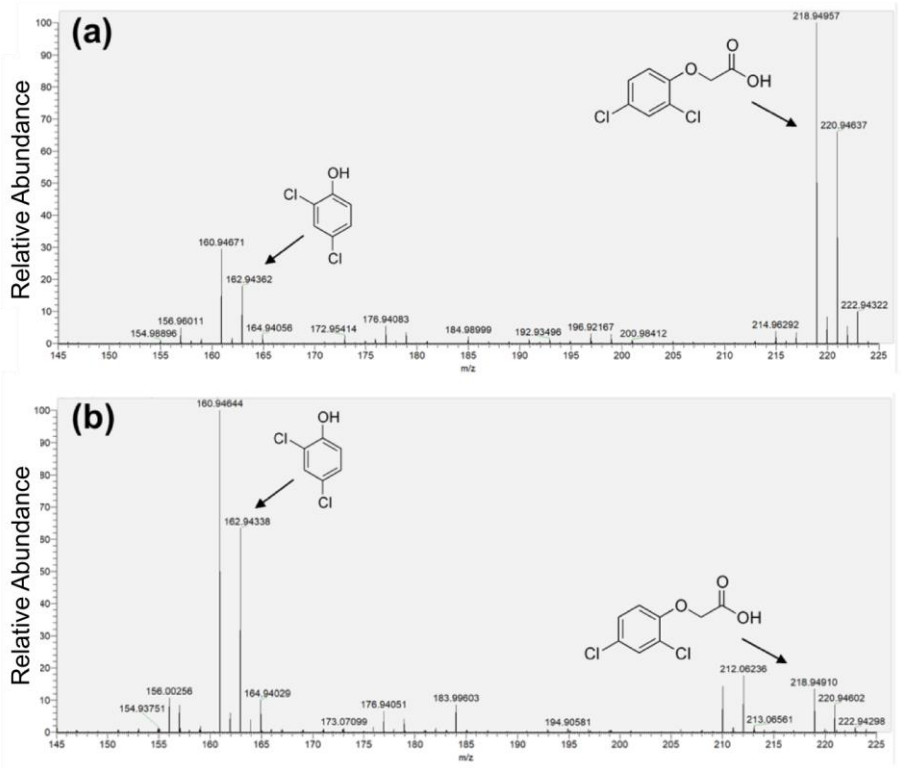

Figure 2.30. ESI-MS spectra collected in negative ion mode for: **(a)** untreated 2,4 D solution and **(b)** Visible-light photo-exposed 2,4-D solution after 6 hours of irradiation time.

Photodegradation ability of hybrid material was tested also on PEG solution. Among water soluble polymers, PEG is constituted by a simple molecular structure representing an adequate compound for studying photocatalytic degradation features. To this purpose, a sample having a narrow polydispersity (D= 1,09) with an Mw of 1900 Da was selected to allow the simultaneously determination of Molar Masses and degradation products as well, by MALDI methods during photoexposure. **Figure 2.31 (a-c)** reported MALDI TOF spectra collected in reflectron mode of **(a)** pristine PEG sample; after **(b)** 3 hours and, **(c)** 6 hours of photo exposure in presence of the photocatalyst. As it is possible to notice from the figure, relative abundance of signals corresponding to PEG macromolecular chains,

significantly decreased as the exposure time proceeded, producing oxidized polymer chains at lower mass range. Degradation products deriving from photocatalytic process are assigned to PEG oligomers having formic acid, aldehydic and alcoholic end-groups. After 6 hours, progressively degradation took place, leading to the disappearing of initial PEO distribution with formation of much lower macromolecular oxidized chains, that cannot be detected being lower to the mass range inferior limit. Photochemical oxidation mechanism proposed in literature for PEG [51,53,56] well fitted with the products revealed by MALDI, mainly involving the ROS attack on CH_2 groups with a random chain scission pathway. At this stage mineralization measured by TOC revealed the 85% of PEG removal **(Figure 2.32).**

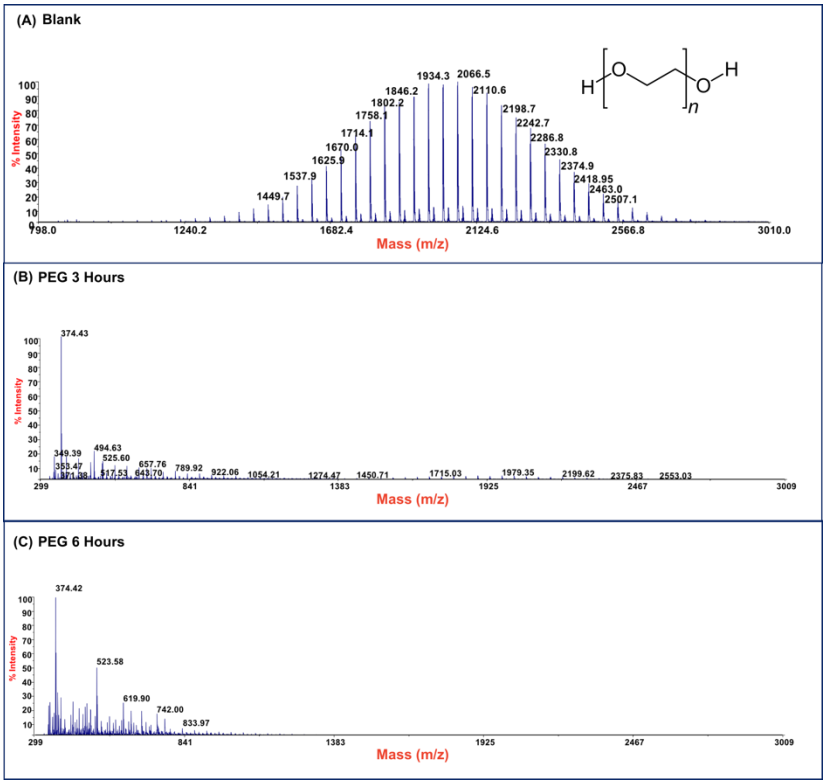

Figure 2.31. MALDI-TOF spectra of **(a)** pristine PEG sample and after **(b)** 3 hours and **(c)** 6 hours of photo-exposure

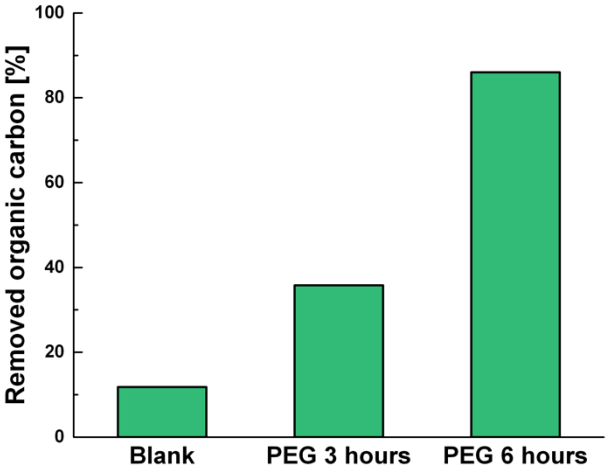

Figure 2.32. TOC measurements of pristine PEG irradiated for 6 hours (Blank) and PEG treated with Ni-free/G-Porph rings after 3 hours (PEG 3 hours) and 6 hours (PEG 3 hours) of photoexposure.

2.5.5 Reactive oxygen species determination and proposed degradation mechanism.

The photochemistry of the material was investigated by the qualitative evaluation of the ROS produced, by following methods described in ref. 7, 52 and 53. Generally, when a photocatalyst is irradiated by light, ROS such as hydroxyl radical ($OH^{\cdot}$), superoxide radicals ($O_2^{\cdot -}$) and the singlet oxygen ($^1O_2$) are generated [10]. These reactive species are able to degrade the pollutants by red-ox reactions [2]. Compared with inorganic photo-catalysts, the formation of $^1O_2$ is a distinctive feature of photosensitizers. The singlet oxygen is a selective oxidant specie able to promptly react with unsaturated double bonds, phenols, sulfides, amines and other electron-donor compounds [57]. In addition, it explicates a highly cytotoxic action versus cells and microorganisms becoming particularly attractive in wastewater treatment for its dual function of decontamination and disinfection [58]. The discrimination among the produced ROS can be obtained by introducing specific

radical-trapping agents during the light exposure. These scavenger molecules interacting with the related photo-generated radicals, inhibit their reaction with the organic pollutant. In particular, ethylene diamine tetraacetic acid (EDTA), t-BuOH, nitro-blue tetrazolium (NBT) and 9,10-anthracene-diyl-bis(methylene)dimalonic acid (ABDA), can be efficiently used to scavenge photo-generated holes, hydroxyl radical, superoxide radical and singlet oxygen respectively [57,59,60]. Consequently, the photochemistry mechanisms involved during photoexcitation can be better elucidated. In particular, samples of 1 cm^2 of Ni-free photocatalyst were immersed in MB solutions up to the adsorption-desorption equilibrium. Then, increasing volumes of trapping agents from 1 mg/L up to 10 and 15 mg/L were added to the solutions evaluating their inhibitory effect on MB degradation (**Figure 2.33**). **Figure 2.33** displayed the degradation tests collected by adding 15 ppm of trapping agents together with the MB degradation trace of our sample and compared. As it is possible to observe from the **Figure 2.34**, the addition of t-BuOH did not affect MB photo-degradation trend. On the contrary, when EDTA was added to the solution, the MB experienced only a decrement of 52% denoting as photo-generated holes took part to the process. Similarly, the presence of NBT and ABDA seems to determine inhibition of MB degradation. As well known, their scavenger effects can be referred to the presence of superoxide radical and singlet oxygen respectively. These findings are entirely in agreement with recent literature reporting similar systems, proposing also an increase of singlet oxygen quantum yield induced by graphene-porphyrin π-π interactions [10].

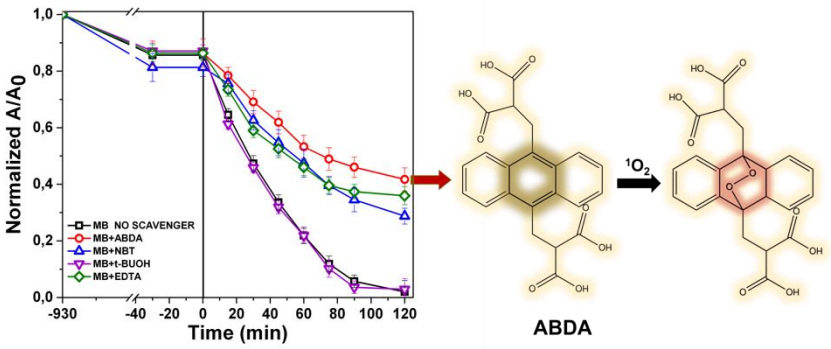

Figure 2.33. Effect of ABDA, NBT, EDTA and t-BuOH radical-hole scavengers on the degradation rate of MB by using the Ni-free/G-Porph rings sample. The inhibition of the MB degradation due to the ABDA oxidation indicates the effective ROS production during 120 minutes of irradiation time. Among the produced ROS, $^1O_2$ constitutes the predominant species.

To gain a better insight into the photodegradation mechanisms, it was very important to understand the electronic properties of the Porph rings (i.e. HOMO and LUMO levels). Although the Cyclic Voltammetry (CV) represents an appropriate tool to estimate the frontier orbitals, it often requires the combination with other techniques, such as UV-Vis spectroscopy [61,62]. CV curves were referred to ferrocene by taking $E_{1/2}(Fc/Fc^+)$ = 0.429 V *vs* SCE (**Figure S3**). From the inspection of the CV measurements on the Porph rings reported in **Figure 5**, the small oxidation and reduction peaks at ~1.6 and ~0.4 V vs Fc/Fc^+ are attributed to traces of the residue monomer molecules, as demonstrated by the CV curve of the porphyrin monomer solution (**Figure S5**). The presence of residue porphyrin monomer was also confirmed by the MALDI spectra (**Figure S1**). Thus, the high and irreversible reduction peak at -0.6 ± 0.2 V vs Fc/Fc^+ was ascribed to the Porph rings (half of FWHM was used to evaluate the error). HOMO (E_{HOMO}) and LUMO (E_{LUMO}) energy levels can be estimated from oxidation (E_{ox}) and reduction (E_{red}) peaks potential as follows:

$$E_{HOMO} = -(E_{ox.} \text{ vs } Fc/Fc^{+} + 4.8)\ eV \quad \textbf{(1)}$$

$$E_{LUMO} = -(E_{red.} \text{ vs } Fc/Fc^{+} + 4.8)\ eV \quad \textbf{(2)}$$

where 4.8 eV is the formal potential of the Fc/Fc^{+} redox couple in the Fermi scale [62]. CV curves were referenced to ferrocene by taking $E_{1/2}(Fc/Fc^{+})$ = 0.429V *vs* SCE (**Figure S5**). According to equation **(2)**, the LUMO energy level of the Porph rings was estimated to E_{LUMO}= -4.2 ± 0.2 eV. On the other hand, by UV-Vis absorption measurement (**Figure S6**) of the optical bandgap (E_g) as E_g= 2.2 eV were performed, estimating also for the first time the HOMO energy level as E_{HOMO}= E_{LUMO} -E_g, finding the equation **(1)** E_{HOMO} = -6.4 ± 0.2 eV [56,63,64].

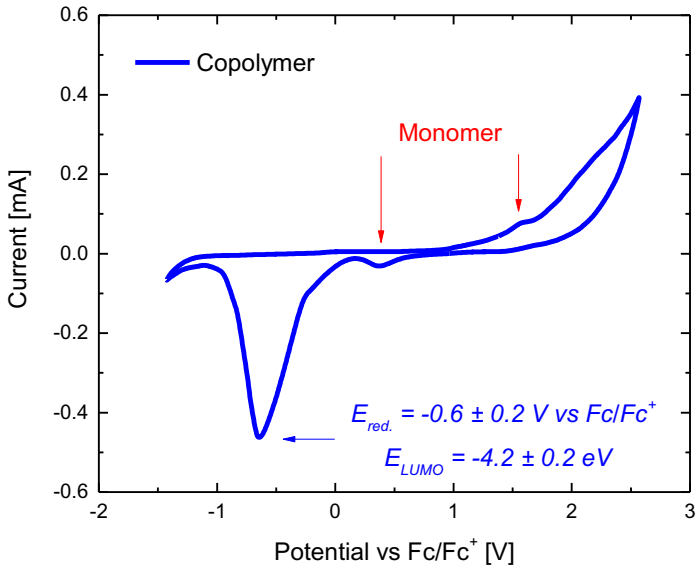

Figure 5. Cyclic voltammetry of Porph rings recorded at 25 mV s^{-1} scan rate in 0.1 M TBAPF6 in dichloromethane solution. Ferrocene was used as internal standard.

On the basis of these experimental data, degradation mechanisms of

the Ni-free GF/CPC were proposed and summarized in **Figure 2.34.** The work function (E) of graphene versus vacuum can be calculated to be about 4.42 eV [53]. Considering the previous reported electrochemical measurements, the LUMO (-4.2 eV) and HOMO (-6.64 eV) energy levels of CPC samples were assigned and plotted. Based on these data, the light-excited porphyrin electrons can be excited from its S0 to the S1* LUMO level. Here, the excited state S_1^* can involve ISC resulting in a first excited tripled state S_3^* as shown in equation (2.1). Supported by literature, this process is also facilitated by the presence of graphene, which can prevent the S_3^* physical deactivation [62] and the electron-hole recombination between S_1^* and the porphyrin ground state [10,57]. Since S_3^* has a longer lifetime than S_1^*, it can transfer its energy to another molecule. In the presence of oxygen, S_3^* transfers its energy to the oxygen triplet ground state, producing singlet oxygen (equation 2.2).

$$P(S_1{}^*) \rightarrow P(S_3{}^*) \tag{2.1}$$

$$P(S_3{}^*) + {}^3O_2 \rightarrow P(S_0) + {}^1O_2 \tag{2.2}$$

At the same time, S3* can transfer electrons to oxygen (equation 2.3) as well as graphene, generating superoxide radicals ($O_2^{\bullet -}$), in accordance with our radical-trapping experiments.

$$P(S_3{}^*) + O_2 \rightarrow P^+ + O_2^{\bullet -} \tag{2.3}$$

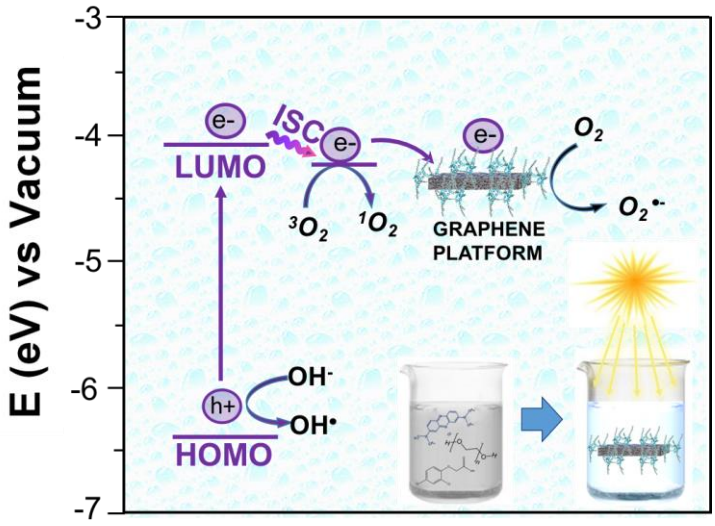

Figure 2.34. Energy diagram of the proposed mechanism for the photocatalytic degradation of MB by using Ni-free GF/CPC as organic photosensitizer.

2.6 Work in progress

The previously described hybrid materials showed outstanding performances to degrade pollutants in water. However, freestanding photoactive graphene-based nanocomposites has not been deeply studied yet and very few examples exist concerning their applications in the water purification field. As a consequence, new promising hybrid nanomaterials based on porphyrin-polymers with different architectures (including open chains, block copolymers, hyperbranched, star, brush) could be designed and developed, comparing their photocatalytic performances with the previous ones. In this context, Reversible Addition-Fragmentation chain Transfer polymerization (RAFT) seem to be the most appropriate technique to obtain an excellent control in the polymer architecture, while also providing tunable structures with narrow molecular-weight distributions (MwDs).

2.6.1 Reversible Addition Fragmentation chain Transfer (RAFT) polymers

Since 1998, date of the first report about RAFT polymerization, a lot of attention is focused on its use for the synthesis of specific polymeric molecular architectures [65,66]. In particular, RAFT is a peculiar living radical polymerization (RDRP) [67], also known as controlled radical polymerization by which it is possible the synthesis of polymeric architectures characterized by predictable molecular masses value, low molar mass dispersity (Đ), high end-group fidelity, and capacity for continued chain growth. Today, with more than 8000 publications RAFT process is considered the most promising tool to generate materials with a broad range of applications from materials science to medicine [68-71]

2.6.2 The RAFT process

The RAFT process is based on an equilibrium between active and dormant chains, established by a degenerative transfer process. Particularly, the number of radicals during the activation−deactivation process remain constant and, as a consequence, a source of radicals is required, usually a radical initiator. In **Figure 2.35** the proposed RAFT mechanism is reported. Specifically, in the first step (I) a radical initiator is activated and, the propagating radical species ($Pn^{\cdot}$) are added to the RAFT agent (III), also called chain transfer agent (CTA). Thus, equilibrium between active and dormant species (steps III and V) is achieved. The latter steps are degenerate as they involve a reversible transfer of the functional chain end-group between the dormant chains (normally a thiocarbonylthio group, Z−C(=S)S−R group) and the propagating radicals (macroRAFT or macroCTA) representing the basis of the RAFT mechanism.

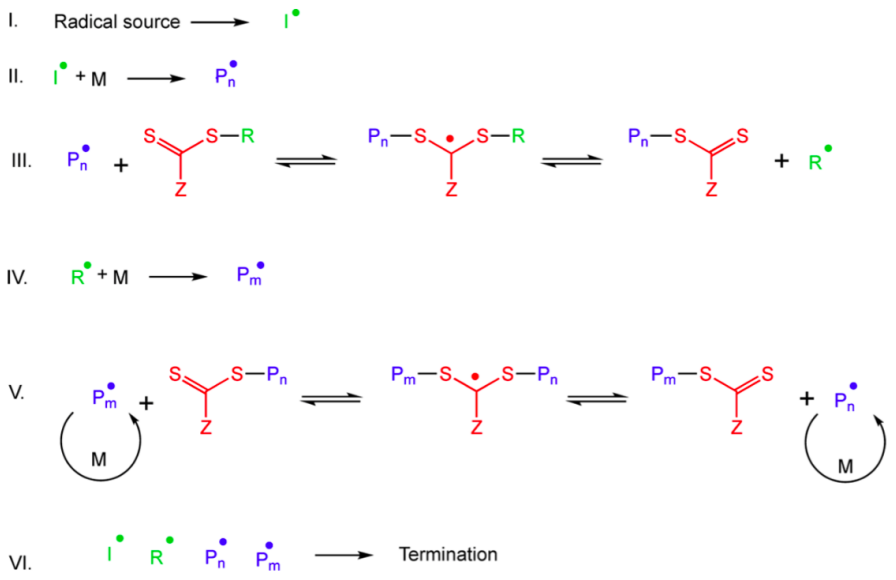

Figure 2.35. Mechanism of Reversible Addiction Fragmentation Transfer process**.**

2.6.3 Porphyrin-based RAFT copolymers

Taking advantage in the use of RAFT polymerization to formulate polymers with precise molecular weight, formulation of linear porphyrin-based RAFT homo-polymers and block copolymers could be done. After deposition on 3D-G materials, their photoability will be compared with those of 3D-G/CPC. Thus, a porphyrin acrylate, 5,10,15-Tri[p-(9-methoxy-triethylenoxy)-phenyl]-20-(p-acryloxyphenyl)-porphyrin [H_2-P(TEG-ME)$_3$Acr] was synthesized. However, being porphyrin-based polymers usually characterized by low transition temperature (Tg) ranging from 15 to 37 °C, depending on MMs value [], its copolymerization by using co-block possessing higher Tg value were designed (see **Scheme 2.2**).

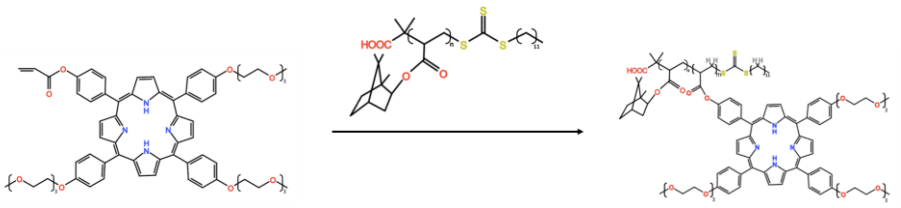

Scheme 2.2 RAFT co-polymerization between [H_2-P(TEG-ME)$_3$Acr] and PiBA previously synthesized by RAFT polymerization.

In particular, poly-isobornyl-acrylate (PiBA) was selected as ideal candidate having high glass transition temperature (Tg = 94 °C), along with its bio-based nature and transparency [72]. Hence, PiBA was synthesized by RAFT polymerization, optimizing the reaction conditions by changing parameters such as the radical initiator content and CTA:RAFT molar ratio. Furthermore, for each experiment, molecular weight distribution, kinetics studies and monomer conversion were evaluated as reported in **Figures 2.36-2.39.** The present work is still in progress in collaboration with prof. Brent Sumerlin at the University of Florida (Gaineville, USA).

IBA/CTA/AIBN [100/1/0.2]

(a)

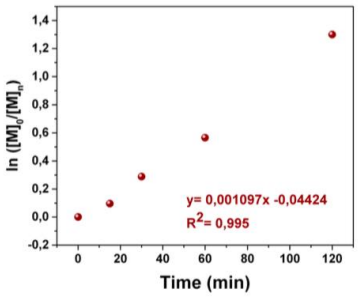

(b)

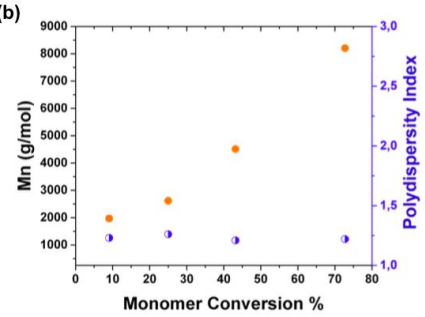

(c)

Time	*Mn$_{THEORY}$	Mn$_{SEC}$	Mw$_{SEC}$	PD
30''	2860	2618	3296	1.26
60''	5564	4512	5470	1.21
120''	9308	6819	8437	1.24
180''	15548	8202	9966	1.22

$$* \frac{g\ IBA}{mol\ RAFT} \times \frac{\%conversion}{100} + PM_{RAFT}$$

(d)

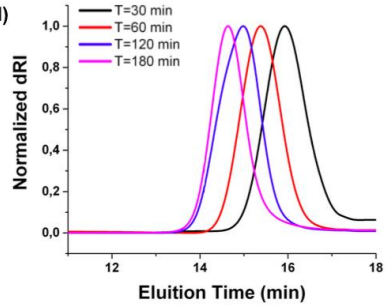

Figure 2.36. Synthesis of PiBA by RAFT polymerization by using iBA/CTA/AIBN molar ratio of 100/1/0.2.

(a) Pseudo-first-order rate plot for iBA polymerization.

(b) Evolution of the monomer to polymer conversion with reaction time.

(c) GPC data of PiBA polymerization as a function of time in comparison with theoretical values.

(d) GPC traces of the withdrawal acquired during the polymerization in fuction of the time.

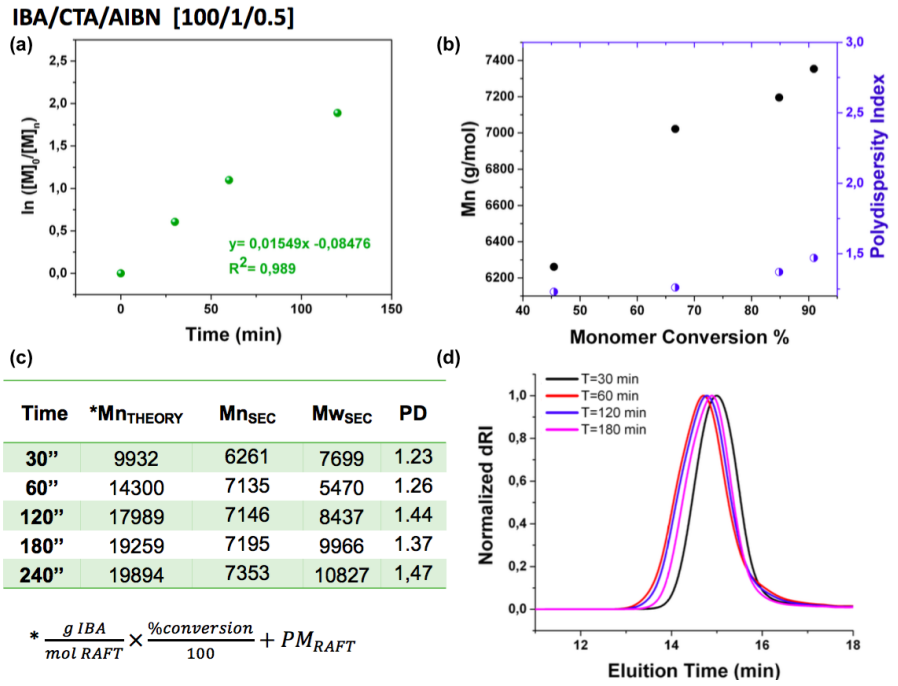

(c)

Time	*Mn_{THEORY}	Mn_{SEC}	Mw_{SEC}	PD
30”	9932	6261	7699	1.23
60”	14300	7135	5470	1.26
120”	17989	7146	8437	1.44
180”	19259	7195	9966	1.37
240”	19894	7353	10827	1,47

$$* \frac{g\ IBA}{mol\ RAFT} \times \frac{\%conversion}{100} + PM_{RAFT}$$

Figure 2.37 Synthesis of PiBA by RAFT polymerization by using iBA/CTA/AIBN molar ratio of 100/1/0.5.

(a) Pseudo-first-order rate plot for iBA polymerization.

(b) Evolution of the monomer to polymer conversion with reaction time.

(c) GPC data of PiBA polymerization as a function of time in comparison with theoretical values.

(d) GPC traces of the withdrawal acquired during the polymerization in fuction of the time.

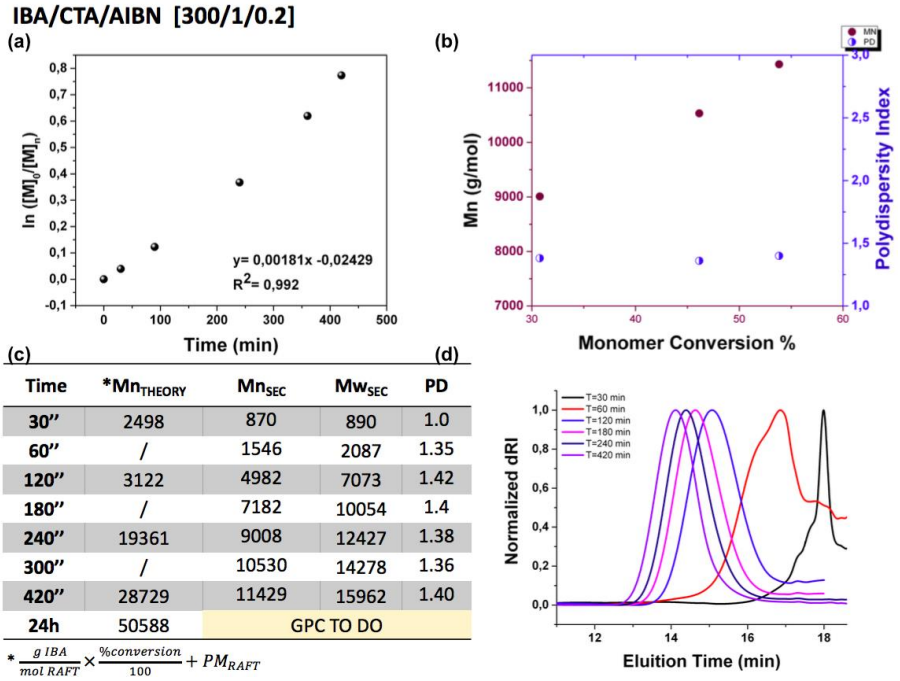

Time	*Mn_{THEORY}	Mn_{SEC}	Mw_{SEC}	PD
30''	2498	870	890	1.0
60''	/	1546	2087	1.35
120''	3122	4982	7073	1.42
180''	/	7182	10054	1.4
240''	19361	9008	12427	1.38
300''	/	10530	14278	1.36
420''	28729	11429	15962	1.40
24h	50588	GPC TO DO		

$$* \frac{g\ IBA}{mol\ RAFT} \times \frac{\%conversion}{100} + PM_{RAFT}$$

Figure 2.38. Synthesis of PiBA by RAFT polymerization by using iBA/CTA/AIBN molar ratio of 300/1/0.2.

(a) Pseudo-first-order rate plot for iBA polymerization.

(b) Evolution of the monomer to polymer conversion with reaction time.

(c) GPC data of PiBA polymerization as a function of time in comparison with theoretical values.

(d) GPC traces of the withdrawal acquired during the polymerization in fuction of the time.

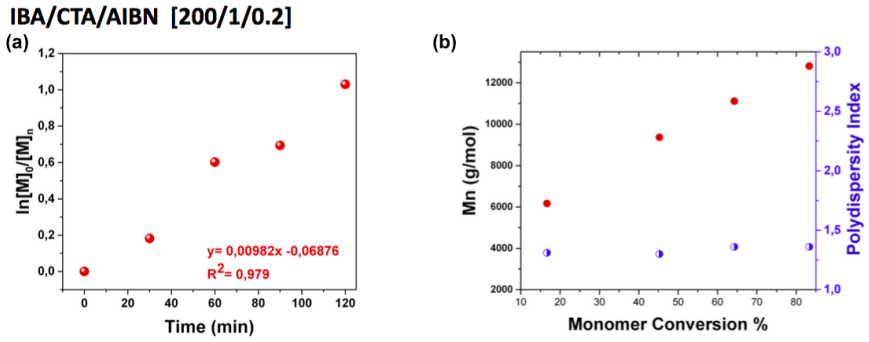

(c)

Time	*Mn_{THEORY}	Mn_{SEC}	Mw_{SEC}	PD
30''	12589	6171	8077	1.28
60''	18883	9362	12262	1.3
120''	26857	11115	15097	1.36
180''	34830	12808	17425	1.36

$$* \frac{g\ IBA}{mol\ RAFT} \times \frac{\%conversion}{100} + PM_{RAFT}$$

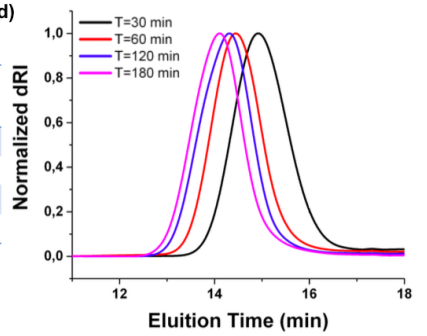

Figure 2.39. Synthesis of PiBA by RAFT polymerization by using iBA/CTA/AIBN molar ratio of 200/1/0.2.

(a) Pseudo-first-order rate plot for iBA polymerization.

(b) Evolution of the monomer to polymer conversion with reaction time.

(c) GPC data of PiBA polymerization as a function of time in comparison with theoretical values.

(d) GPC traces of the withdrawal acquired during the polymerization in fuction of the time.

Materials and methods

Materials. All solvents and basic materials were commercial products appropriately purified before use.

Gel Permeation Chromatography (GPC).
A Waters 515 HPLC pump, connected to four Ultra-Styragel HR columns joined in series (in the order: HR4, HR3, HR2 and HR1), and a Waters R401 diferential refractometer, were used for GPC analysis. Polymer solutions (1mg/ml, in THF) were injected and eluted at a fow rate of 1ml/min. Calibration curve was obtained using a set of primary polymethylmethacrylate (PMMA) standards.

Matrix Assisted Laser Desorption Ionization–Time Of Flight (MALDI-TOF).
MALDI /mass spectra were recorded in refector mode using a 4800 MALDI TOF/TOF™ Analyzer (Applied Biosystem, Framingham, MA, USA), equipped with a Nd:YAG laser (λ=355nm) and working in positive-ion mode. External calibration was performed using an Applied Biosystems calibration mixture consisting of polypeptides with diferent molecular weight values. Mass accuracy was about 50 ppm. Te samples were prepared by mixing approximately 0.1mmol of the monomer or polymer and 40 mmol of trans-3-indoleacrylic acid (IAA, used as a matrix) on the sampler target, using THF as a solvent. Te m/z nominal values reported in the spectra, are referred to molecular ions constituted by the most abundant isotopes of each element present in the molecule.

XPS analysis.
XPS were performed by a PHI ESCA/SAM 5600 Multy technique spectrometer with the use of an Mg standard X-ray source. During the analyses, the pressure in the chamber was ~10^{-9} Torr. The measurements were carried out at 45° photoelectron take-of angle relative to the sample surface with an acceptance angle of ±3°. The analyzer pass energy was set at 23.5 eV for the high-resolution spectra. The binding energy (BE) scale was calibrated by centering the C1s signal of the aliphatic/aromatic component at 285.0 eV). Te analyses were performed on 2mm diameter surface area of the sample, much greater than the lateral size of any carbon island on the nickel foam surface.

Raman spectroscopy.
Micro-Raman Stokes spectra were taken in backscattering geometry with a HORIBA Jobin-Yvon system, equipped with Olympus BX41 microscope. He-Ne laser radiation at a wavelength of 632.8nm is focused to a spot size of about 1 μm by a 100× objective. The laser power on the sample was about 5mW, and a 550mm focal length spectrometer with 1800 lines/mm grating was used.

UV–Vis spectroscopy.
Absorption spectra were registered by using quartz cuvettes with a path length of 1 cm on a Shimadzu spectrophotometer at room temperature. For the experiment, different copolymer solutions (about 1×10^{-6} M) were prepared, by using $CHCl_3$,THF and DMF as solvents.

UV–visible diffuse reflectance spectra (DRS) were recorded on a Varian, CARY 6000i within the wavelength range of 200–1100 nm by using a double-beam spectrophotometer equipped with an integrating sphere. In the used reflectance geometry, both the specular and diffuse components are sent to the detector in the integrating sphere.

SEM and FIB analyses
In order to study the samples morphology and the uniformity of the porphyrin coverage, 2D- and 3D-G hybrid structures were analyzed by scanning electron microscopy (SEM, Gemini 152 feld emission SEM Supra 25, Carl Zeiss, Oberkochen, Germany—images obtained in the Inlens mode). For cross-sectional analyses, 2D hybrid materials were carefully cut. The SEM images were recorded by the electron beam of a Versa 3D Dual Beam Focused Ion Beam (FEI, Hillsboro, OR, USA—images obtained with a secondary electron detector in low-vacuum condition).

Atomic force microscopy (AFM)
AFM analyses were performed using a Bruker-Innova microscope operating in high-amplitude mode, and ultra-sharpened Si tips were used (MSNL-10 from Bruker Instruments, with anisotropic geometry, the radius of curvature∼2 nm, tip height∼2.5 μm, front angle∼15°, back angle∼25°, side angle 22.5°). The Si tips were substituted as soon as a resolution loose was observed during the AFM images acquisition. The AFM images were analyzed by using the SPM LABANALYSES

V7.00 software. In order to give representative parameters, statistics on the AFM images were carried out over different areas of the same sample.

Determination of Total Organic Carbon (TOC)
The mineralization of the pollutants after the irradiation in the presence of samples was evaluated by measuring the TOC content with a TOC analyzer (Shimadzu TOC-LCSH) equipped with a non-dispersive infrared detector.

Inductively coupled plasma–mass spectrometry (ICP-MS).
ICP-MS analysis was performed by using a NEXION 300X (PERKIN ELMER). A piece of 1 cm2 of Ni-free/3DG Copolymer were mineralized (700W, 40 minutes). 10 ppb of internal standard (Multielement standard solution for ICP -TraceCERT®) was added.

Photoluminescence (PL) analyses.
PL measurements were performed by sampling the same surface areas of the photocatalyst and reference as well (1 cm2), at room temperature by an He-Cd laser (excitation wavelength of 325 nm). PL signals have been recorded by a monochromator and a water-cooled Hamamatsu photomultiplier.

Cyclic voltammetry measurements.
Electrochemical analyses were performed to measure the HOMO and LUMO energy values of the Porph rings by using a potentiostat (VersaSTAT 4, Princeton Applied Research, USA) and a three-electrode setup with Pt wires as working and counter electrodes, a saturated calomel electrode (SCE) as reference electrode and 0.1 M tetrabutylammoniumhexafluorophosphate (TBAPF6) as supporting electrolyte. The experiments were carried out on three different dichloromethane solutions containing 1 mg of porphyrin copolymer, 1 mg of porphyrin monomer and TBAPF6. For each experiment dichloromethane solvent was preventively passed in molecular sieves and ferrocene was used as an internal standard (Figure S5). To evaluate the HOMO energy level we measured the optical bandgap (Eg) from the maximum value of the Qy (0,0) absorption band (554 nm) of UV-vis spectrum of Porph rings (Figure S6) by using $Eg=hc/\lambda onset$ where h is the Planck constant (6.63x10-34 m2 Kg s-1) and c is the speed of light (3x108 m s-1).

Synthesis of Ni-foam GF.
Synthesis of Ni-G samples were performed in AIXTRON's Black Magic Chemical Vapor Deposition (CVD) system [19]. Systems was heated at 900°C for 20 minutes under Ar and H_2 flows (600 and 400 sccm, respectively) to eliminate the residual thin surface oxide layer before Graphene growth. After, the chamber was heated up to 1000°C and the CH_4 flow was opened for 40 minutes (flow rates of 20, 600 and 1000 sccm for CH_4, Ar and H2, respectively) and then cooled down at 15°C/min to grow the graphene layers on the Ni foam surface.
Characterization of graphene in terms of quality and number of layers was performed by Raman spectra.

Synthesis of 5,10-di[p-(9-methoxytriethylenenoxy)phenyl]-15,20-di[p-hydroxyphenyl]-porphyrin monomer.
The monomer was synthesized by reaction between tetrakis-p(hydroxyphenyl)-porphyrin and 9-methyltriethyleneoxy chloride in aqueous alkaline solution, as reported elsewhere [21].

Synthesis of 5,10-di[p-(9-methoxytriethylenenoxy)phenyl]-15,20-di[p-hydroxyphenyl]-zinc porphyrin monomer.
Zinc 5,10-di[p-(9-methoxytriethylenenoxy)phenyl]-15,20-di[p-hydroxyphenyl]-porphyrin complex was obtained, as previously reported, by reaction between the 5,10-di[p-(9 methoxytriethylenenoxy)phenyl]-15,20-di[p-hydroxyphenyl] porphyrin and the teen excesses fold of zinc acetate in pyridine [22].

Synthesis of 1,20-di(bisphenoxy-A)eicosane monomer.
1,20-di(bisphenoxy-A)eicosane was obtained from 1,20-dibromo-eicosane and bisphenol-A according to the method mentioned elsewhere [21].

Synthesis of porphyrin homopolymers (CPH). The homopolyformal was synthesized according to the method described elsewhere23 by reaction of 5,10-di[p-(9-methoxytriethylenenoxy)phenyl]−15,20-di[p-hydroxyphenyl]-porphyrin with CH_2Br_2. In a 2 mL vial, equipped with magnetic stirrer and placed in a water bath at 70 °C, 10 mg (0.01 mmol) of 5,10-di[p-(9-methoxytriethylenenoxy)phenyl]−15,20-di[p-hydroxyphenyl]-porphyrin were solubilized in 0.5 mL of N-methylpirrolidinone (NMP) together with 3 mg (a large molar excess)

of powdered KOH. After 1hour, 0.3mL of CH2Br2 (a large excess) were added and the vial closed. After 24hours, the solution was poured into 5mL of 5% HCl under vigorous stirring and the obtained suspension was centrifuged to give a purple polymeric residue. The material was solubilized in 2mL of THF, precipitated in 5mL of water, centrifuged and dried in vacuum for 24hours (yield about 80%). Te polymer was characterized by MALDI-TOF mass spectrometry, GPC and UV-Vis spectroscopy. CPH based on zinc-porphyrin monomer was synthesized in a similar way starting from the specifc porphyrin derivative.

Synthesis of porphyrin copolymer (CPC).

Random copolymer was synthesized by interfacial etherifcation reaction. According to the method described elsewhere22, tetrabutylammonium bromide (TBAB) as the phase-transfer agent and a 50% (in moles) mixture of monomers were used, in the presence of a large excess of dibromomethane. Typically, 11 mg of 5,10-di[p-(9-methoxytriethylenenoxy)phenyl]−15,20-di[p-hydroxyphenyl]-porphyrin (0.011 mmol) and 8.1 mg of di(bisphenoxy-A)eicosane (0.011mmol) were solubilized in 3mL of toluene in a 10mL closed vial and heated at 70 °C. Ten, 4mg of NaOH (0.1mmol, a large molar excess), solubilised in 1mL of water together with 7.1mg of TBAB (0.022 mmol), were added and the solution was stirred at the same temperature for 1 hour before adding 0.5 mL of CH_2Br_2. After 24 hours, the organic solution was separated from the aqueous one and poured, under stirring, into a solution of 10mL of EtOH acidified by 0.5mL of CH3COOH. After separation by centrifugation, the precipitated material was dissolved in THF and precipitated in EtOH a further two times, washed with H_2O, and then dried under vacuum. 14mg of a purple fibrous polymeric material was recovered with a yield of about 75%. The copolymer was characterized by MALDI-TOF mass spectrometry, GPC and UV-Vis spectroscopy.

Hybrid nanocomposites preparation

To prepare hybrid nanocomposites, 2D and 3D (pieces of 15 mm×10 mm) graphene were immersed in 10 mg/ml of porphyrin solutions. In particular, in the case of 2D-G were used three different solvents, dimethylformamide (DMF), tetrahydrofuran (THF) and chloroform (CHCl3). After 12 h, the THF and $CHCl_3$ samples were removed from vials, washed and dried at room temperature, whereas materials

obtained by using DMF as a solvent were dried under vacuum at 50 °C overnight.

Ni free-GF/CPC preparation.
About 10 mg of CPC was dissolved in 1 mL of dimethylformamide (DMF). GF pieces of 1 cm^2 were covered by spin-coating a DMF solution 10mg/ml of porph rings. The specimens were dried on a hot plate (80°C) for 40 minutes and overnight in a under vacuum oven at 60 °C. Then, samples were immersed in HCl (1M) for 12 hours. Finally, after washing in fresh distilled water the samples were dried in oven for two hours at 45°C.

Photocatalytic activity on Ni-foam 2D-G and GF hybrids.
The variation of the concentration of MB was spectrophotometrically evaluated by using a PerkinElmer Lambda 45 UV–Vis spectrophotometer. The concentrations of MB solutions were optimized in function of their absorbance, avoiding high concentrations that induce shielding effect. At the same time, the loss of signals for higher exposure times (low absorbance values) was prevented. At this purpose, MB was prepared at 0.015 mM at pH 7.5. The water-insoluble hybrid device was immersed in the solutions, and the absorbance data were recorded in the dark for several hours to allow the absorption–desorption equilibrium. Subsequently, when the absorption values in the dark were constant, the samples were exposed to visible-light irradiation with a xenon lamp operating at 1.5 mW/cm2 and equipped with a cut-on filter 400 nm. At given time intervals of 1 h for 5 h, the concentration of the MB was spectrophotometrically evaluated, observing the absorption peaks at 664 nm.

Photocatalytic tests on Ni-free GF/CPC.
The photocatalytic efficiency of the hybrid materials was evaluated versus 2,4-D, PEG having a Mn 1900 Da, as well as MB water solutions under visible-light irradiation. All solutions were saturared by bubbling air every 10 minutes per hours, and were irradiated by the solar simulator VeraSol-2 from Oriel by Newport corresponding to AM1.5 G in the visible and near-infrared region (400–1100 nm) with a light irradiance of 100 ± 3 mW cm−2. Specifically, MB degradation tests were performed by removing the irradiation in the range 600-700 nm to suppress MB absorption (see Figure S14). 1 cm^2 of sample was immersed in 2 ml of the target solution (0,015 Mm) and left overnight

in the dark up to the adsorption-desorption equilibrium. The variation of MB concentrations was spectrophotometrically evaluated observing the absorption at 664 nm. The photodegradation ratio was defined as (A0 – A)/A0 where A is the absorption of the dye at a certain time and A0 represents the absorption value of the MB initial concentration.
With regards to 2,4-D photodegradation tests, 1 cm^2 of device was immersed in 2 mL of herbicide solution (0,005 mM) and irradiated for 6 hours. Control experiments were carried out in the dark for 30 minutes to ensure the adsorption–desorption equilibrium of the herbicide. The photodegradation products were determined by the ESI-MS as well as UV-Vis measurements, following also the degradation by UV-Vis and TOC analyses. Finally, to evaluate the photodegradation ability versus polyethylene-oxide (PEG), 1 cm^2 of speciment was immersed in 2 ml of polymer acqueous solution (0,5 mg/mL). To estimate the photodegradation process, MALDI-TOF spectra were acquired up to 6 hours of photoexposure, while mineralization of PEG was monitored by measuring the TOC. Tests in absence of photocatalysts were also performed as black reference.

Radical trapping measurements.
1 mL of MB aqueous solutions ($1x10^{-5}$ M) were mixed with 1 mL of radical- and hole-trapping agent solutions ($1x10^{-3}$ M) with absorbance adjusted around 1.0. When the adsorption-desorption equilibrium was reached, all mixed solutions were saturared by bubbling air for 15 minutes for each hour. The cuvettes were exposed to the solar simulation in the same conditions reported above for the photocatalytic test. The MB degradation rate was evaluated by monitoring the absorbance values at 664 nm for two hours. Triplicate data was collected for each irradiation time.

Conclusions

In this section, hybrid graphene-based composites were proposed as new photocatalytic systems for degradation of conventional and emerging pollutants in water. In particular, high-quality graphene supports coated by porphyrin-based polymers photocatalysts were able to protect graphene from the shielding effect, radical scavenger activity as well as protection during the Ni etching of 3D structures from defects formation and collapse. Furthermore, it was demonstrated how π-π interactions at the graphene/polymer interface were crucial to promote the electron-transfer process resulting in freestanding materials with outstanding photocatalytic performances versus selected target pollutants, such as 2,4-D herbicide, MB and PEG samples. By radical trapping measurements the singlet oxygen was recognized as the predominant species produced, although the other ROS are also produced assisting the contaminants degradation. Finally, RAFT polymerization was introduced as a promising tool to obtain different polymer porphyrin-based photosensitizers for the preparation of novel hybrid graphene-based composites eventually studying their photocatalytic efficiency.

References

[1] Marin, M. L., Santos-Juanes, L., Arques, A., Amat, A. M., & Miranda, M. A. (2011). Organic photocatalysts for the oxidation of pollutants and model compounds. Chemical reviews, 112(3), 1710-1750.

[2] Chen, Y., Li, A., Huang, Z. H., Wang, L. N., & Kang, F. (2016). Porphyrin-based nanostructures for photocatalytic applications. Nanomaterials, 6(3), 51.

[3] Guo, P., Chen, P., Ma, W., & Liu, M. (2012). Morphology-dependent supramolecular photocatalytic performance of porphyrin nanoassemblies: from molecule to artificial supramolecular nanoantenna. Journal of Materials Chemistry, 22(38), 20243-20249.

[4] Hasobe, T. (2012). Photo-and electro-functional self-assembled architectures of porphyrins. Physical Chemistry Chemical Physics, 14(46), 15975-15987.

[5] Wang, J., Zhong, Y., Wang, L., Zhang, N., Cao, R., Bian, K., ... & Fan, H. (2016). Morphology-controlled synthesis and metalation of porphyrin nanoparticles with enhanced photocatalytic performance. Nano letters, 16(10), 6523-6528.

[6] Wojcik, A., & Kamat, P. V. (2010). Reduced graphene oxide and porphyrin. An interactive affair in 2-D. ACS nano, 4(11), 6697-6706.

[7] Chen, Y., Huang, Z. H., Yue, M., & Kang, F. (2014). Integrating porphyrin nanoparticles into a 2D graphene matrix for free-standing nanohybrid films with enhanced visible-light photocatalytic activity. Nanoscale, 6(2), 978-985.

[8] Zhu, M., Li, Z., Xiao, B., Lu, Y., Du, Y., Yang, P., & Wang, X. (2013). Surfactant assistance in improvement of photocatalytic hydrogen production with the porphyrin noncovalently functionalized graphene nanocomposite. ACS applied materials & interfaces, 5(5), 1732-1740.

[9] Han, L., Wang, P., & Dong, S. (2012). Progress in graphene-based photoactive nanocomposites as a promising class of photocatalyst. Nanoscale, 4(19), 5814-5825.

[10] Lu, Q., Zhang, Y., & Liu, S. (2015). Graphene quantum dots enhanced photocatalytic activity of zinc porphyrin toward the degradation of methylene blue under visible-light irradiation. Journal of Materials Chemistry A, 3(16), 8552-8558.

[11] Wang, A., Yu, W., Huang, Z., Zhou, F., Song, J., Song, Y., ... & Shao, J. (2016). Covalent functionalization of reduced graphene oxide with porphyrin by means of diazonium chemistry for nonlinear optical performance. Scientific reports, 6, 23325.
[12] Karousis, N., Sandanayaka, A. S., Hasobe, T., Economopoulos, S. P., Sarantopoulou, E., & Tagmatarchis, N. (2011). Graphene oxide with covalently linked porphyrin antennae: Synthesis, characterization and photophysical properties. Journal of Materials Chemistry, 21(1), 109-117.
[13] Yamuna, R., Ramakrishnan, S., Dhara, K., Devi, R., Kothurkar, N. K., Kirubha, E., & Palanisamy, P. K. (2013). Synthesis, characterization, and nonlinear optical properties of graphene oxide functionalized with tetra-amino porphyrin. Journal of nanoparticle research, 15(1), 1399.
[14] Krishna, M. B. M., Venkatramaiah, N., Venkatesan, R., & Rao, D. N. (2012). Synthesis and structural, spectroscopic and nonlinear optical measurements of graphene oxide and its composites with metal and metal free porphyrins. Journal of Materials Chemistry, 22(7), 3059-3068.
[15] Ge, R., Wang, X., Zhang, C., Kang, S. Z., Qin, L., Li, G., & Li, X. (2015). The influence of combination mode on the structure and properties of porphyrin–graphene oxide composites. Colloids and Surfaces A: Physicochemical and Engineering Aspects, 483, 45-52.
[16] Mandal, S., Nayak, S. K., Mallampalli, S., & Patra, A. (2013). Surfactant-assisted porphyrin based hierarchical nano/micro assemblies and their efficient photocatalytic behavior. ACS applied materials & interfaces, 6(1), 130-136.
[17] Qiu, P., Yao, J., Chen, H., Jiang, F., & Xie, X. (2016). Enhanced visible-light photocatalytic decomposition of 2, 4-dichlorophenoxyacetic acid over ZnIn2S4/g-C3N4 photocatalyst. Journal of hazardous materials, 317, 158-168.
[18] Fiorenza, R., Di Mauro, A., Cantarella, M., Iaria, C., Scalisi, E. M., Brundo, M. V., ... & Carroccio, S. C. (2020). Preferential removal of pesticides from water by molecular imprinting on TiO2 photocatalysts. Chemical Engineering Journal, 379, 122309.
[19] Zhang, N., Yang, M. Q., Tang, Z. R., & Xu, Y. J. (2013). Toward improving the graphene–semiconductor composite photoactivity via the addition of metal ions as generic interfacial mediator. ACS nano, 8(1), 623-633.

[20] Yang, S. T., Chen, S., Chang, Y., Cao, A., Liu, Y., & Wang, H. (2011). Removal of methylene blue from aqueous solution by graphene oxide. Journal of colloid and interface science, 359(1), 24-29.
[21] Vitalini, D., & Scamporrino, E. (1992). Main chain porphyrin polymers. 2. Synthesis and characterization of some copolyethers and their metal derivatives. Macromolecules, 25(24), 6605-6611.
[22] Scamporrino, E., Mineo, P., & Vitalini, D. (2011). Covalent nano-clip and nano-box compounds based on free base porphyrins. Tetrahedron, 67(20), 3705-3713.
[23] Angelini, N., Micali, N., Mineo, P., Scamporrino, E., Villari, V., & Vitalini, D. (2005). Uncharged Water-Soluble Co (II)− Porphyrin: A Receptor for Aromatic α-Amino Acids. The Journal of Physical Chemistry B, 109(39), 18645-18651.
[24] Vitalini, D., Mineo, P., & Scamporrino, E. (1999). Synthesis and characterization of some main chain porphyrin copolyformals, based on bisphenol A and long linear aliphatic units, having a low glass transition temperature. Macromolecules, 32(1), 60-69.
[25] Su, W. F. (2013). Principles of polymer design and synthesis (Vol. 82). Berlin, Heidelberg: Springer.
[26] Guang, L., Hui, W., & Xuejun, Z. (2016). Effect of drying temperatures on structural performance and photocatalytic activity of BiOCl synthesized by a soft chemical method. Journal of Solid State Chemistry, 239, 259-264.
[27] Sobczyński, J., Tønnesen, H. H., & Kristensen, S. (2013). Influence of aqueous media properties on aggregation and solubility of four structurally related meso-porphyrin photosensitizers evaluated by spectrophotometric measurements. Die Pharmazie-An International Journal of Pharmaceutical Sciences, 68(2), 100-109.
[28] Ribeiro, V., Marcelo, A., da Silva, K., da Silva, F., Mota, J., do Nascimento, J., ... & Mazzetto, S. (2017). New ZnO@ Cardanol porphyrin composite nanomaterials with enhanced photocatalytic capability under solar light irradiation. Materials, 10(10), 1114.
[29] La, D. D., Bhosale, S. V., Jones, L. A., Revaprasadu, N., & Bhosale, S. V. (2017). Fabrication of a Graphene@ TiO2@ Porphyrin hybrid material and its photocatalytic properties under simulated sunlight irradiation. ChemistrySelect, 2(11), 3329-3333.
[30] Ahmed, M. A., Abou-Gamra, Z. M., Medien, H. A. A., & Hamza, M. A. (2017). Effect of porphyrin on photocatalytic activity of TiO2

nanoparticles toward Rhodamine B photodegradation. Journal of Photochemistry and Photobiology B: Biology, 176, 25-35.
[31] Zhang, Y. I., Zhang, L., & Zhou, C. (2013). Review of chemical vapor deposition of graphene and related applications. Accounts of chemical research, 46(10), 2329-2339.
[32] Pellegrino, G., Alberti, A., Condorelli, G. G., Giannazzo, F., La Magna, A., Paoletti, A. M., ... & Zanotti, G. (2013). Study of the anchoring process of tethered unsymmetrical Zn-phthalocyanines on TiO2 nanostructured thin films. The Journal of Physical Chemistry C, 117(21), 11176-11185.
[33] Pellegrino, G., Condorelli, G. G., De Rossi, F., Brown, T. M., Giovenale, F., Bongiorno, C., & Alberti, A. (2014). Thermally induced structural modifications of nano-sized anatase films and the effects on the dye-TiO2 surface interactions. Applied Surface Science, 296, 69-78.
[34] Sarno, D. M., Matienzo, L. J., & Jones, W. E. (2001). X-ray photoelectron spectroscopy as a probe of intermolecular interactions in porphyrin polymer thin films. Inorganic chemistry, 40(24), 6308-6315.
[35] Moore, K. T., Horváth, I. T., & Therien, M. J. (2000). Mechanistic studies of (porphinato) iron-catalyzed isobutane oxidation. Comparative studies of three classes of electron-deficient porphyrin catalysts. Inorganic chemistry, 39(15), 3125-3139.
[36] Iovine, P. M., Kellett, M. A., Redmore, N. P., & Therien, M. J. (2000). Syntheses and 1H NMR Spectroscopy of Rigid, Cofacially Aligned, Porphyrin− Bridge− Quinone Systems in Which the Interplanar Separations between the Porphyrin, Aromatic Bridge, and Quinone Are Less than the Sum of Their Respective van der Waals Radii. Journal of the American Chemical Society, 122(36), 8717-8727.
[37] Polzonetti, G., Ferri, A., Russo, M. V., Iucci, G., Licoccia, S., & Paolesse, R. (1999). Platinum complex/Zn-porphyrin macrosystem assemblies: Electronic structure and conformational investigation by x-ray photoelectron spectroscopy. Journal of Vacuum Science & Technology A: Vacuum, Surfaces, and Films, 17(3), 832-839.
[38] Pellegrino, G., Condorelli, G. G., Privitera, V., Cafra, B., Di Marco, S., & Alberti, A. (2011). Dye-sensitizing of self-nanostructured Ti (: Zn) O2/AZO transparent electrodes by self-assembly of 5, 10, 15,

20-tetrakis (4-carboxyphenyl) porphyrin. The Journal of Physical Chemistry C, 115(15), 7760-7767.
[39] Yamashige, H., Matsuo, S., Kurisaki, T., Perera, R. C., & Wakita, H. (2005). Local structure of nitrogen atoms in a porphine ring of meso-phenyl substituted porphyrin with an electron-withdrawing group using X-ray photoelectron spectroscopy and X-ray absorption spectroscopy. Analytical sciences, 21(6), 635-639.
[40] Impellizzeri, G., Scuderi, V., Romano, L., Napolitani, E., Sanz, R., Carles, R., & Privitera, V. (2015). C ion-implanted TiO2 thin film for photocatalytic applications. Journal of Applied Physics, 117(10), 105308.
[41] Zhong, Y., Wang, Z., Zhang, R., Bai, F., Wu, H., Haddad, R., & Fan, H. (2014). Interfacial self-assembly driven formation of hierarchically structured nanocrystals with photocatalytic activity. ACS nano, 8(1), 827-833.
[42] Chen, Y., Zhang, C., Zhang, X., Ou, X., & Zhang, X. (2013). One-step growth of organic single-crystal p–n nano-heterojunctions with enhanced visible-light photocatalytic activity. Chemical Communications, 49(80), 9200-9202.
[43] Crowder, S. W., Prasai, D., Rath, R., Balikov, D. A., Bae, H., Bolotin, K. I., & Sung, H. J. (2013). Three-dimensional graphene foams promote osteogenic differentiation of human mesenchymal stem cells. Nanoscale, 5(10), 4171-4176.
[44] Chen, Z., Xu, C., Ma, C., Ren, W., & Cheng, H. M. (2013). Lightweight and flexible graphene foam composites for high-performance electromagnetic interference shielding. Advanced materials, 25(9), 1296-1300.
[45] Chen, Z., Ren, W., Gao, L., Liu, B., Pei, S., & Cheng, H. M. (2011). Three-dimensional flexible and conductive interconnected graphene networks grown by chemical vapour deposition. Nature materials, 10(6), 424.
[46] Aly, S. M., Parida, M. R., Alarousu, E., & Mohammed, O. F. (2014). Ultrafast electron injection at the cationic porphyrin–graphene interface assisted by molecular flattening. Chemical Communications, 50(72), 10452-10455.
[47] Bajjou, O., Mongwaketsi, P. N., Khenfouch, M., Bakour, A., Baïtoul, M., Maaza, M., & Venturini, J. W. (2015). Photoluminescence quenching and structure of nanocomposite based on graphene oxide layers decorated with nanostructured porphyrin. Nanomaterials and Nanotechnology, 5,7.

[48] Garrido-Barros, P., Gimbert-Suriñach, C., Moonshiram, D., Picón, A., Monge, P., Batista, V. S., & Llobet, A. (2017). Electronic π-delocalization boosts catalytic water oxidation by Cu (II) molecular catalysts heterogenized on graphene sheets. Journal of the American Chemical Society, 139(37), 12907-12910.
[49] El-Shafai, N., El-khouly, M. E. S., El-Kemary, M., & Masoud, M. S. (2019). Self-assembly of porphyrin on graphene oxide in aqueous medium: fabrication, characterization, and photocatalytic studies. Photochemical & Photobiological Sciences.
[50] Giroto, J. A., Teixeira, A. C., Nascimento, C. A., & Guardani, R. (2010). Degradation of poly (ethylene glycol) in aqueous solution by photo-Fenton and H2O2/UV processes. Industrial & Engineering Chemistry Research, 49(7), 3200-3206.
[51] Vijayalakshmi, S. P., & Madras, G. (2006). Photocatalytic degradation of poly (ethylene oxide) and polyacrylamide. Journal of applied polymer science, 100(5), 3997-4003.
[52] Hassouna, F., Mailhot, G., Morlat-Thérias, S., & Gardette, J. L. (2008). Photochemical behaviour of poly (ethylene oxide)(PEO) in aqueous solution: Influence of iron salts. Journal of Photochemistry and Photobiology A: Chemistry, 195(2-3), 167-174.
[53] Morlat, S., & Gardette, J. L. (2003). Phototransformation of water-soluble polymers. Part II: photooxidation of poly (ethylene oxide) in aqueous solution. Polymer, 44(26), 7891-7897.
[54] Chen, H., Zhang, Z., Yang, Z., Yang, Q., Li, B., & Bai, Z. (2015). Heterogeneous fenton-like catalytic degradation of 2, 4-dichlorophenoxyacetic acid in water with FeS. Chemical Engineering Journal, 273, 481-489.
[55] Oturan, N., Panizza, M., & Oturan, M. A. (2009). Cold incineration of chlorophenols in aqueous solution by advanced electrochemical process electro-Fenton. Effect of number and position of chlorine atoms on the degradation kinetics. The Journal of Physical Chemistry A, 113(41), 10988-10993.
[56] Dias, F. B., Santos, J., Graves, D. R., Data, P., Nobuyasu, R. S., Fox, M. A., ... & Monkman, A. P. (2016). The role of local triplet excited states and D-A relative orientation in thermally activated delayed fluorescence: photophysics and devices. Advanced Science, 3(12), 1600080.

[57] DeRosa, M. C., & Crutchley, R. J. (2002). Photosensitized singlet oxygen and its applications. Coordination Chemistry Reviews, 233, 351-371.
[58] Nosaka, Y., & Nosaka, A. Y. (2017). Generation and detection of reactive oxygen species in photocatalysis. Chemical reviews, 117(17), 11302-11336.
[59] Ding, K., Zhang, Y., Si, W., Zhong, X., Cai, Y., Zou, J., ... & Dong, X. (2017). Zinc (II) Metalated Porphyrins as Photothermogenic Photosensitizers for Cancer Photodynamic/Photothermal Synergistic Therapy. ACS applied materials & interfaces, 10(1), 238-247.
[60] Seema, H., Kemp, K. C., Chandra, V., & Kim, K. S. (2012). Graphene–SnO2 composites for highly efficient photocatalytic degradation of methylene blue under sunlight. Nanotechnology, 23(35), 355705.
[61] Leonat, L., Sbarcea, G., & Branzoi, I. V. (2013). Cyclic voltammetry for energy levels estimation of organic materials. UPB Sci Bull Ser B, 75, 111-118.
[62] Shafiee, A., Salleh, M. M., & Yahaya, M. (2011). Determination of HOMO and LUMO of [6, 6]-phenyl C61-butyric acid 3-ethylthiophene ester and poly (3-octyl-thiophene-2, 5-diyl) through voltametry characterization. Sains Malaysiana, 40(2), 173-176.
[63] Pan, L., Hu, B., Zhu, X., Chen, X., Shang, J., Tan, H., ... & Li, R. W. (2013). Role of oxadiazole moiety in different D–A polyazothines and related resistive switching properties. Journal of Materials Chemistry C, 1(30), 4556-4564.
[64] Srour, H., Doan, T. H., Da Silva, E., Whitby, R. J., & Witulski, B. (2016). Synthesis and molecular properties of methoxy-substituted diindolo [3, 2-b: 2′, 3′-h] carbazoles for organic electronics obtained by a consecutive twofold Suzuki and twofold Cadogan reaction. Journal of Materials Chemistry C, 4(26), 6270-6279.
[65] Chiefari, J., Chong, Y. K., Ercole, F., Krstina, J., Jeffery, J., Le, T. P., ... & Rizzardo, E. (1998). Living free-radical polymerization by reversible addition− fragmentation chain transfer: the RAFT process. Macromolecules, 31(16), 5559-5562.
[66] Corpart, P., Charmot, D., Biadatti, T., Zard, S. Z., & Michelet, D. (1998). Method for block copolymer synthesis by controlled radical polymerization. Pat. Num. WO, 98, 9858974.

[67] Jenkins, A. D., Jones, R. G., & Moad, G. (2009). Terminology for reversible-deactivation radical polymerization previously called" controlled" radical or" living" radical polymerization (IUPAC Recommendations 2010). Pure and Applied Chemistry, 82(2), 483-491.
[68] Moad, G., Rizzardo, E., & Thang, S. H. (2006). Living radical polymerization by the RAFT process—a first update. Australian Journal of Chemistry, 59(10), 669-692.
[69] Moad, G., Rizzardo, E., & Thang, S. H. (2009). Living radical polymerization by the RAFT process–a second update. Australian Journal of Chemistry, 62(11), 1402-1472.
[70] Moad, G., Rizzardo, E., & Thang, S. H. (2012). Living radical polymerization by the RAFT process–a third update. Australian Journal of Chemistry, 65(8), 985-1076.
[71] Perrier, S., & Takolpuckdee, P. (2005). Macromolecular design via reversible addition–fragmentation chain transfer (RAFT)/xanthates (MADIX) polymerization. Journal of Polymer Science Part A: Polymer Chemistry, 43(22), 5347-5393.
[72] Kulikov, E. E., Zaitsev, S. D., & Semchikov, Y. D. (2015). Reversible addition-fragmentation chain transfer (RAFT)(Co) polymerization of isobornyl acrylate. Polymer Science Series C, 57(1), 120-127.

CHAPTER 3

HYBRID ADSORBITIVE MATERIALS

In chapter one it was highlighted how the current water purification methods are unable to meet the present needs from environmental and economical point of views; in fact, many of the procedures used today, including sedimentation, filtration, chemical methods, and reverse osmosis, already established in the beginning of the 20th century, fail to satisfy many requirements. Indeed, they involve high operating costs and could generate toxic secondary pollutants into the ecosystem.
In this context, from technology point of view, adsorption methods hold many advantages being feasible, efficient, and low-cost.
Various adsorbents, such as carbon-based materials, [1,2] clay, [3,4] natural and synthetic polymers [5-7] as well as organic−inorganic composites [8], have been extensively studied and applied in wastewater treatment to selectively capture conventional and emerging pollutants. Even though adsorption can efficiently remove contaminants from water, this process presents a critical issue: whatever the adsorbing phase is, it is not able to eliminate the adsorbed pollutants in a permanent way. Therefore, further disposal is required to avoid the simple transfer of contaminants from one phase to another one [9]. In light of this, the development of new generation hybrid adsorbents combined with photocatalytic materials seems to be a promising solution to obtain systems easily separable after the water purification process.
In this chapter, the design of novel multifunctional nanocomposites will be reported, introducing also the cryopolymerization process in water as a green method to produce superabsorbent sponges. A key role will be also reserved to the use of graphene derivatives as a filler to improve the selectivity, surface area and chemistry, mechanical strength, regeneration properties or a combination of these features.

3.1 Adsorption

The adsorption process is a method commonly used for several purposes in the academy and industry. In particular, it is used to remove recalcitrant compounds from effluents, and to purify products during the industrial processing [10]. Generally, adsorption is referred to a surface process which ions and molecules (adsorbates) are transferred from a solution phase to the surface of a solid phase (adsorbent), up to the equilibrium is reached. In particular, the adsorbates/adsorbent interaction can be classified as chemisorption or physical adsorption. The latter is a rapid process driven by non-specific binding (non-covalent bonds) that require low energies ranging from 4 to 40 kJ/mol. As a consequence, physical adsorption being a reversible process is the most common used in water treatment. Differently, chemisorption involves high-energy (40-800 kJ/mol) and specific interactions. In this case, chemical reactions occur, involving the transfer of electron pairs between adsorbent and adsorbate to establish a chemical bond with the surface. Due to the chemical nature of the interactions chemisorption is usually not reversible. When the desorption process occurs, it is accompanied by an irreversible chemical modification in the adsorbate. On the basis of these fundamental concepts, to develop a suitable adsorption system the adsorbent choice is the first requirement. Along this, other specific features have to be included, such as low cost, availability, efficiency, high surface area and pore volume, mechanical, chemical, and thermal stability. A fast kinetic and, high adsorption capacity are also required [10]. The equilibrium capacity and kinetics are the major affecting factors of the adsorption process, influenced by the surface affinity for different species, physicochemical and morphological features, surface charge and area as well as the porosity. Furthermore, operational parameters such as pH, temperature, and co-existing species in the solution also influence the adsorptive performance, and a deep study and optimization of the influencing factors are necessary before applying the system at full scale.

3.1.1 Kinetics and isotherms

The adsorption process is often described at the equilibrium through equations called isotherms, that quantify the amount of substance adherent to the surface. These equations provide parameters related to the adsorption capacity of a particular adsorbent, adsorbent–adsorbate interactions, as well as thermodynamic parameters. In static conditions, the most applied models are the pseudo-first-order, pseudo-second-order, and intraparticle diffusion models [11,12].

The pseudo-first-order model presented by Lagergren is based on the solid capacity to adsorb and is given by equation 3.1 [10].

$$\frac{dQt}{dt} = k_1(Q_e - Q_t) \tag{3.1}$$

where Qe and Q_t (mg g $^{-1}$) are the adsorption capacities at equilibrium and at time t (min), respectively, and k_1 (min^{-1}) is the pseudo-first-order rate constant of the kinetic model. Integration of equation using the initial conditions of Qt = 0 at t = 0 leads to equation 3.2:

$$\ln\left[\frac{Q_e}{Q_e - Q_t}\right] = k_1 t \tag{3.2}$$

which can be rewritten as:

$$\ln(Q_e - Q_t) = \ln Q_e - k_1 t \tag{3.3}$$

This model is normally used when the adsorption operation is fast, attaining the equilibrium within 20−30 min. In the second-order model, the driving force ($Q_e - Q_t$) is proportional to the available fraction of active sites, and it can be written as

$$\frac{dQ_t}{dt} = k_2(Q_e - Q_t)^2 \quad (3.4)$$

and integration of equation 4 leads to

$$\frac{1}{(Q_e - Q_t)} = \frac{1}{Q_e} + k_2 t \quad (3.5)$$

This last equation can be rewritten as follows

$$\frac{t}{Q_t} = \frac{1}{k_2 Q_e^2} + \frac{t}{Q_e} \quad (3.6)$$

The second-order rate equation has been successfully applied to the adsorption of metal ions, dyes, and organic substances from aqueous solutions. Several studies for adsorption of divalent metals reported that the majority of the sorption kinetics follows the pseudo-second-order mechanism [13,14]. A functional relationship common to most of the treatments of intraparticle diffusion is that the uptake varies almost proportionately with the half-power of time ($t^{0.5}$), rather than t. Good linearization of the data is observed for the initial phase of the reaction in accordance with the expected behavior if intraparticle diffusion is the rate-limiting step [15,16]. The intraparticle diffusion model is expressed by the following equation:

$$Q_t = k_i\sqrt{t} + C \quad (3.7)$$

where k_i is the intraparticle diffusion rate constant (mg g^{-1} $h^{-0.5}$). The k_i values are calculated from the slope of the straight line of the respective plots. The plot of Qt versus $t^{0.5}$ may present multilinearity, which indicates that two or more rate-controlling steps occur in the adsorption process.

3.2 Cryosponges

Freeze-thawed cryogels, or more commonly cryogels are polymeric materials formed via the cryogenic treatment of liquids or dispersion of appropriate precursors, summarized in **Figure 3.1**. Cryogelation is a radical polymerization activated at sub-zero temperatures, able to form crosslinked and macroporous gel networks characterized by pores with dimensions ranging from 5 to 100 mm, depending on the temperature of the process. In particular, the frozen solution is an heterophase system containing both solids and some unfrozen liquid microphase, where the solutes are concentrated. Thus, gelation can only occur within the latter unfrozen regions of the system, while the crystals of frozen solvents act as porogens. More importantly, as a consequence, materials obtained by using this method, possess a high porosity (usually in the range of 80-90%) gaining more and more attention by scientific community in water purification processes [17-19]. Indeed, the peculiarity of interconnected pores provides high absorption capability, making them suitable as superabsorbent materials with a versatile platform to adsorb both, organic and inorganic contaminants.

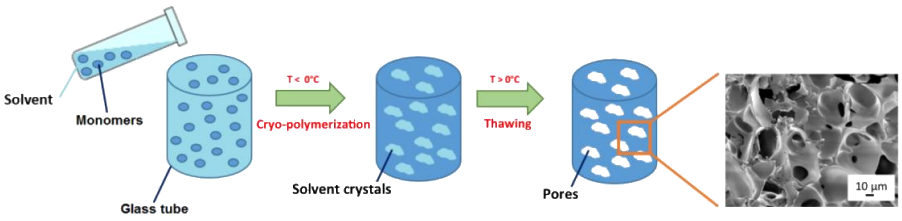

Figure 3.1. Schematic illustration showing the different steps involved during the cryopolymerization process.

3.3 ZnO-based cryosponges for dye removal

As previously discussed, one of the major challenges in the framework of adsorption process, is the development of new generation of adsorptive materials able to remove contaminants in a permanent way. However, an ecofriendly and definitive approach to degrade contaminants through their complete mineralization exploits the photocatalytic process [20,21]. In this context, the “bait-hook-and-destroy” concept for the design of high-capacity absorptive materials combined with photocatalysts (see **Figure 3.2**) for more efficient degradation is an appealing and promising solution as well [22].

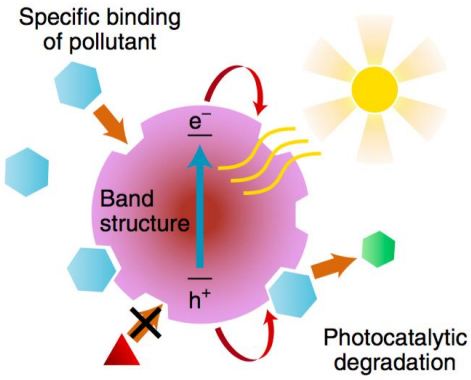

Figure 3.2. Bait-hook-destroy concept for selective removal of pollutants via adsorption of higher pollutant concentration for faster destruction by photocatalysis [Adapted from Ref. [22] with kind permission of the Wiley-VCH].

As reported in literature, photocatalysis by using ZnO semiconductor materials has attracted huge attention, stimulating several synthetic strategies with the aim to boost photocatalytic and visible-light-active performances [23-25]. Compared to the most common used inorganic semiconductors, ZnO is a wide band-gap (~3 eV) material, relatively easy and cheap to prepare, with great photocatalytic properties, [26-30], and thermodynamically stable in its hexagonal wurtzite structure

[31-33]. As already mentioned in the previous chapters, the major barrier that restrains the commercialization of such kind of photocatalyst is its post-recovery after water treatment. If nanoparticles are not removed, they can exhibit serious toxicity to aquatic and human life [34]. With this in mind, researchers have been drawing the attention to a practical and safe application of such kind of nanomaterials by using polymers to support them [35-37]. Among the great variety of materials used for water purification applications, cryogels have attracted interest, due to their peculiar properties. Moreover, depending on the precursor monomer, semiconductors can be covalently attached to the polymeric structure by chemical functionalization via bath deposition or atomic layer deposition as well. The use of ZnO through a stable covalent linkage between the polymeric support and the photocatalyst can provide a freestanding material, easily and safely removable from the polluted site and able to degrade pollutants after each adsorption step. Clearly, this represents a crucial advantage. Indeed, good adsorbent devices reported in the recent literature present excellent performance in terms of dye removal, although their regeneration is still arduous [38-39].
In the next sections the formulation of a novel multifunctional material will be discussed, combining in a single system both, adsorption and photodegradation processes. In particular, the cryopolymerization was conducted by using as a starting monomer 2-hydroxyethylmethacrylate (HEMA). HEMA was chosen due to the opportunity to produce cryopolymers in water as well as for its biocompatibility, high light resistance and transparency [40]. Additionally, taking advantage of the hydroxyl pendant groups on HEMA moieties (see **Figure 3.3**), ZnO molecules can be covalently linked to pHEMA by using atomic layer deposition (ALD) method (see **appendix 2**).

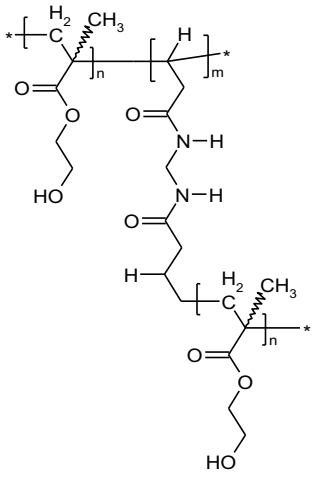

Figure 3.3. Poly-2-hydroxyethylmethacrylate (pHEMA) structure

3.3.1 Graphene oxide as a filler for pHEMA cryogels.

Among the materials designed for both adsorption and photocatalysis, a key role is also reserved for graphene-based polymeric composites. In this context, GO was intensively investigated as an effective low-cost polymeric filler, principally due to its high specific surface area that provides huge adsorption ability versus organic and inorganic contaminants. Its ability to improve thermal and mechanical stability of formulated materials was also considered an interesting feature [41-50]. However, as already reported in chapter one, although GO is an excellent candidate as a constituent of polymeric materials for polymer-supported photocatalyst, a GO content superior than 5% drastically affect the efficiency of the catalytic process. In light of this, having as a goal the development of a material with both, adsorption and photocatalytic properties, polymer composites have to be designed not exceeding this concentration limit. As far as this concept is concerned, pHEMA cryogels was formulated by introducing GO during the non-frozen phase and, subsequently, subjected to ZnO deposition by atomic layer deposition (ALD) method. In the next section the as prepared cryogels (pHEMA, pHEMA-GO, ZnO/pHEMA, ZnO/pHEMA-GO) will be described starting from their physico-chemical characterization to their applicability in MB degradation.

3.3.2 Physico-chemical characterizations.

pHEMA samples were synthesized by using 10% w/w monomers (HEMA and MBAA) solution in water with a molar ratio of 6:1 and 1% w/w APS/TEMED (radical initiators) of the total monomers. Each cryogel was synthesized in 0.5 mL solution in a glass tube, 6 mm in diameter, and frozen overnight at −16 °C. The cryogels were then washed with water, ethanol, and diethyl ether and left to dry at room temperature under nitrogen flux. At this stage, the unmodified pHEMA cryogel represents the plain cryogel used as a reference. To obtain the GO cryocomposite (pHEMA-GO), a sonicated 0.2% water solution of GO was added prior the frozen stage. The as obtained cryosponges (pHEMA and pHEMA-GO) was subjected to the ZnO deposition by ALD (for further details see materials and methods section), to produce the composites ZnO/pHEMA and ZnO/pHEMA-GO. In **Scheme 3.1** is reported a summary of the composites formulation.

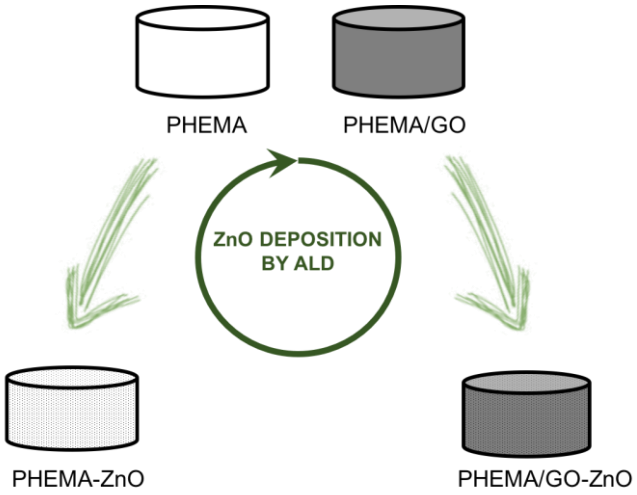

Scheme 3.1. Formulation of ZnO pHEMA-cryogel composites by atomic layer deposition (ALD) process.

The all prepared samples were characterized by thermogravimetric analysis (TGA), Fourier transform infrared (FTIR) spectroscopy, scanning and transmission electron microscopy (SEM and TEM), and X-ray diffraction (XRD), evaluating also their mechanical

performances. In particular, TGA using N_2 as a carrier gas up to 800 °C, was conducted on all samples to evaluate their thermal stability as well as the inorganic content of the polymer composites (see **Table 3.1**). The temperatures at the maximum derivative of weight loss (TMD) range from 404 to 426 °C depending on the material formulation. The low content of GO in the polymer did not significantly change the thermal behavior of the material, whereas the samples enriched with ZnO nanostructures produce a sensible decrease of TMD of about 8−20 °C with a residue ranging from 10 to 15% depending on the ZnO samples. Indeed, as reported in the literature for poly(methylmethacrylate), the content of ZnO higher than 0.15% results in a decrease of the thermal stability due to the contribution of the catalytic effect of ZnO in degrading the polymer matrix [51]. The TGA results also indicate 4.9% of residue in ZnO/pHEMA-GO, which is higher than that in the ZnO/pHEMA sample. This finding is more likely attributed to the presence of ≅0.6% of GO in the polymer specimen. Commercial GO aqueous solution used during the cryopolymerization, is composed of aggregates containing 15−20 sheets with a 4−10% of edge-oxidized suggesting that ZnO nucleates on the defect sites, reacting with the oxidized groups in a covalent mode and contributing to its increment into the final material [52].

SAMPLE	T_{MD} [°C]	Residue at T=800°C [wt.%]
PHEMA	425	2.8
PHEMA-GO	426	3.4
ZnO/PHEMA	418	10
ZnO/PHEMA-GO	404	14.9

Table 3.1. Temperature at the maximum rate of decomposition and residual masses of pHEMA samples as estimated through TGA analyses

In **Figure 3.4**, SEM micrographs of all synthesized samples are reported. The pHEMA sample images [**Figure 3.4 (a−d)**] revealed typical structures consisting of a microporous jagged surface, with a random three-dimensional network. Even though the images collected

for samples containing ZnO [**Figure 3.4 (c,d)**] appeared much more resolved, they did not reveal any significant structural modifications when compared with the samples without ZnO. This is likely due to the great conformability of the ALD process [53]. In the insets of **Figure 3.4**, high-magnification images of the surfaces of pHEMA and pHEMA-GO coated with ZnO were reported. The images displayed the typical morphology of ZnO, formed by small grains, uniformly distributed on the surface, showing a regular shape and size coating [54].

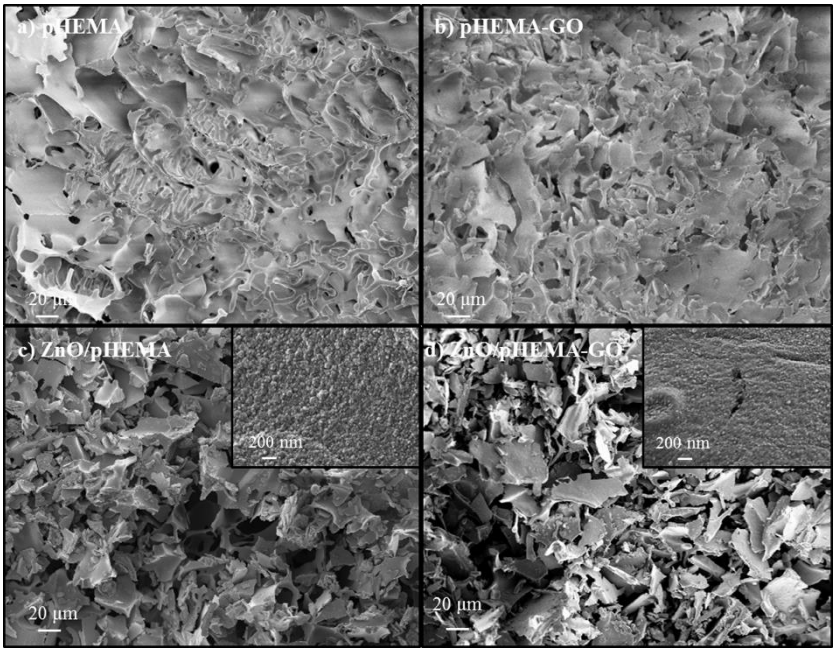

Figure 3.4. SEM images of pHEMA (a), pHEMA-GO (b), ZnO/pHEMA (c), and ZnO/pHEMA-GO (d), together with high-magnification images shown as insets of (c) and (d).

Figure 3.5 reports the TEM analysis of the ZnO/pHEMA sample. In particular, the TEM image in a plan view [**Figure 3.5 (a)**] confirms the morphology of ZnO/pHEMA already showed by the SEM analysis reported in **Figure 3.4**; the ZnO thin film is made of grains with an average diameter of ~10 ± 1 nm (calculated by measuring the diameter of several grains, by Digital Micrograph 3.6.1 of Gatan Inc.). The cross-sectional TEM image reported in **Figure 3.5 (b)** shows the great

conformability of the ZnO film due to the ALD technique and indicates a mean film thickness of ~15 nm.

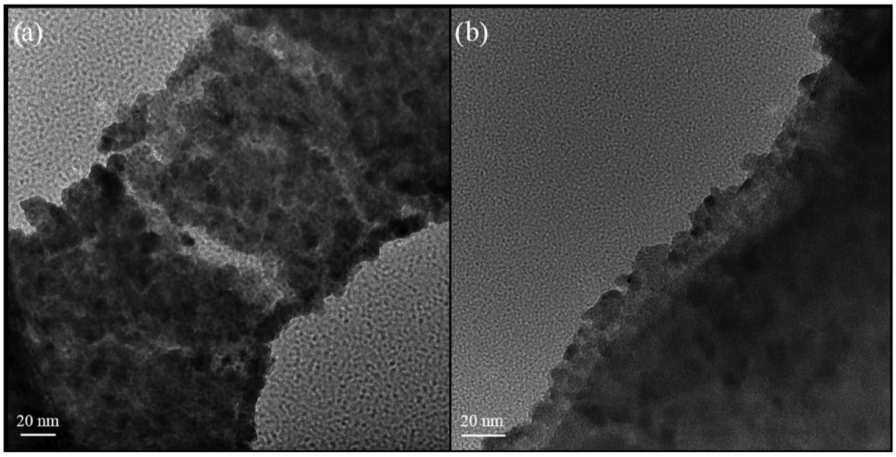

Figure 3.5. TEM images in plan view (a) and cross section (b).

To further appreciate the presence of photoactive ZnO crystals (wurtzite) on the pHEMA materials, XRD analysis was performed before and after the ALD procedure (**Figure 3.6**). The large band observed for pHEMA in **Figure 3.6** is related to the amorphous structure of the polymer. In particular, patterns of both samples showed very broad features consistent with the incoherent scattering from an amorphous solid. Conversely, after ALD cycles of ZnO, the pattern of ZnO/ pHEMA shows well-defined Bragg peaks corresponding to the planes (100), (002), (101), and (110), confirming the wurtzite crystal structure of the thin deposited films (JCPDS 36-1451).

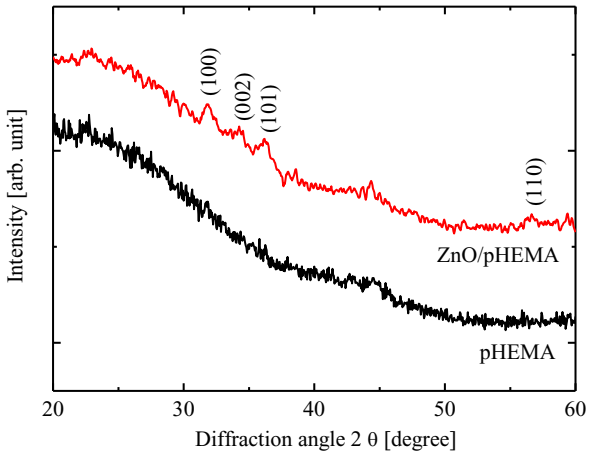

Figure 3.6. XRD patterns of pHEMA, and ZnO/pHEMA (from the bottom to the top).

The average crystallite size is assumed to be the size of a coherently diffracting domain, and it was calculated from the XRD peak width of (101), based on the Debye−Scherrer equation [55] reported below:

$$D = \frac{k\lambda}{\beta_{hkl} cos\theta} \tag{3.8}$$

where β_{hkl} is the integral half-width, k is a constant equal to 0.90, λ is the wavelength of the incident X-ray (λ = 0.1540 nm), D is the crystallite size, and θ is the Bragg angle. The average crystallite size for the ZnO thin film was calculated to be 10 ± 1 nm, which is equal to the value calculated by TEM analysis. Given that, the high absorption capacity, quick absorption equilibrium, and/or swelling−deswelling properties have to be considered fundamental parameters to establish the capture efficiency of the formulated materials toward organic pollutants in water. The dynamic adsorption behavior of the prepared ZnO and GO samples was tested and compared to that of the pHEMA reference

[18,19,56] The equilibrium swelling degree (ESD) can be calculated using the following formula [57]:

$$swelling\ degree = \frac{(m_w - m_d)}{m_d} \quad (3.9)$$

where m_w is the weight of the wet cryogel and m_d is the weight of the dry cryogel. In **Figure 3.7**, the ESD for each sample is reported. The column graph showed similar ESD values for pHEMA, ZnO/pHEMA, and pHEMA-GO, ~9.5 ± 0.2 g g−1, while a lower value was measured for ZnO/pHEMA- GO, ~6.0 ± 0.2 g g^{-1}. This clearly indicated that the ZnO/pHEMA-GO sample is able to adsorb a smaller amount of water. This result is supported by TGA analyses that revealed a higher content of ZnO in ZnO/pHEMA-GO when compared to that in ZnO/pHEMA samples and is consistent with data reported in the literature indicating that ZnO films did not show a relevant water adsorption [51]. As a consequence, a higher ZnO content would induce a lower swelling capacity.

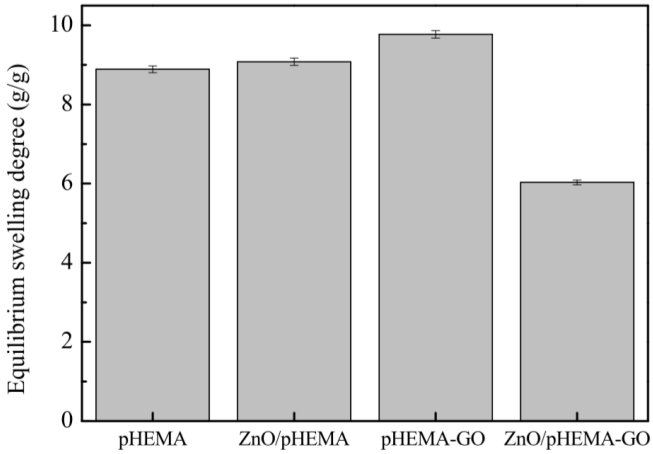

Figure 3.7. Equilibrium swelling degree of pHEMA, ZnO/pHEMA, pHEMA-GO, and ZnO/pHEMA-GO.

Figure 3.8 reported the normalized swelling degrees in water as a function of time. All of the samples took only 2.5 s to reach ~95% of the equilibrium swelling capacity, achieving the equilibrium swollen state in less than 10 s. In this case, the presence of ZnO in the material formulations did not influence the swelling rate of the composites in a relevant manner.

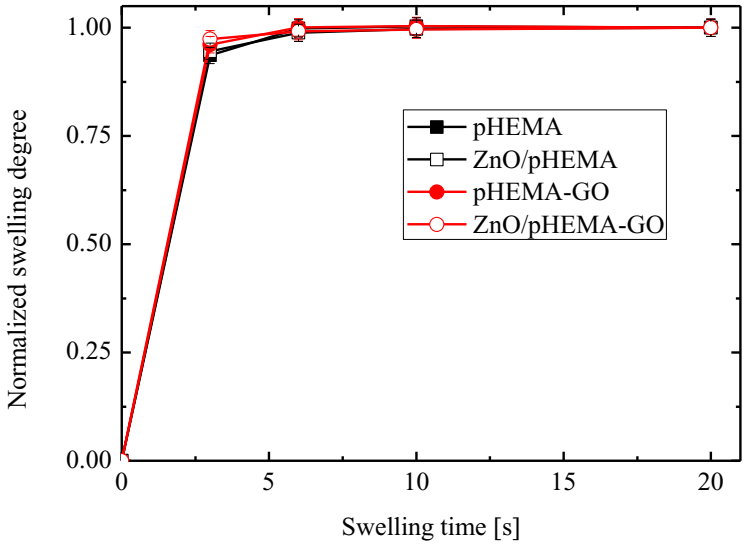

Figure 3.8. Dynamic swelling profiles of pHEMA, ZnO/pHEMA, pHEMA-GO, and ZnO/pHEMA-GO. Constant adsorption capacity values of about 8.9, 9.1, 9.8, and 6.0 g/g were found for pHEMA, ZnO/pHEMA, pHEMA-GO, and ZnO/pHEMA-GO, respectively, after each cycle.

Furthermore, the ZnO nanocomposites exhibited superfast and stable oscillatory swelling and deswelling up to five cycles (**Figure 3.9**) without any significant loss in the swelling degree and water recovery, similar to the results reported by Wang et al. in the literature [59].

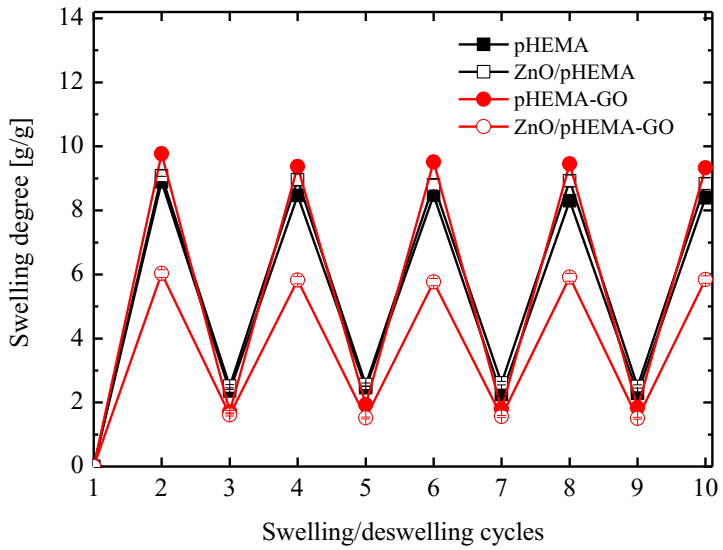

Figure 3.9. Swelling/deswelling degree cycles of all pHEMA samples.

Although the swelling performance of ZnO/pHEMA-GO samples shown in **Figures 3.7** and **3.9** appeared to be slightly affected by the higher amount of ZnO (see **Table 3.1**), we supposed that its contribution certainly could make the difference in terms of pollutant removal. The porosity of the dried samples was calculated as percentage by measuring the absorbed volume of cyclohexane versus the total volume of each sample. The data displayed in **Figure 3.10** evidenced that the porosity of pHEMA was not altered by the addition of GO, as well as of ZnO molecules. In particular, ZnO nanostructuration by ALD could determine the shrinkage of the pore size, affecting the final access to the surrounding medium. The results (**Figure 3.10**) did not show any significant differences in cyclohexane uptake for all samples, suggesting the shrinkage of pore size occurs only after ZnO deposition.

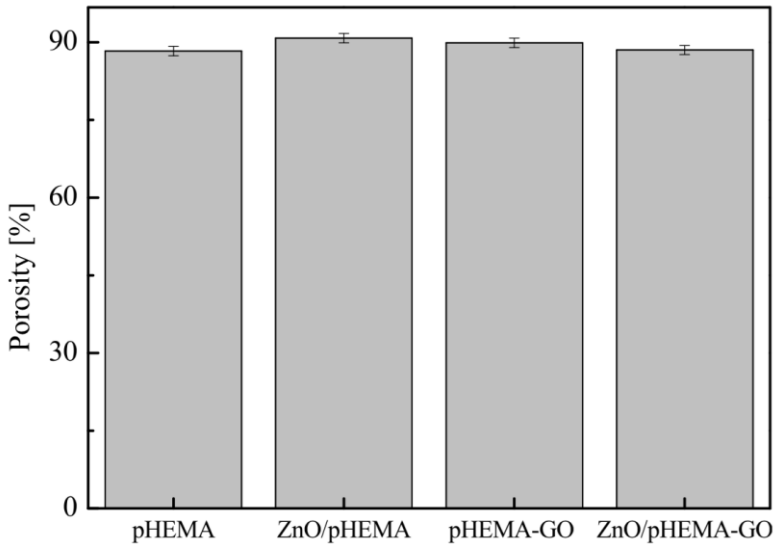

Figure 3.10. Porosity of pHEMA, ZnO/pHEMA, pHEMA-GO, and ZnO/pHEMA-GO cryogels.

To provide information on the mechanical stability of the samples mechanical characterizations were established. **Figure 3.11** shown The curves displaying the stress−strain behavior of the cryogels subjected to compression tests. All of the samples could bear compression strain of 50% without permanent deformation or mechanical destruction. As expected, all of the curves exhibited an elastic deformation region at low strain values followed by a nonlinear stage at compression values above 30% [60]. It is noticed that pHEMA-GO displayed slightly lower values of compressive stress over the entire deformation range investigated, likely due to its higher equilibrium swelling degree.

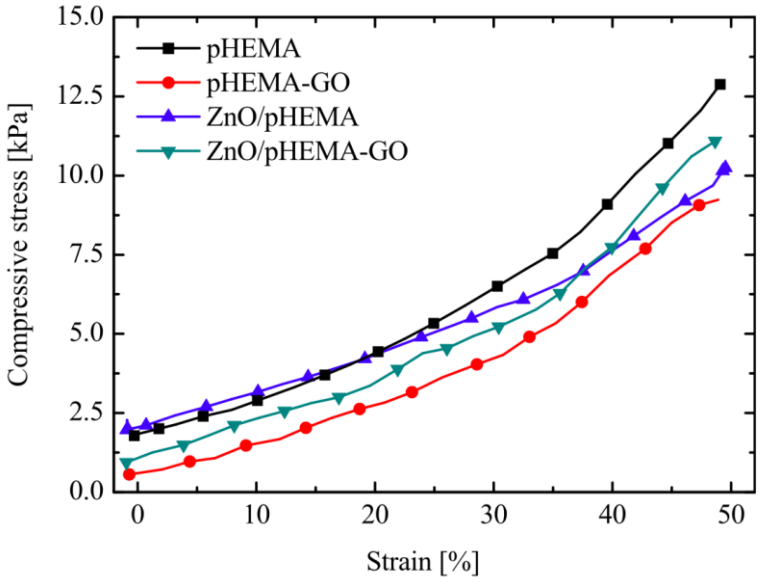

Figure 3.11. Stress−strain curves of pHEMA, ZnO/pHEMA, pHEMA-GO, and ZnO/pHEMA-GO wet cryogels subjected to compression tests.

In addition, this can also arise from a slightly lower cross- linking density due to the interference of GO during the polymerization step. ZnO deposition on pHEMA-GO resulted in increased compression stress, while ZnO/pHEMA did not show significant differences with respect to pHEMA. Young's modulus values calculated from the elastic region (<20% strain) were found to be 12.5 ± 1.8 kPa (pHEMA), 10.9 ± 0.5 kPa (pHEMA-GO), 10.7 ± 2.1 kPa (ZnO/pHEMA), and 11.7 ± 1.0 kPa (ZnO/pHEMA-GO). These values are comparable to those reported for other HEMA-based cryogels and demonstrate the tough and elastic nature of the cryogels, which is appropriate for the envisaged application [61]. To get insight into the recyclability of the cryogels, 10-cycle compression tests were carried out.
All of the samples showed very good mechanical reversibility upon compression cycling, as after 10 cycles at 50% strain, the cryogels maintained 97.3% (pHEMA), 87.2% (pHEMA-GO), 92.8% (ZnO/pHEMA), and 88.0% (ZnO/pHEMA-GO) of the initial compression stress.

3.3.3 Adsorption kinetics and photocatalytic studies

In this section the adsorption capability, contact time, mechanical performances, recyclability, and photocatalytic efficiency of all synthesized cryogels will be discussed. Kinetic adsorption studies were carried out at room temperature to provide information concerning the interaction mechanisms that occur between dye and our functionalized pHEMA materials. To evaluate the amount of MB adsorbed at equilibrium, the cryogels were immersed in a solution of MB overnight, until the equilibrium was reached. At time t, the adsorption capacity, Q_t (mg g $^{-1}$), was determined by the following equation [62]:

$$Q_t = \frac{(C_0 - C_t)}{W} \tag{3.10}$$

where C_0 (mg L^{-1}) is the initial concentration of MB, C_t (mg L^{-1}) is the concentration of MB at time t, V (L) is the volume of the solvent, and W (g) is the amount of adsorbent used in the adsorption process. The results of this experiment are reported in **Figure 3.12**.

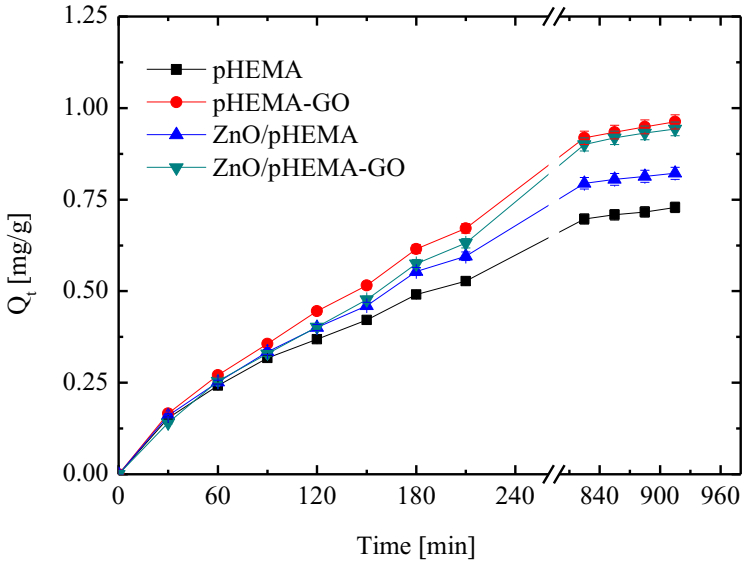

Figure 3.12. MB adsorption capacity versus time for pHEMA, pHEMA-GO, ZnO/pHEMA, and ZnO/pHEMA-GO.

To further achieve information on the distribution of MB molecules between the solid and the liquid phase at the equilibrium, the adsorption kinetics and the capacity of the cryogels at the equilibrium were monitored using the adsorption isotherms. The adsorption capacity at the equilibrium, Q_e (mg g^{-1}), was computed by the following equation:

$$Q_e = \frac{(C_0 - C_t) \times V}{W} \quad (3.11)$$

where C_0 (mg L^{-1}) is the initial concentration of MB, C_e (mg L^{-1}) is the concentration of MB at equilibrium, V (L) is the volume of the solution, and W (g) is the amount of adsorbent used in the adsorption process. In **Table 3.2**, the values of Q_e for each sample are reported. As predictable, the samples containing GO (pHEMA-GO and ZnO/pHEMA-GO) exhibited higher adsorption capacities when compared to those of the unfilled GO samples [34]

SAMPLE	Q_e [mg/g]
pHEMA	0.73 ± 0.01
pHEMA-GO	0.97± 0.02
ZnO/pHEMA	0.82±0.02
ZnO/pHEMA-GO	0.94±0.02

Table 3.2. Equilibrium adsorption capacity of the tested cryogels at room temperature

On the basis of the three kinetics models discussed in the previous section, several fittings of the experimental data were performed. In **Table 3.3**, the values of R^2 for all samples are reported. A comparison of R^2 for the three different models clearly shows that our experimental data fit more closely to the pseudo-second-order law (**Figure 3.13**).

R^2	I Order	II order	Intraparticle diffusion
pHEMA	0.929	0.999	0.923
pHEMA-GO	0.917	0.998	0.912
pHEMA/ZnO	0.918	0.998	0.928
pHEMA-GO/ZnO	0.814	0.997	0.956

Table 3.3. R^2 Values for the different kinetic models of MB adsorption on the tested Samples

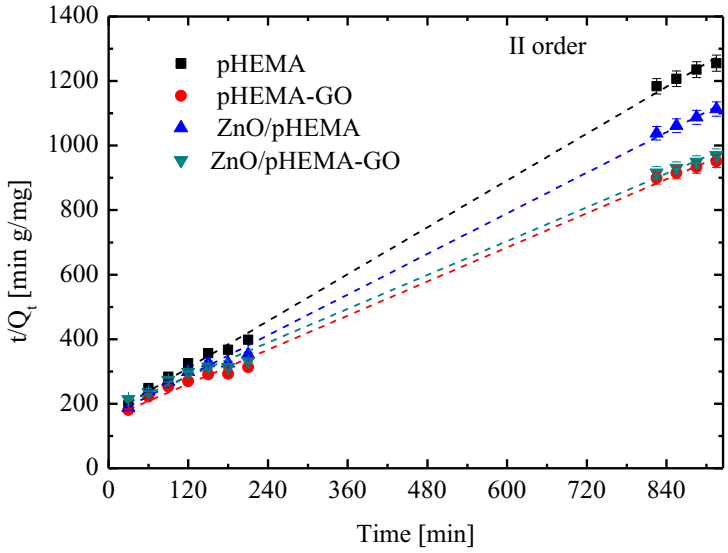

Figure 3.13. Adsorption kinetics of MB for pHEMA (squares), pHEMA-GO (circles), ZnO/pHEMA (up triangles), and ZnO/ pHEMA-GO (down triangles) fitted with the pseudo-second-order model (dashed lines).

As reported in the literature, the pseudo-second-order kinetics model assumes that a chemisorption process occurred [63]. As desirable, MB adsorption performed by our pHEMA cryogels was mainly driven by chemical interactions. To verify the efficacy of the regeneration process accomplished by the ZnO polymer coating, adsorption followed by a photocatalytic process for all of the samples was executed using MB solution as the organic pollutant reference material. Three adsorption processes were performed; after each adsorption process, all samples were irradiated by a UV lamp to regenerate the material via the photocatalytic action of ZnO. The adsorption results obtained in each cycle (420 min for each cycle) are summarized in **Figure 3.14**, reporting a column graph with the percentage of the adsorbed amount of MB for the different samples.

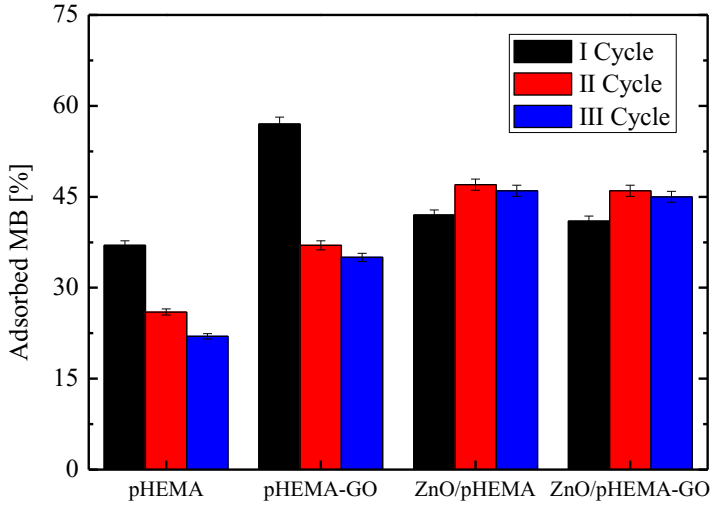

Figure 3.14. Recyclability of pHEMA, pHEMA-GO, ZnO/pHEMA, and ZnO/pHEMA-GO after three adsorption cycles of MB.

The MB dye adsorption was performed in the absence of adsorbent materials and in the presence of pHEMA, pHEMA-GO, ZnO/pHEMA, and ZnO/pHEMA-GO. As expected, no variations in adsorbance percentage values were revealed in the MB reference experiment.

During the first cycle, pHEMA adsorbs ~37% of MB, while pHEMA- GO was able to adsorb ~57% of the dye. The higher value obtained from the latter sample was due to the excellent capability of GO to capture pollutants [36]. ZnO/pHEMA and ZnO/pHEMA-GO samples absorbed ~41% of MB (see **Figure 3.14**). This finding can be reasonable ascribed to the ZnO coverage of the GO sheets that decreased the peculiar GO sequester performance, by hindering the interactions between dye molecules and GO surface. After the second and third cycles, pHEMA and pHEMA-GO exhibited a sensible decrease in the adsorption capacity, indicating that mere UV exposure was not able to photodegrade the adsorbed MB. Consequently, the materials after the third adsorption cycle were not regenerated. As evidenced in the figure, the values decreased from the first to the third cycle in both pHEMA and pHEMA-GO up to ~22 and ~35%, respectively. In contrast, the corresponding samples coated with ZnO showed a nicely comparable adsorption capacity during the three cycles, proving that these devices can be efficiently regenerated by UV light irradiation.

The anchorage of the photocatalyst to the polymeric sponges, which was able to produce ROS in water, clearly played a decisive role in this experiment. To corroborate the effective photoremoval of MB after UV light exposure, FT-IR analyses were performed for the pHEMA and ZnO/pHEMA samples. **Figure 3.15** showed the spectra of as-prepared pHEMA (first from the top), after the first cycle of the adsorption process (the second from the top), and after the photocatalytic process (the third from the top). The pHEMA diagnostic bands at 3400−3100, 2895−2854, 1722, 1162, and 1022 cm^{-1}, corresponding to the O−H, C−H, C=O, and C− C−O group stretching vibrations and O−H bending, respectively, appeared in the IR profile [63]. The FT-IR spectrum of MB in **Figure 3.15**, reported as reference, clearly showed the typical peaks of the dye, in particular, the peak at 1600 cm^{-1} related to the C=C stretching of the aromatic ring and the two peaks at 1354 and 1340 cm^{-1} associated with two different C−N bonds of MB (see vertical dashed lines in **Figure 3.15**) [64]. As expected, after MB adsorption, the IR spectra of both pHEMA and ZnO/pHEMA revealed the appearance of aforementioned MB peaks (drawn lines) among the signals, while from the inspection of the identical samples subjected to UV irradiation up to 5h, their disappearance was evident. Accordingly, in the IR spectra of irradiated virgin pHEMA, peaks belonging to MB

remained visible. FTIR analysis of the ZnO/pHEMA-GO sample was also performed, showing a similar trend.

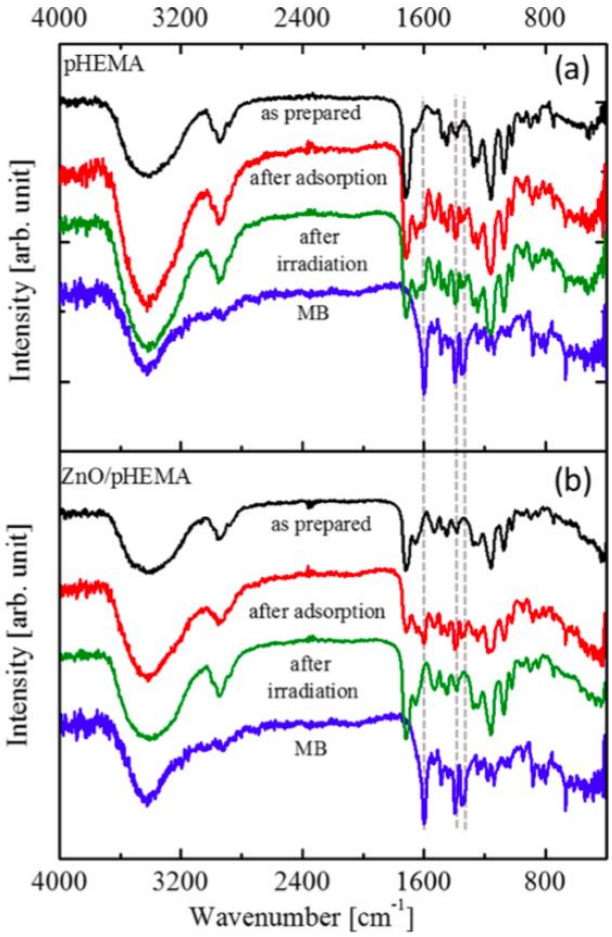

Figure 3.15. FTIR spectra measured on pHEMA (a) and on ZnO/ pHEMA (b): as prepared (first spectrum from the top), after MB adsorption (second spectrum from the top), and after regeneration by UV light irradiation (third spectrum from the top). The spectrum of pure MB is shown as a reference. Vertical dashed lines indicate the typical stretching peaks of MB.

To verify the chemical stability of the samples after regeneration by the photocatalytic process, SEM and XRD analyses of ZnO/pHEMA have been performed and reported in [**Figure 3.16 (a,b)**]. In particular, SEM images [**Figure 3.16 (a)**] show the same morphology of ZnO/pHEMA before the adsorption process. The diffractogram of ZnO/pHEMA after photo- regeneration [**Figure 3.16 (b)**] shows the peaks related to the wurtzite structure at 31.8, 34.5, and 36.5°. The grain size, calculated by Scherrer's law, is 10 ± 1 nm, not showing any variation compared to the size calculated before the photocatalytic regeneration.

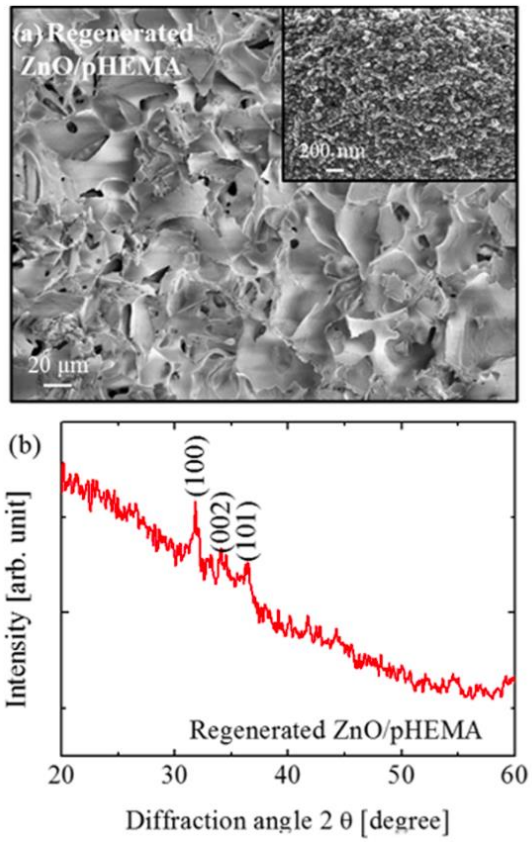

Figure 3.16 (a) SEM analysis of ZnO/pHEMA after regeneration with high-magnification images (inset); (b) XRD diffractogram of regenerated ZnO/pHEMA.

3.3.4 Materials and methods

Materials. 2-hydroxyethylmethacrylate (HEMA), N,N-methylene-bisacrylamide (MBAA), ammonium persulfate (APS), N,N,N′,N′-tetramethylethylenediamine (TEMED), and graphene oxide (GO) in water solution (1 mg mL−1) containing aggregates of 15−20 sheets with a 4−10% of edge-oxidized were purchased from Sigma-Aldrich.

Preparation of pHEMA and pHEMA-GO. The pHEMA cryogel was obtained following the procedure described previously using 10% w/w monomer (HEMA and MBAA) solution in water with a molar ratio of 6:1, HEMA/MBAA, and 1% w/w APS/TEMED of the total monomers [40]. Each cryogel was synthesized in 0.5 mL solution in a glass tube, 6 mm in diameter, and frozen overnight at −16 °C. The cryogels were then washed with water, ethanol, and diethyl ether and left to dry at room temperature under nitrogen flux. At this stage, the unmodified pHEMA cryogel represents the plain cryogel used as a reference. To obtain the GO cryocomposite, a sonicated 0.2% water solution of GO was used as medium to synthetize HEMA and then treated as reported above. The samples used for ALD, TGA, and photocatalytic experiments were cut in pieces of 0.4 cm using the same section eliminating the top and the bottom part of the specimens.

Atomic Layer Deposition of ZnO on pHEMA and pHEMA-GO. ZnO films were deposited by ALD using the Picosun R-200 advanced reactor. During the deposition, the temperature was fixed at 80 °C. ZnO was deposited on cylinders of pHEMA and pHEMA-GO and on pieces of silicon as reference. Diethyl zinc (DEZ, purity 99.9999%) and de-ionized water were used as precursors, while N2 was used as a carrier and purge gas (purity ≥ 99.999%). The pulse and purge times were kept constant at 0.1:3:0.1:5 s for DEZ/N_2/H_2O/N_2, using three-times pulses for both DEZ and H_2O precursors, for a total of 110 cycles. The flow rates for DEZ and H_2O were 150 and 200 sccm, respectively, while the flow in the other lines was 40 sccm. The pressure of the reactor was ~10 hPa. The precursor's temperatures were fixed at 22 °C. The film thickness was evaluated by the Woollam M-2000 spectroscopic

ellipsometer by applying a Cauchy model in the 400−1700 nm range thanks to ZnO deposited on silicon. The film thickness was calculated to be ~15 nm. The pHEMA and pHEMA-GO samples used for this study had a weight of ~5 mg. The synthesized materials after ZnO deposition will be hereafter called “ZnO/pHEMA” and “ZnO/pHEMA-GO”. Characterization. All of the synthesized materials were deeply characterized. The morphology of the sponges was investigated by SEM, with a field emission Zeiss Supra 25 microscope. The pHEMA and ZnO/pHEMA samples were previously coated, by sputtering, with a 10 nm thick gold film to prevent electron beam charging of the insulating polymer. TEM analyses were performed with JEOL ARM200F Cs-corrected operated at low current and low voltage, 60 keV, to avoid specimen damaging and charging. All of the images have been acquired in conventional TEM (C/TEM) mode and bright-field mode. Inelastic scattering contribution of the electrons has been removed by inserting the energy filter, a GATAN Quantum ER, with a 10 eV energy slit tuned on zero loss to improve the contrast and better localize the nanoparticles.

As for the specimen preparation, the processed specimen has been gently scratched on an ultrathin carbon TEM grid and transferred to the microscope.

The structure of the samples was evaluated by XRD analyses, with a Bruker D-500 diffractometer, operating with a parallel Cu Kα radiation at 40 kV and 40 mA, with 2θ from 20 to 60°, in the θ/2θ mode. The XRD spectra were analyzed by the Bruker software suite, including ICSD structure database.

Thermogravimetric analyses of the samples were performed using a thermogravimetric apparatus (TGA, TA Instruments Q500) under a nitrogen atmosphere (flow rate, 60 mL min^{-1}) at 10 °C min^{-1} heating rate, from 40 to 800 °C. Sample weights were approximately 6 mg. TGA sensitivity is 0.1 μg with a weighting precision of ± 0.01%. The isothermal temperature accuracy is ±1 °C.

The swelling properties were determined by gravimetric analyses. For the determination of the swelling profile, dried samples in the form of cylinders, ~5 mm in diameter and 4 mm in height, were swollen in de-ionized water. Excess of surface water was gently wiped off using filter papers before any measurements of the mass of the swollen sample.

To calculate the equilibrium swelling degree, each sample was soaked in water for 30 min and then it was carefully placed on the weight scale. A small amount of water was added to rectify any loss during sample collection and transport, and any excess of water was removed by an absorbent paper. The calculation of water adsorption kinetics was performed by placing each sample in contact with a slight excess of water for the selected time; therefore, the excess of water that was not absorbed was quickly removed by the absorbent paper. The wet sample was weighted, and the value of water absorbed at time t was normalized with respect to the value of the water absorbed after 30 min. For the determination of swelling−deswelling cycle performances, after the first determination of equilibrium swelling, all of the wet samples were placed between two sheets of absorbent paper and squeezed with a 50 g weight for about 5 min. The squeezed samples were weighed, immersed again in water, and then prepared for a new operation of swelling degree determination. This operation sequence was repeated five times.

The porosity of the dried samples was calculated as percentage by measuring the adsorbed volume of cyclohexane versus the total volume of each sample. The porosity of the cryogel samples was measured according to Archimedes' principle using an adapted gravity bottle and determined by the following equation:

$$Porosity\ \% = \frac{V_{pores}}{V_{sample}} 100 = \frac{m_w - m_d}{m_1 - m_2 + m_w} 100 \qquad (3.12)$$

where md is the mass of the dried cryogel, mw is the mass of the cyclohexane-saturated cryogel, m_1 is the mass of the gravity bottle filled with cyclohexane, and m_2 is the mass of the gravity bottle containing cyclohexane and cryogel. To remove the residual gas in the cryogels, the samples were immersed in cyclohexane under reduced pressure before their transfer inside the gravity bottle.

Compression tests of wet pHEMA-based cryogels were performed using a Thermo Scientific RS6000 rotational rheometer in a uniaxial compression mode. Equilibrium swollen cryogel samples were cut in pieces of 6 mm height and placed in between the rheometer plates (20 mm diameter) at 25 °C. The rheometer gap was reduced until the sample was firmly kept between the plates, and then a pre-strain of 0.4 mm was imposed. The samples were then compressed up to 50% of the initial height with a speed of 15 mm min^{-1}.

The adsorption properties of all of the samples were examined through the adsorption of MB dye in aqueous solution. In a typical experiment, ~5 mg of sponges was added in 2 mL of MB solution with a starting concentration of 1.5×10^{-5} M (4.8 mg L^{-1}), at room temperature and with a neutral pH. The adsorption tests were run in parallel for each sample. Every 30 min, the solutions were collected, and the adsorption of MB onto materials was evaluated measuring the variation of the dye absorbance at 664 nm. The dye adsorption on the vial walls was also checked, as a reference, in the absence of the adsorbent materials.

With the aim to regenerate the sponges, they were immersed in de-ionized water and irradiated by a UV lamp, centered at 368 nm, with an irradiance of 4 mW cm^{-2}, for a total time of 5 h.

FTIR characterization was performed by a PerkinElmer Spectrum 1000 spectrometer. The analyzed samples, in the form of tablet, were obtained by mixing ~1 mg of milled sponge with 300 mg of KBr powders in an agate mortar and pressing with a press. To evaluate the adsorption and the eventual photodegradation of the adsorbed dye under UV light irradiation, after the absorption process and after the

UV light irradiation, a portion of each sample was dried, at 100 °C overnight, and analyzed by FTIR spectroscopy, as reported before.

3.4 Work in progress

The use of cryopolymerization represents a promising and versatile tool in the preparation of selective composites for the water purification, principally due to the opportunity to operate with a wide range of monomers and co-monomers. By opportunely modifying the monomer to make it soluble in green solvents, the final device could be addressed versus selective contaminants capture. For instance, cryosponges able to remove arsenic in water with outstanding performances were formulated. As well known, Arsenic (As) is a highly toxic and harmful element for the human health, and in agreement with the World Health Organization, the maximum recommended limit in drinking water is 0.01 ppm. This limit, especially in developing nations, is largely exceeded. Thus, synthesis of 4-vinyl-benzyl-N-methyl-D-glucamine by functionalization of not-soluble 4-vinyl-benzylchloride with water-soluble N-methyl-D-glucamine, provides the formulation of sponges by cryopolymerization in presence of N,N'-methylenebisacrylamide (MBAA, molar ratio 1/6 comparing to the moles of monomer). Additionally, co-polymerization with HEMA were also performed obtaining different rates of arsenic adsorption. The efficacy of the as prepared cryogels for the sequestration of arsenic from water was evaluated using two different concentrations of $Na_2HAsO_4 \bullet 7H_2O$. In particular, high concentrated solutions of arsenate ions equal to 1400 ppm and 140 ppm were used to establish the maximum adsorption ability of the samples. Based on the outstanding results a patent was already applied with number 102019000012339 [65], opened also new perspectives in the formulation of materials for wastewater treatment. Indeed, along with the preparation of materials able to efficacy remove Arsenic, metacrylic acid-based cryogels impregnated by GO solution in a post-polymerization phase, followed by freeze-drying process, could be used to introduce higher amounts

of inorganic filler (not exceeding the 5% limit) obtaining materials able to remove both, organic and inorganic species. Alternatively, the porphyrin monomer well described in the previous chapter and used for RAFT polymerization synthesis, was also applied to the cryopolymerization process, obtaining sponges able to tune the light absorption versus the visible-light range as well as to address improved capture ability versus organic and inorganic contaminants, explicating also a disinfection process.

Conclusions

In this section the preparation of innovative nanocomposites based on a pHEMA polymeric cryogels containing GO and ZnO nanostructures was presented. The formulated materials displayed a noteworthy adsorption aptitude against MB dye. Particularly, sponges enriched with ZnO by ALD have acquired photocatalytic properties, allowing recyclability after their irradiation by UV light. Furthermore, the amounts of adsorbed MB achieved by the different samples, clearly indicates that GO played an important role during the adsorption process. The recyclability and mechanical tests revealed also that ZnO/pHEMA materials can be easily reused, explicating an effective remediation action against organic pollutants. In particular, it was demonstrated how the cryopolymerization technique allows the combination of tailored individual components conferring special features to the final sponges, and resulting an effective strategy for improving the removal and the degradation of contaminants in water.

References.

[1] Liu, F., Chung, S., Oh, G., & Seo, T. S. (2012). Three-dimensional graphene oxide nanostructure for fast and efficient water-soluble dye removal. ACS applied materials & interfaces, 4(2), 922-927;

[2] Gupta, V. K., & Saleh, T. A. (2013). Sorption of pollutants by porous carbon, carbon nanotubes and fullerene-an overview. Environmental science and pollution research, 20(5), 2828-2843;

[3] Ganigar, R., Rytwo, G., Gonen, Y., Radian, A., & Mishael, Y. G. (2010). Polymer–clay nanocomposites for the removal of trichlorophenol and trinitrophenol from water. Applied Clay Science, 49(3), 311-316;

[4] Srinivasan, R. (2011). Advances in application of natural clay and its composites in removal of biological, organic, and inorganic contaminants from drinking water. Advances in Materials Science and Engineering, 2011;

[5] de Luna, M. S., Castaldo, R., Altobelli, R., Gioiella, L., Filippone, G., Gentile, G., & Ambrogi, V. (2017). Chitosan hydrogels embedding hyper-crosslinked polymer particles as reusable broad-spectrum adsorbents for dye removal. Carbohydrate polymers, 177, 347-354;

[6] Vakili, M., Rafatullah, M., Salamatinia, B., Abdullah, A. Z., Ibrahim, M. H., Tan, K. B., ... & Amouzgar, P. (2014). Application of chitosan and its derivatives as adsorbents for dye removal from water and wastewater: A review. Carbohydrate polymers, 113, 115-130;

[7] Chang, C., & Zhang, L. (2011). Cellulose-based hydrogels: Present status and application prospects. Carbohydrate polymers, 84(1), 40-53;

[8] Dutta, K., & De, S. (2017). Smart responsive materials for water purification: an overview. Journal of Materials Chemistry A, 5(42), 22095-22112;

[9] Chong, M. N., Jin, B., Chow, C. W., & Saint, C. (2010). Recent developments in photocatalytic water treatment technology: a review. Water research, 44(10), 2997-3027;

[10] Bonilla-Petriciolet, A., Mendoza-Castillo, D. I., & Reynel-Ávila, H. E. (Eds.). (2017). Adsorption processes for water treatment and purification. Berlin: Springer International Publishing;

[11] Qiu, H., Lv, L., Pan, B. C., Zhang, Q. J., Zhang, W. M., & Zhang, Q. X. (2009). Critical review in adsorption kinetic models. Journal of Zhejiang University-Science A, 10(5), 716-724;
[12] Largitte, L., & Pasquier, R. (2016). A review of the kinetics adsorption models and their application to the adsorption of lead by an activated carbon. Chemical Engineering Research and Design, 109, 495-504;
[13] Ho, Y. S. (2006). Review of second-order models for adsorption systems. Journal of hazardous materials, 136(3), 681-689;
[14] Aydın, Y. A., & Aksoy, N. D. (2009). Adsorption of chromium on chitosan: Optimization, kinetics and thermodynamics. Chemical Engineering Journal, 151(1-3), 188-194;
[15] Ho, Y. S., & McKay, G. (1998). Kinetic models for the sorption of dye from aqueous solution by wood. Process Safety and Environmental Protection, 76(2), 183-191;
[16] Ho, Y. S., & McKay, G. (1998). A comparison of chemisorption kinetic models applied to pollutant removal on various sorbents. Process safety and environmental protection, 76(4), 332-340;
[17] Mattiasson, B., Kumar, A., & Galeaev, I. Y. (Eds.). (2009). Macroporous polymers: production properties and biotechnological/biomedical applications. CRC Press;
[18] Loo, S. L., Krantz, W. B., Fane, A. G., Gao, Y., Lim, T. T., & Hu, X. (2015). Bactericidal mechanisms revealed for rapid water disinfection by superabsorbent cryogels decorated with silver nanoparticles. Environmental science & technology, 49(4), 2310-2318;
[19] Loo, S. L., Fane, A. G., Lim, T. T., Krantz, W. B., Liang, Y. N., Liu, X., & Hu, X. (2013). Superabsorbent cryogels decorated with silver nanoparticles as a novel water technology for point-of-use disinfection. Environmental science & technology, 47(16), 9363-9371;
[20] Marin, M. L., Santos-Juanes, L., Arques, A., Amat, A. M., & Miranda, M. A. (2011). Organic photocatalysts for the oxidation of pollutants and model compounds. Chemical reviews, 112(3), 1710-1750;
[21] Kanakaraju, D., Glass, B. D., & Oelgemöller, M. (2018). Advanced

oxidation process-mediated removal of pharmaceuticals from water: A review. Journal of environmental management, 219, 189-207;
[22] Alvarez, P. J., Chan, C. K., Elimelech, M., Halas, N. J., & Villagrán, D. (2018). Emerging opportunities for nanotechnology to enhance water security. Nature nanotechnology, 13(8), 634;
[23] Pelaez, M., Nolan, N. T., Pillai, S. C., Seery, M. K., Falaras, P., Kontos, A. G., ... & Entezari, M. H. (2012). A review on the visible light active titanium dioxide photocatalysts for environmental applications. Applied Catalysis B: Environmental, 125, 331-349;
[24] Chen, Y., Li, A., Huang, Z. H., Wang, L. N., & Kang, F. (2016). Porphyrin-based nanostructures for photocatalytic applications. Nanomaterials, 6(3), 51;
[25] Chen, X., & Mao, S. S. (2007). Titanium dioxide nanomaterials: synthesis, properties, modifications, and applications. Chemical reviews, 107(7), 2891-2959;
[26] Janotti, A., & Van de Walle, C. G. (2009). Fundamentals of zinc oxide as a semiconductor. Reports on progress in physics, 72(12), 126501;
[27] Reynolds, D. C., Look, D. C., Jogai, B., Litton, C. W., Cantwell, G., & Harsch, W. C. (1999). Valence-band ordering in ZnO. Physical Review B, 60(4), 2340;
[28] Chen, Y., Bagnall, D. M., Koh, H. J., Park, K. T., Hiraga, K., Zhu, Z., & Yao, T. (1998). Plasma assisted molecular beam epitaxy of ZnO on c-plane sapphire: Growth and characterization. Journal of Applied Physics, 84(7), 3912-3918;
[29] Udom, I., Ram, M. K., Stefanakos, E. K., Hepp, A. F., & Goswami, D. Y. (2013). One dimensional-ZnO nanostructures: synthesis, properties and environmental applications. Materials science in semiconductor processing, 16(6), 2070-2083;
[30] Kołodziejczak-Radzimska, A., & Jesionowski, T. (2014). Zinc oxide—from synthesis to application: a review. Materials, 7(4), 2833-2881;
[31] Wang, Z. L. (2004). Nanostructures of zinc oxide. Materials today, 7(6), 26-33;
[32] Schmidt-Mende, L., & MacManus-Driscoll, J. L. (2007). ZnO–nanostructures, defects, and devices. Materials today, 10(5), 40-48;

[33] Man, M. T., Kim, J. H., Jeong, M. S., Do, A. T. T., & Lee, H. S. (2017). Oriented ZnO nanostructures and their application in photocatalysis. Journal of luminescence, 185, 17-22;
[34] Li, Q., Mahendra, S., Lyon, D. Y., Brunet, L., Liga, M. V., Li, D., & Alvarez, P. J. (2008). Antimicrobial nanomaterials for water disinfection and microbial control: potential applications and implications. Water research, 42(18), 4591-4602;
[35] Di Mauro, A., Cantarella, M., Nicotra, G., Privitera, V., & Impellizzeri, G. (2016). Low temperature atomic layer deposition of ZnO: applications in photocatalysis. Applied Catalysis B: Environmental, 196, 68-76;
[36] Srikanth, B., Goutham, R., Narayan, R. B., Ramprasath, A., Gopinath, K. P., & Sankaranarayanan, A. R. (2017). Recent advancements in supporting materials for immobilised photocatalytic applications in waste water treatment. Journal of environmental management, 200, 60-78;
[37] Cantarella, M., Sanz, R., Buccheri, M. A., Ruffino, F., Rappazzo, G., Scalese, S., ... & Privitera, V. (2016). Immobilization of nanomaterials in PMMA composites for photocatalytic removal of dyes, phenols and bacteria from water. Journal of Photochemistry and Photobiology A: Chemistry, 321, 1-11;
[38] Cai, R., Wu, J. G., Sun, L., Liu, Y. J., Fang, T., Zhu, S., ... & Wei, A. (2016). 3D graphene/ZnO composite with enhanced photocatalytic activity. Materials & Design, 90, 839-844;
[39] Singh, S., Mahalingam, H., & Singh, P. K. (2013). Polymer-supported titanium dioxide photocatalysts for environmental remediation: A review. Applied Catalysis A: General, 462, 178-195;
[40] Spina, R. L., Tripisciano, C., Mecca, T., Cunsolo, F., Weber, V., & Mattiasson, B. (2014). Chemically modified poly (2-hydroxyethyl methacrylate) cryogel for the adsorption of heparin. Journal of Biomedical Materials Research Part B: Applied Biomaterials, 102(6), 1207-1216;
[41] Perreault, F., De Faria, A. F., & Elimelech, M. (2015). Environmental applications of graphene-based nanomaterials. Chemical Society Reviews, 44(16), 5861-5896;
[42] Kemp, K. C., Seema, H., Saleh, M., Le, N. H., Mahesh, K.,

Chandra, V., & Kim, K. S. (2013). Environmental applications using graphene composites: water remediation and gas adsorption. Nanoscale, 5(8), 3149-3171;
[43] Filice, S., D'Angelo, D., Libertino, S., Nicotera, I., Kosma, V., Privitera, V., & Scalese, S. (2015). Graphene oxide and titania hybrid Nafion membranes for efficient removal of methyl orange dye from water. Carbon, 82, 489-499;
[44] Yang, S. T., Chen, S., Chang, Y., Cao, A., Liu, Y., & Wang, H. (2011). Removal of methylene blue from aqueous solution by graphene oxide. Journal of colloid and interface science, 359(1), 24-29;
[45] Ramesha, G. K., Kumara, A. V., Muralidhara, H. B., & Sampath, S. (2011). Graphene and graphene oxide as effective adsorbents toward anionic and cationic dyes. Journal of colloid and interface science, 361(1), 270-277;
[46] Kuilla, T., Bhadra, S., Yao, D., Kim, N. H., Bose, S., & Lee, J. H. (2010). Recent advances in graphene based polymer composites. Progress in polymer science, 35(11), 1350-1375;
[47] Potts, J. R., Dreyer, D. R., Bielawski, C. W., & Ruoff, R. S. (2011). Graphene-based polymer nanocomposites. Polymer, 52(1), 5-25;
[48] Periasamy, A. P., Wu, W. P., Ravindranath, R., Roy, P., Lin, G. L., & Chang, H. T. (2017). Polymer/reduced graphene oxide functionalized sponges as superabsorbents for oil removal and recovery. Marine pollution bulletin, 114(2), 888-895;
[49] Huang, Y., Zeng, M., Ren, J., Wang, J., Fan, L., & Xu, Q. (2012). Preparation and swelling properties of graphene oxide/poly (acrylic acid-co-acrylamide) super-absorbent hydrogel nanocomposites. Colloids and Surfaces A: Physicochemical and Engineering Aspects, 401, 97-106;
[50] Sha, J., Gao, Y., Wu, T., Chen, X., Cordie, T., Zhao, H., ... & Turng, L. S. (2016). Biocompatible graphene nanosheets grafted with poly (2-hydroxyethyl methacrylate) brushes via surface-initiated ARGET ATRP. RSC Advances, 6(42), 35641-35647;
[51] Japić, D., Marinšek, M., & Orel, Z. C. (2016). Effect of ZnO on the thermal degradation behavior of poly (methyl methacrylate) nanocomposites. Acta Chimica Slovenica, 63(3), 535-543;

[52] Yu, M., Wang, A., Wang, Y., Li, C., & Shi, G. (2014). An alumina stabilized ZnO–graphene anode for lithium ion batteries via atomic layer deposition. Nanoscale, 6(19), 11419-11424;
[53] Singh, S., Mahalingam, H., & Singh, P. K. (2013). Polymer-supported titanium dioxide photocatalysts for environmental remediation: A review. Applied Catalysis A: General, 462, 178-195;
[54] Di Mauro, A., Fragala, M. E., Privitera, V., & Impellizzeri, G. (2017). ZnO for application in photocatalysis: from thin films to nanostructures. Materials Science in Semiconductor Processing, 69, 44-51;
[55] Saleem, M., Fang, L., Ruan, H. B., Wu, F., Huang, Q. L., Xu, C. L., & Kong, C. Y. (2012). Effect of zinc acetate concentration on the structural and optical properties of ZnO thin films deposited by Sol-Gel method. International Journal of Physical Sciences, 7(23), 2971-2979;
[56] Azizi, S., Ahmad, M., Mahdavi, M., & Abdolmohammadi, S. (2013). Preparation, characterization, and antimicrobial activities of ZnO nanoparticles/cellulose nanocrystal nanocomposites. BioResources, 8(2), 1841-1851;
[57] Loo, S. L., Krantz, W. B., Fane, A. G., Hu, X., & Lim, T. T. (2015). Effect of synthesis routes on the properties and bactericidal activity of cryogels incorporated with silver nanoparticles. RSC Advances, 5(55), 44626-44635;
[58] Liu, C., Liu, X., Quan, C., Li, X., Chen, C., Kang, H., ... & Zhang, C. (2015). Poly (γ-glutamic acid) induced homogeneous mineralization of the poly (ethylene glycol)-co-2-hydroxyethyl methacrylate cryogel for potential application in bone tissue engineering. RSC Advances, 5(26), 20227-20233;
[59] Wang, D. C., Yu, H. Y., Song, M. L., Yang, R. T., & Yao, J. M. (2017). Superfast adsorption–disinfection cryogels decorated with cellulose nanocrystal/zinc oxide nanorod clusters for water-purifying microdevices. ACS Sustainable Chemistry & Engineering, 5(8), 6776-6785;
[60] Zhai, M., Ma, F., Li, J., Wan, B., & Yu, N. (2018). Preparation and properties of cryogel based on poly (hydroxypropyl methacrylate). Journal of Biomaterials Science, Polymer Edition, 29(12), 1401-

1425;
[61] Kumari, J., & Kumar, A. (2017). Development of polymer based cryogel matrix for transportation and storage of mammalian cells. Scientific reports, 7, 41551;
[62] Bonilla-Petriciolet, A., Mendoza-Castillo, D. I., & Reynel-Ávila, H. E. (Eds.). (2017). Adsorption processes for water treatment and purification. Berlin: Springer International Publishing;
[63] Sahiner, N., & Demirci, S. (2017). The use of graphene oxide-embedded superporous poly (2-hydroxyethylmethacrylate) cryogels for p (aniline) conductive polymer synthesis and their use in sensor applications. Materials & Design, 120, 47-55;
[64] Kumpan, N., Poonsawat, T., Chaicharoenwimolkul, L., Pornsuwan, S., & Somsook, E. (2017). Ferrocenated nanocatalysts derived from the decomposition of ferrocenium in basic solution and their aerobic activities for the rapid decolorization of methylene blue and the facile oxidation of phenylboronic acid. RSC Advances, 7(10), 5759-5763;
[65] Patent Application for Industrial Invention: “N-alkyl-D-glucamine based macroporous polymeric cryogel for sequestering and/or removing toxic contaminants” Application number: 102019000012339

Appendix 1:

Chemical Vapor Deposition (CVD) of graphene

The discovery of graphene led to the development of more and more innovative approaches in its preparation, spanning from simple mechanical cleavage, to epitaxial growth on SiC or metals, to chemical vapor deposition (CVD) on metal substrates.
CVD of graphene is a process in which a gas precursor (low molecular weight idrocarbon) is injected to a reduced pressure chamber, reacting with a metal catalyst at high temperature (~ 1000°C) and forms a graphene film onto the catalyst surface. Compared to other graphene synthetic methods, CVD is considered a more versatile process, allowing a fine-tuning of the deposited graphene and its morphology, with the possibility of large-scale production with very high levels of reproducibility and purity of the grown graphene. However, the quality of the deposited graphene also depends on the specific metal substrate used for the graphene synthesis, involving different deposition mechanisms.
In this thesis, polycrystalline Ni foam was selected as catalytic substrate and methane was used as gas precursor. In this case, methane is decomposed at 1000°C at the Ni surface and carbon is dissolved in the substrate. After cooling, a segregation process of carbon atoms, followed by the graphene growth on Ni surface was achieved. A schematic diagram of the graphene growth mechanism on Ni substrate is reported in **Figure A1**.

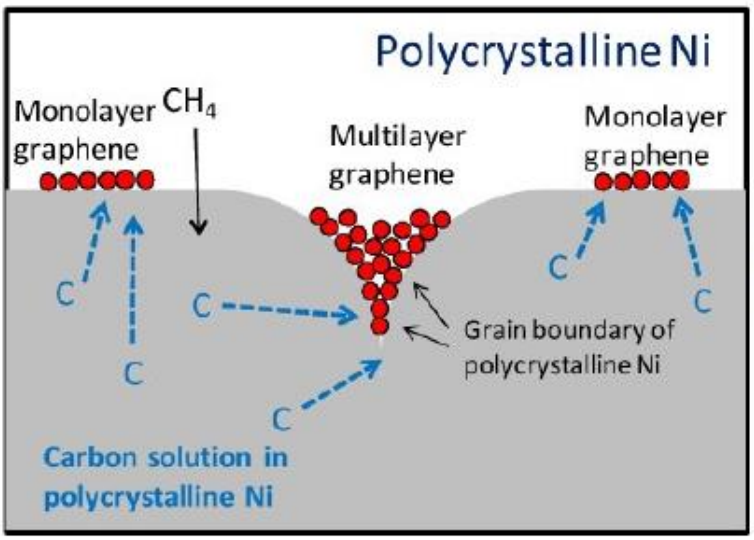

Figure A1. Diagram of the growth mechanism on polycrystalline Nickel. Reproduced from Ref. [1] with kind permission of ACS

Even though, differently from Ni (111) or other metals such as copper, the use of polycrystalline Nickel produces monolayer and multilayer regions, the unique interconnected structure of 3D graphene, its tunable porosity, ease of surface functionalization, outstanding electron-transfer efficiency as well as improved electrical and optical properties, opened new exciting perspectives in a wide range of applications for graphene macrostructures.

References

[1] Zhang, Y. I., Zhang, L., & Zhou, C. (2013). Review of chemical vapor deposition of graphene and related applications. Accounts of chemical research, 46(10), 2329-2339.

Appendix 2

Atomic Layer Deposition (ALD) on polymer

The research field on polymers is constantly expanding, especially with the aim to produce innovative environmental-friendly advanced materials. For example, polymer surface modification with nanomaterials confers it new exciting properties such as bio-functionalities, barrier properties, photocatalytic or biodegradable activity and hydrophobic to hydrophilic conversion, and so on. To this purpose, among several chemical and physical methods commonly used, atomic layer deposition (ALD) can offer many advantages compared to other techniques, such as the opportunity to work at very low temperature, even room temperature, promoting also covalent bonding between nanostructured metal oxides and the polymer substrates. Furthermore, ALD allows conformal and homogeneous coating on a large polymer surface area, thanks to a fine control of the thickness of thin films at the angstrom level based on sequential and self-saturating surface reactions [1-3].

On the other hand, from the technical point of view, the ALD uses two or more chemicals, typically low-cost gas precursors, that are feed in a reaction chamber at low pressure, separately. Each precursor saturates the surface forming a monolayer of material. However, to achieve a stable adhesion at the polymer/inorganic interface, and thus a controlled self-limiting reaction, both polymers and metal precursors have to be properly selected. Indeed, polymers possessing different functional groups involve specific deposition reaction mechanisms that can drastically influence their chemical, physical and mechanical properties.

In this thesis poly-hydroxyethylmethacrylate (pHEMA) and pHEMA-graphene oxide cryogels were functionalized with ZnO nanostructures by ALD. The procedures to formulate the nanocomposites are summarized in Figure A2. ZnO layers were linked to the OH pendant groups of pHEMA and GO by using $Zn(C_2H_5)_2$ and H_2O as precursors.

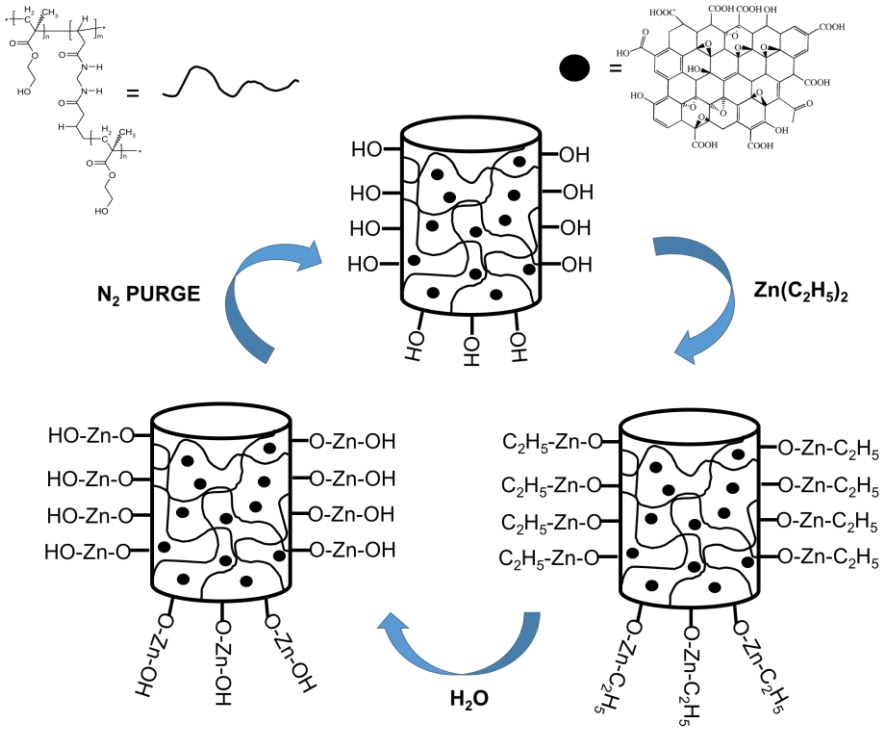

Figure A2. Schematic diagram of the ZnO deposition on polymeric cryogels by ALD.

References

[1] Ahn, J., Ahn, C., Jeon, S., & Park, J. (2019). Atomic layer deposition of inorganic thin films on 3D polymer nanonetworks. Applied Sciences, 9(10), 1990;
[2] Yu, M., Wang, A., Wang, Y., Li, C., & Shi, G. (2014). An alumina stabilized ZnO–graphene anode for lithium ion batteries via atomic layer deposition. Nanoscale, 6(19), 11419-11424.

Curriculum Vitae

Martina Ussia was born in Frosinone (Italy) in 1987. She moved to Catania (Italy) where she started her academic career. In 2012 she attained her Master degree in Organic and Bioorganic chemistry at the University of Catania. Few months later she won a scholarship at the University of Catania working on the design and molecular diagnostic in oncology under the supervision of Prof. Daniele F. Condorelli. At the end of 2014 she obtained a scholarship at the Institute of Biomolecular Chemistry (CNR-ICB Catania Unit), by working on the "Spin-Off" PO FSE project (sochimsal.icb.cnr) up to 2015. In October 2016, she attained a second master degree in Chemical Engineering for industrial sustainability working on the development of polymer nanocomposites based on carbon nanotubes. In November 2016 she started the PhD course in Materials Science and Nanotechnology at the University of Catania. In particular, she obtained a fellowship by CNR-IMM (Catania Unit) to work on polymeric nanocomposites for water remediation. She spent part of her PhD course at the University of Florida (Gainesville, USA) as an Exchange Visitors Student in the framework of the project H2020-MSCA-RISE-VAHVISTUS, under the supervision of prof. Brent Sumerlin, working on novel RAFT copolymers based on porphyrins molecules. Her main research is focused on the development of new stimuli-responsive nanocomposites based on graphene in addition to photoactive organic and/or inorganic semiconductors for water and biomedical applications.

List of Publications

[1] **Ussia M.,** Bruno E., Spina E., Vitalini D., Pellegrino G., Ruffino F., Privitera V., Carroccio, S.C. (2018). Freestanding photocatalytic materials based on 3D graphene and polyporphyrins. Scientific reports, 8(1), 5001;

[2] **Ussia M.**, Di Mauro A., Mecca T., Cunsolo F., Nicotra G. Spinella, C., Cerruti P., Impellizzeri G., Privitera V., Carroccio, S. C. (2018). ZnO–pHEMA Nanocomposites: An Ecofriendly and Reusable Material for Water Remediation. ACS applied materials & interfaces, 10(46), 40100-40110;

[3] **Ussia M.**, Ruffino F., Bruno E., Spina E., Conticello I., Privitera V., Carroccio, S.C. (2019). The role of solvent on the formulation of graphene/polyporphyrin hybrid material versus photocatalytic activity. Polymer Bulletin, 1-15;

[4] **Ussia M.**, Urso M., Miritello M., Bruno E., Curcuruto G., Vitalini D., Condorelli G.G., Cantarella M., Privitera V., Carroccio S.C., (2019) Hybrid Nickel-free graphene/porphyrin rings for photodegradation of emerging pollutants in water, RSC Advances, 9, 30182.

Other publications

[1] Gorrasi G., Bugatti V., **Ussia M.**, Mendichi R., Zampino D., Puglisi C., Carroccio, S.C. (2018). Halloysite nanotubes and thymol as photo-protectors of biobased polyamide 11. Polymer degradation and stability, 152, 43-51;

[2] Clarizia G., Bernardo P., Carroccio S. C., **Ussia M.**, Restuccia C., Parafati L., Zampino D., Heterogenized Imidazolium-based ionic liquids in Pebax®RNEW. Thermal, Gas transport and antimicrobial properties, (Under Submission)

Patents

Ussia M., Mecca T., Cunsolo F., Scurti S., Caretti D., Privitera V., Carroccio S.C., “N-alkyl-D-glucamine based macroporous polymeric cryogel for sequestering and/or removing toxic contaminants” Application number: 102019000012339

Communications

- **Invited Speaker**

[1] 7-9 May 2019, Materials, AIV XXIV Conference, Interfaces, Processes in Industrial and Basic Research Applications, Giardini Naxos (Italy), M.Ussia **"Hybrid Nickel-free graphene polyporphririn photocatalyst: Time-saving formulation and photodegradation studies"**;

[2] 15-16 April 2019, Vahvistus-Bio2019 - VALORIZATION OF NATURAL AND SYNTHETIC BIOMOLECULES IN NOVEL DRUG-VECTOR NANOSTRUCTURES, Fez (Morocco), M.Ussia "**ROS-responsive materials based on porphyririn polymers**";

- **Oral Communication**

[1] 30 September-4 October 2019, Catania (Italy), FISMAT 2019 **M.Ussia** et al. ***"Formulation of Nickel-free 3D graphene for Visible-Light photocatalysis";***

[2] 27-31 May 2019, Nizza (France), EMRS-SPRING 2019 **M.Ussia** et al. **"Time-saving preparation of Nickel-free 3D graphene for Visible-Light photocatalysis"**;

[3] 23-24 May 2019, Blois (France), 9 JOURNEE NATIONALES SUR LA RECUPERATION ET LE STACKAGE D'ENERGIE, **M.Ussia** et al. ***"Hybrid Ni-free 3D graphene/polyporphyrin with improved electron-transfer for light-harvesting";***

[4] 10-15 March 2019 HYMA2019 Sitges (Spain) MULTIFUNCTIONAL, HYBRID AND NANOMATERIALS **M.Ussia** ***"Hybrid nanomaterials based on 3D graphene and polyporphyrins for visible-light photocatalysis";***

[5] 22-26 October 2018 MATERIALS.IT, Bologna, (Italia) **M.Ussia et al.** *"**Novel 3D graphene and cyclic-polyporphyrins hybrid materials for photocatalytic applications**;*

[6] 9-12 September 2018, Catania (Italia), XXIII CONVEGNO NAZIONALE Associazione Italiana di Macromolecole (AIM) CATANIA, **M.Ussia** et al.*"**Materials based on 3D graphene and polyporphyrins for Visible-Light photocatalysis**";*

[7] 14-15 June 2018, Salerno (Italia) MACROGIOVANI 2018- Associazione Italiana di Macromolecole (AIM), **M.Ussia** *"**Multifunctional materials based on GO-pHEMA ZnO for pollutants adsorption and photodegradation**";*

[8] 13-15 June 2017 Trento (Italia) MACROGIOVANI 2017- Associazione Italiana di Macromolecole (AIM), **M.Ussia** *"**Novel polymeric materials based on graphene for water purification**";*

- **Poster Communication**

[1] 28-30 August 2019, Salerno, CHEMISTRY MEETS INDUSTRY AND SOCIETY 2019- Associazione Italiana di Macromolecole (AIM), **M.Ussia** et al. ***"Formulation of Nickel-free 3D graphene for Visible-Light photocatalysis"***

[2] 9-12 September 2018, XXIII CONVEGNO NAZIONALE Associazione Italiana di Macromolecole (AIM), Catania (Italia), **M.Ussia** et al., **"*Materials based on 3D graphene and polyporphyrins for Visible-Light applications"*;**

[3] 9-12 Settembre 2018 XXIII CONVEGNO NAZIONALE Associazione Italiana di Macromolecole (AIM), Catania (Italia), T.Mecca, F.Cunsolo, M.Ussia, A.Di Mauro, G.Impellizeri,

V.Privitera, S.Carroccio, ***"Criogeli nanostrutturati a base di PHEMA-ZnO: nuovi materiali riciclabili per il trattamento e purificazione delle acque";***

[4] 9-12 Settembre 2018 XXIII CONVEGNO NAZIONALE Associazione Italiana di Macromolecole (AIM), Catania (Italia), G.Munzi, M.Ussia, G.Gorrasi, A.Cannizzaro, M.Agati, S.C.Carroccio, S.Boninelli, ***"Polymer nanocomposites based on Ultrathin Silicon Nanowires";***

[5] 9-12 Settembre 2018 XXIII CONVEGNO NAZIONALE Associazione Italiana di Macromolecole (AIM), Catania (Italia), **M.Ussia** et al. **"Halloysite nanotubes filled thymol as photo-protectors of biobased polyammide 11"**;

[6] 9-12 Settembre 2018 XXIII CONVEGNO NAZIONALE Associazione Italiana di Macromolecole (AIM), Catania (Italia), D.Caretti, S.Scurti, F.Cunsolo, T.Mecca, M.Ussia, S.C.Carroccio, ***"Nuovi materiali polimerici per la complessazione di arsenico dalle acque";***

[7] 14-15 Settembre 2017 Italian Nordic Polymer Future - Associazione Italiana di Macromolecole (AIM), Pisa (Italia) **M.Ussia** et al. ***"Freestanding photocatalytic device based on polyporphyrin and graphene foam nanocomposite"***

[8] 22-26 Maggio 2017 European Material Research Society (E-MRS) - Spring meeting, Strasburgo (Francia) **M.Ussia** et al.: ***"Novel polymeric materials based on r-GO/Porphyrin systems for photocatalytic applications";***

Schools participation

[1] 10 - 14 June 2019 Bologna, (Italy), **"VIII Ciamician Photochemistry School, From Fundamentals to Applications";**

[2] 14-19 May 2017 Brescia, (Italy) - European Polymer Federation Summer School in **"Transport Phenomena in polymers and hybrid Materials";**

[3] 12-15 December 2016, Bologna (Italy) - CNR-IMM – **"Scanning Electron Microscopy school in material science"**

Awards

[1] **GRADUATE STUDENT AWARD**, 2019 E-MRS SPRING MEETING (Symposium H) Materials for applications in photocatalysis and photoconversione 27-31 May 2019, Nizza (France);

[2] **OUTSTANDING ORAL PRESENTATION AWARD**, JNRSE 2019 23-24 May 2019, Blois (France);

[3] **BEST ORAL PRESENTATION AWARD** MACROGIOVANI 2018 Associazione Italiana di Macromolecole (AIM), 14-15 June 2018, Trento, Italy;

[4] **BEST ORAL PRESENTATION AWARD** MACROGIOVANI 2017 Associazione Italiana di Macromolecole (AIM), 13-15 June 2017, Salerno (Italy).

Collaboration with other Institutions

- CNR-IPCB (Italy);
- CNR-ICB Catania Unit (Italy);
- University of Bologna, Chemistry Department (Italy);
- University of Florida, Chemistry Department (Gainesville, USA)

Acknowledgments

The most important thanks are addressed to my family for its unconditional love, unevaluable work, their protection and comprehension, even in the darkest moments. I was very lucky to be guided from so fantastic people.
I would like to thank Mario to be my love, to make every day better and better, to understand my feelings. You take my dreams and my secrets and a lot more.
Heartfelt thanks go to my tutor Dr. Sabrina Carola Carroccio, who helped me to realize my objectives every day, to make me a best researcher and woman, to have believed in me!
My gratitude goes to Dr. Vittorio Privitera to have given me the opportunity to be part of his research group, for his scientific support during the last three years.
Thanks also to Prof. Elena Bruno, my university tutor, for her collaboration and support from the beginning, important to my personal and professional growth.
My sincere gratitude goes to Dr. Daniele Vitalini, Dr. Giusy Curcuruto Dr. Daniela Zampino, Dr. Emanuela Spina, Prof. Daniele Caretti, Dr. Tommaso Mecca, Dr. Franca Cunsolo, Dr. Giuliana Impellizzeri, Dr. Maria Miritello, Prof. Francesco Ruffino, Prof. Guido Condorelli, Dr. Alessandro Di Mauro, Dr. Simona Boninelli who accompanied me for most of this PhD period, for sharing their scientific knowledge and supporting me with useful suggestions and sincere friendship.
A special thank goes to my collegues and dear friends Dr. Pierfrancesco Cerruti, Dr. Anna Calarco, Prof.ssa Veronica Ambrogi and Dr. Maurizio Avella, to allow me to take part of their great family in Naple, for their scientific support, for the fantastic experiences in Florida and Morocco, very important for improving my knowledge and my work.
Thanks also to all my colleagues and friends: Giacomo Torrisi, Maria Censabella, Rosario Raciti, Marzia Monforte, Vincenzina Strano, Maria Cantarella, Paola Lova, Martina S. De Luna and Valentina Marturano.

I am deeply grateful to all components of Italian Macromolecular Association committee to give me the opportunity to actively participate in the association projects.
I want also to acknowledge Prof. Maria Grazia Grimaldi and Prof. Salvo Mirabella, coordinator and vice-coordinator of the PhD, for their patience, availability and support all the way.
I would like to express my gratitude to Prof. Brent Sumerlin, to accept me in his research group and for providing me original insights within our collaborations.
A very special thank goes to Gaetano e prof. Cuttone, who they always supported me with their advices and to be close me like a second family!

GRAZIE A TUTTI DI CUORE!